

MASARYK UNIVERSITY
FACULTY OF SCIENCE
DEPARTMENT OF THEORETICAL PHYSICS AND
ASTROPHYSICS

PH.D. DISSERTATION

TRANSITING EXTRASOLAR PLANETS
AND STAR-PLANET INTERACTION

TEREZA KREJČOVÁ

SUPERVISOR: RNDR. JÁN BUDAJ, CSc.



BRNO 2013

BIBLIOGRAPHIC ENTRY

- Author:** Tereza Krejčová
Faculty of Science, Masaryk University
Department of Theoretical Physics and Astrophysics
- Title of Dissertation:** Transiting extrasolar planets
and star–planet interaction
- Degree Programme:** Physics
- Field of Study:** Theoretical Physics and Astrophysics
- Supervisor:** RNDr. Ján Budaj, CSc.
Astronomical Institute of Slovak Academy of Sciences
Tatranská Lomnica, Slovakia
- Academic Year:** 2012/2013
- Number of Pages:** 118
- Keywords:** Extrasolar planet; light curve; transit; CCD photometry;
out-of-eclipse variation; reflection effect; star–planet interaction;
Ca II H and K line; $\log R'_{\text{HK}}$ parameter; statistical test

BIBLIOGRAFICKÝ ZÁZNAM

- Autorka:** Tereza Krejčová
Přírodovědecká fakulta, Masarykova Univerzita
Ústav Teoretické Fyziky a Astrofyziky
- Název práce:** Tranzitující extrasolární planety
a interakce mezi hvězdou a planetou
- Studijní program:** Fyzika
- Studijní obor:** Teoretická Fyzika a Astrofyzika
- Školitel:** RNDr. Ján Budaj, CSc.
Astronomický Ústav Slovenskej Akadémie Vied
Tatranská Lomnica, Slovensko
- Akademický rok:** 2012/2013
- Počet stran:** 118
- Klíčová slova:** Extrasolární planeta; světelná křivka; tranzit; CCD fotometrie;
mimožákrytové variace; reflexní jev; interakce hvězda-planeta;
čára Ca II H a K; parametr $\log R'_{HK}$; statistický test

ABSTRACT

The focus of this thesis is extrasolar planets. The first chapter is devoted to the analysis of transiting exoplanet light curves and the process followed to determine the physical and orbital parameters of the system from its measured light curve. In the first sections of Chapter 1, we describe observations and consequent data analysis of exoplanetary systems Wasp-10 and TrES-3. Two different telescopes were used, the 50 cm telescope, located at Stará Lesná, Slovakia and the 2.2 m telescope, located at the Calar Alto Observatory in Spain. The last section of the first chapter is focused on the modelling of the out-of-eclipse light curve of exoplanetary system KOI-13.01. The changes in this part of the light curve are extremely small and are caused by a combination of several effects, such as the reflection of the light from the exoplanet and its dependence on the phase angle, ellipsoidal variations of the star, the thermal emission from the planet, and the doppler boosting effect. Such variations in the light curve require a very precise photometry and are observable from the space only. Data from the Kepler Mission were used for the verification of the model of the out-of-eclipse light curve. As a result, the constraints on the Bond albedo of the exoplanet and on the heat redistribution over the planetary surface were set.

In the second chapter the interaction between the star and exoplanet is studied. Exoplanets orbiting close enough to their parent stars – in tenths of an astronomical unit – can interact with the upper layers of their stars’ atmospheres via tidal or magnetic interaction. We search for the imprints that these effects can leave in the cores of Ca II H and K absorption lines, which are formed in the chromosphere of the star. We studied the correlations between the chromospheric activity represented by two different indicators – the equivalent width of the core of Ca II K line and the $\log R'_{\text{HK}}$ parameter – and selected parameters of the star-exoplanet systems, mainly semi-major axis, planetary mass, and stellar temperature. The sample consists of more than 200 stars with exoplanets. For this purpose the spectra from the Keck HIRES archive and data obtained with the 2.2 m telescope of the European Southern Observatory at La Silla in Chile were used. We found a statistically significant evidence, that cool stars ($T_{\text{eff}} < 5500 \text{ K}$) with close-in exoplanets ($a < 0.15 \text{ AU}$) are more chromospherically active than stars with exoplanets at more distant orbits.

ABSTRAKT

Tato dizertační práce se zabývá studiem extrasolárních planet. První část se věnuje analýze světelných křivek tranzitujících exoplanet. Je zde popsán postup pro získání fyzikálních a orbitálních parametrů exoplanety z naměřených dat, v tomto případě z pozorovaných tranzitů dvou exoplanetárních systémů Wasp-10 a TrES-3. Zpracována jsou zde fotometrická data ze dvou rozdílných přístrojů – 50 cm dalekohledu ve Staré Lesné na Slovensku a z 2.2 m dalekohledu na observatoři Calar Alto ve Španělsku. Poslední sekce první kapitoly se zabývá modelováním části světelné křivky mezi primárním a sekundárním zákrytem exoplanetárního systému KOI-13.01. Změny této části křivky které jsou extrémně malé, jsou způsobeny kombinací více faktorů, jako jsou světelné změny způsobené odrazem světla z hvězdy od planety, elipsoidálními variacemi hvězdy, tepelným zářením planety a tzv. “boosting” jevem. Ke studiu takovýchto variací světelné křivky jsou zapotřebí přesná fotometrická data dosažitelná pouze z vesmíru. Pro ověření modelu světelných změn mimo primární a sekundární tranzit jsou proto použita data z družice Kepler. Výsledkem je určení rozmezí hodnot Bondova albeda planety a účinnosti přenosu tepla po povrchu planety.

Druhá kapitola této práce je věnována interakci mezi hvězdou a planetou. Předpokládá se, že exoplanety obíhající hvězdu ve velmi malé vzdálenosti – řádově desetiny astronomické jednotky – mohou díky slapové nebo magnetické interakci ovlivňovat vrchní vrstvy atmosféry hvězdy. Zaměřili jsme se na výzkum jádra čar Ca II H a K, které se formují ve chromosféře a mohou být těmito efekty ovlivněny. Hledali jsme vzájemnou souvislost mezi chromosférickou aktivitou hvězdy popsanou dvěma různými indikátory – ekvivalentní šířkou jádra absorpčních čar Ca II K a parametrem $\log R'_{HK}$ – a vybranými parametry exoplanetárního systému, především velkou poloosou, hmotností planety a teplotou hvězdy. Vzorek obsahuje více než 200 exoplanetárních systémů. Pro tento účel byla použita spektra z archivu dalekohledu Keck a vlastní naměřená data pořízená na 2.2 m dalekohledu Evropské jižní observatoře na La Silla v Chile. Výsledkem bylo nalezení statisticky významné indikace, že chladné hvězdy ($T_{\text{eff}} < 5500 \text{ K}$) s blízkými exoplanetami ($a < 0.15 \text{ AU}$) jsou více chromosféricky aktivní než hvězdy kolem kterých obíhají exoplanety ve velkých vzdálenostech.

ACKNOWLEDGEMENT

Many times in the past I promised myself not to leave the important things to the last minute. Well, here I am. It is almost midnight, few hours before the deadline and I am writing this last but for me one of the most important parts of the thesis. There are many people in my mind connected with the last five years of my PhD studies and I want to thank all of them. The most important one is without any doubt my thesis advisor Ján Budaj. His never-dying research enthusiasm he was willing to share with me every day was unbelievable and very inspiring. He always had time to listen and to help me. I would like to thank him deeply for all the guidance, encouragement, help, discussions, and time he provided me. I really appreciate all the years of being his PhD student.

My thanks also go to our collaborators Martin Vaňko and Lubo Hambálek. I want to thank Martin for his never-ending good mood and help during the work on the TrES-3 system. Thanks to Lubo for all the help and discussions concerning the Kepler data and for our mountain trips.

I also want to thank the staff of the astronomical institute in High Tatra mountains in Slovakia, especially to the grad students Zuzka, Lubo, Dušan, Marcela, Maťo, Zuzka and Marek. I have spent there almost one year of my PhD studies and it was a great time full of science and a scent of conifers.

I want to thank Marek Chrastina, my officemate, for all the discussions concerning the CCD photometry and for all our violin playing.

The grad school wouldn't be what it was without grad students. I want to thank Terka, Honza, Milka, Klara, and Jirka for creating a great atmosphere at our astrophysics department in Brno.

I am grateful to Fanie De Villiers, who made my thesis speak english. His concern was admirable and I want to thank him for every single language correction he made. There were many of them.

Very special thanks go to my friends and fellows through all of our university studies Lucie and Tomáš. All the countless days and nights we have spent together

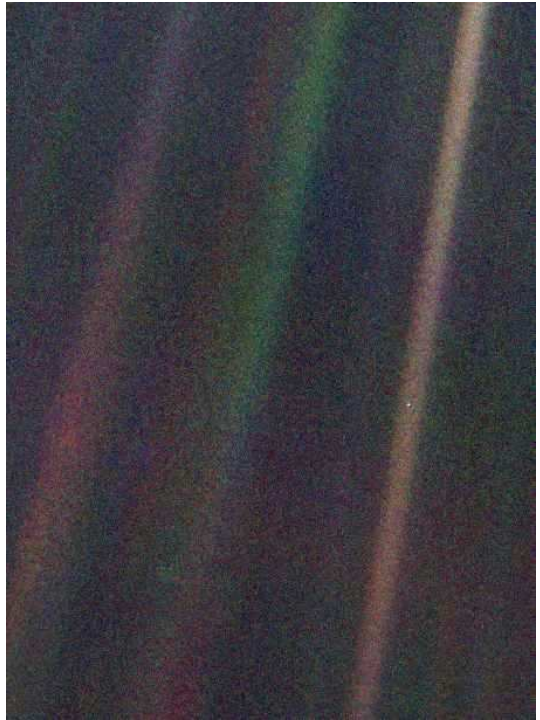
were unforgettable and yes, they still do have red and green flags and their pope smoked dope.

Lucie Jílková read the whole thesis, from the beginning till the end. It was a tough task. Thank You for all the comments, corrections, suggestions, and ironic remarks you made.

One of the biggest thanks goes to Petr, who was with me for the last three wonderful years.

Na závěr bych chtěla poděkovat rodičům, kteří mě vždy nechali jít tam kam jsem chtěla, a i když někdy s hlavou v oblacích, tak s nohama vždy pevně na zemi. This

work has been supported by Student Project Grant at MU (MUNI/A/0968/2009), grant GA ČR GD205/08/H005, and National Scholarship Programme of the Slovak Republic.



The Earth as imaged by Voyager 1 from the distance of more than 6 billion kilometers. Courtesy NASA/JPL.

CONTENTS

Introduction	13
1 Light curves of transiting extrasolar planets	19
1.1 Transits	20
1.2 Wasp-10	24
1.2.1 Observations and data reduction	24
1.2.2 Data analysis	26
1.2.3 Monte Carlo simulations	28
1.2.4 Confidence regions	30
1.2.5 Discussion and conclusion	33
1.3 TrES-3	34
1.3.1 Observations and data reduction	37
1.3.2 Data analysis and confidence regions	37
1.3.3 Discussion and conclusion	38
1.4 Modelling of out-of-eclipse light curves	41
1.4.1 Out-of-eclipse light curve variation	41
1.4.2 KOI-13.01	44
1.4.3 Models of light curves	45
1.4.4 Kepler data analysis	47
1.4.5 Results	50
1.4.6 Discussion and conclusion	52
2 Star–planet interaction	57
2.1 Introduction	57
2.1.1 Ca II H and K lines	59
2.1.2 Mt.Wilson observations	60
2.2 Search for star–planet interaction	61
2.3 Spectroscopic observations and data	64
2.3.1 2.2 m MPG/ESO telescope–Observations and data reduction	64
2.3.2 Keck HIRES archive data	66

CONTENTS

2.3.3	Equivalent width measurements	67
2.4	Statistical analysis of the data sample	67
2.5	Conclusion	78
A	lcquad4.f – parameter determination	81
B	montechyby4.f – Monte Carlo simulation	93
C	Statistical tests	101
C.1	Student’s <i>t</i> -test	101
C.2	Kolmogorov–Smirnov test	102
D	List of exoplanets used in Chapter 2	103
E	List of abbreviations and constants	109
	Bibliography	111
	List of publications	117

INTRODUCTION

When we look at the night sky with our naked eyes, it is possible to see various types of objects, but none of them is an extrasolar planet. Even with a telescope of the usual size, we cannot see any. The main reason for this is the big contrast between the star and the exoplanet orbiting around it and small angular distance of both objects. The ratio of their brightnesses varies with the wavelength of observation and is quite high for visible light, as seen in Figure 1. That is the reason why the first images of exoplanets were made in the infrared region of electromagnetic spectra, where the brightnesses ratio is more favourable. Among the first exoplanets discovered by direct imaging was 2M1207 b—a giant exoplanet of mass $\sim 5 M_J$, orbiting a brown dwarf 2MASSWJ 1207334-393254 at a distance of ~ 55 AU (Chauvin et al., 2004). The image of this exoplanetary system (Figure 2) was obtained from the ground with one of the biggest telescopes (VLT-UT4, instrument NACO).

Extrasolar planets, or in short exoplanets, are planets orbiting stars other than our Sun. In the last two decades more than 800 such objects were discovered (Schneider et al., 2011).¹ Starting with the detection of exoplanets around a pulsar (Wolszczan & Frail, 1992) and followed by the first exoplanet orbiting a solar-type star 51 Peg b (Mayor & Queloz, 1995), the number of discovered exoplanets is growing almost daily. Not only ground based telescopes, but also space missions like *Kepler* (Borucki et al., 2003) or *CoRoT* (Baglin et al., 2002), should be credited with the discovery of exoplanets.

The range of values describing the characteristics of newly discovered exoplanets could be very diverse with respect to each other or with respect to the solar system planets. To accommodate this a working definition for extrasolar planets has been proposed by the IAU’s Working Group on Extrasolar Planets.² This definition consists of three points.

1. Objects with true masses below the limiting mass for thermonuclear fusion of deuterium (currently calculated to be $13 M_J$ for objects of solar metallicity) that orbit stars or stellar remnants are “planets” (no matter how they formed). The

¹<http://exoplanet.eu>

²<http://www.dtm.ciw.edu/users/boss/definition.html>

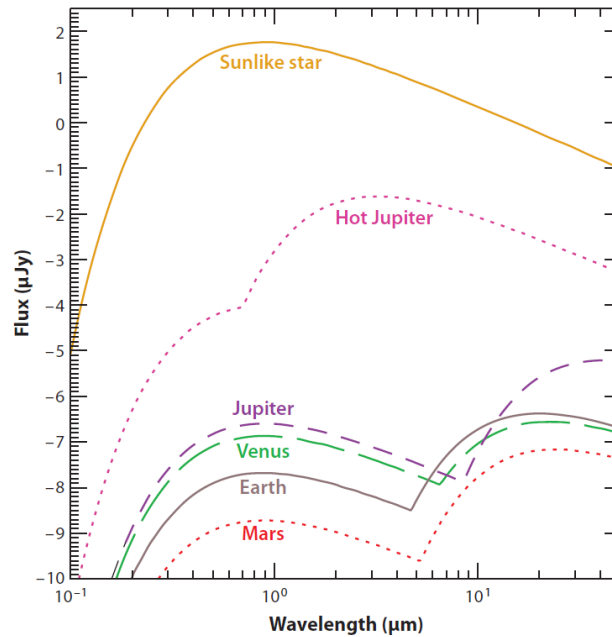


Figure 1: Black body flux in μJy ($1 \text{ Jy} = 10^{-26} \text{ W m}^{-2} \text{ Hz}^{-1}$) of the Sun-like star, Jupiter, Mars, Earth, Venus and hypothetical Hot Jupiter exoplanet (with equilibrium temperature 1600 K and albedo 0.05) as viewed from 10 pc. Two peaks in the spectra of solar system planets are clearly visible. The peak at long wavelength stands for the thermal emission from the planet. The short wavelength peak is caused by a scattered stellar light from the planetary atmosphere. Taken from Seager & Deming (2010).

minimum mass/size required for an extrasolar object to be considered a planet should be the same as that used in our solar system.

2. Substellar objects with true masses above the limiting mass for thermonuclear fusion of deuterium are “brown dwarfs,” no matter how they formed nor where they are located.
3. Free-floating objects in young star clusters with masses below the limiting mass for thermonuclear fusion of deuterium are not “planets,” but are “sub-brown dwarfs” (or whatever name is most appropriate).

Although the methods that allow for the direct observation of an exoplanet are very promising, and the first direct discovery of an exoplanet was soon followed by other images of exoplanets, the majority of exoplanets has been discovered by indirect methods. Each of these methods is sensitive to different types of exoplanets with different orbital parameters. The distribution of discovered exoplanets in the mass–semi-major axis plane, sorted out according to discovery technique, is shown in Figure 3.

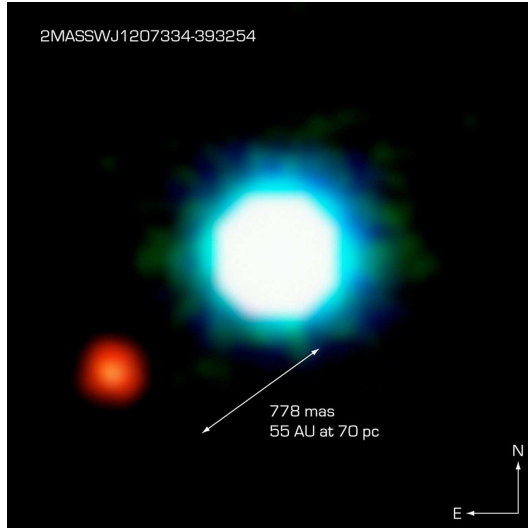


Figure 2: The composite image (H –blue, K_s –green, and L' –red bands) of brown dwarf 2MASSWJ 1207334-393254 (blue object) and exoplanet (red object). Image taken from Chauvin et al. (2004).

Figure 3 shows that most of the exoplanets have been discovered by either one of two methods: *radial velocity technique* or *transit technique*.

Radial velocity (hereafter RV) technique is an indirect spectroscopic method based on the measurement of the change of stellar radial velocity, which is a result of the reflex motion of the star around the common star–planet barycenter. This velocity can be determined from the shift of the absorption lines in the spectrum of the parent star. The shifted spectral lines of the moving star (because of the unseen companion) arise as a consequence of the Doppler effect. The majority of exoplanets have been discovered by the RV technique, see Figure 3. The sample of exoplanets discovered by the RV method suffers from a number of selection effects. The detection method is only suitable for bright stars of specific spectral types with a sufficient number of sharp spectral lines in their spectra. Stars of spectral type F, G, K and M are especially suited for this detection method. To avoid any misinterpretation during the searching for and confirmation of an exoplanet, suitable candidate stars are selected. Since stellar activity can cause features that cannot be eliminated to appear in star spectra, stars showing low-activity are selected. The RV method itself is strongly biased towards the discovery of massive planets in close-in orbits and high inclinations. Such systems cause the biggest radial velocity amplitude.

The second method–transit technique–measures the decrease in flux of light coming from the star, caused by a planet transiting in front of the stellar disk and is described in more detail in Chapter 1. This second method is unfortunately not suitable for all exoplanetary systems, but is limited only to those which are properly oriented

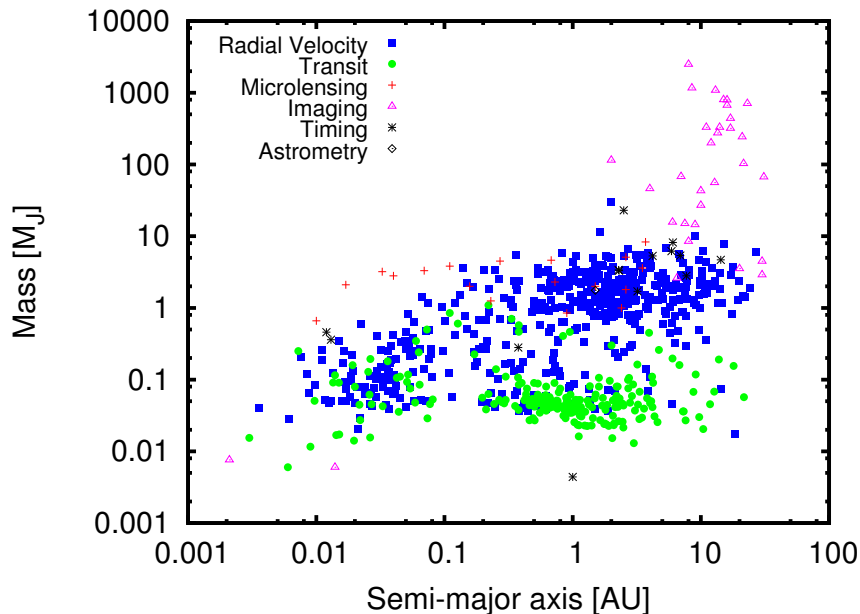


Figure 3: Extrasolar planets distributed according to their semi-major axis and mass. Detection method of each exoplanet is drawn with different color. Data taken from exoplanet encyclopaedia in March 2013 (Schneider et al., 2011).

with respect to the observer. Among the most pronounced selection effects belong the discoveries of big planets on close-in orbits. This method also favours the smaller host stars.

Both these methods are especially suitable for the discovery of close-in and massive planets. As a result, about 20% of discovered exoplanets are Jupiter-like planets orbiting within 0.1 AU from their parent star. These exoplanets are called *Hot Jupiters* since they have similar mass to Jupiter, although their spectral properties are completely different. Their close proximity to the parent star is responsible for the high level of insolation the planet receives and the consequent high atmospheric temperatures of Hot Jupiters. The predicted temperatures exceeded 1 000 K and were confirmed by *Spitzer Space Telescope* observations (Seager et al., 2005). This group of exoplanets is clearly visible in the left part of Figure 3.

The biggest disadvantage of the RV discovery technique is that the planetary mass cannot be determined. We can only calculate the product of the mass, M_p , and the inclination, i , of the planetary orbit $M_p \sin i$, which could give us the minimum mass only. So, we do not know the real masses for most of the extrasolar planets discovered by RV technique. This is not true for exoplanets discovered by the transiting method. This method allows us to determine the orbital inclination i and the planetary radius

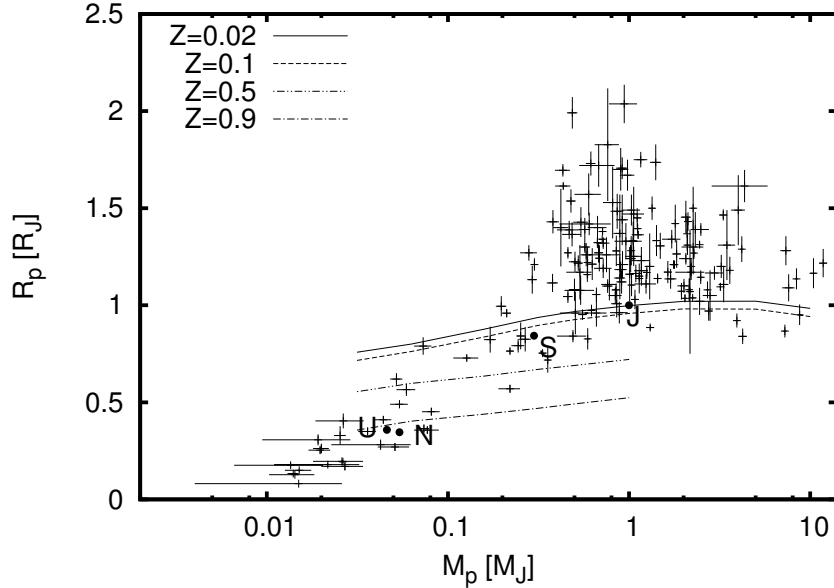


Figure 4: Mass–radius diagram for selected transiting exoplanets. The points stand for measured data of individual exoplanets. Four lines indicate theoretical mass–radius relationships for different heavy element enrichment $Z = 0.02, 0.1, 0.5, 0.9$. $Z = 0.02$ is the solar content of heavy elements. Models for the system correspond to the age 5 Gyr and were taken from Baraffe et al. (2008). Letters J, S, U, and N stand for the solar system planets Jupiter, Saturn, Uranus, and Neptune, respectively.

R_p . The combination of these two methods allow us to determine the mass and the radius of the planet.

The radius and mass of a planet are the most important characteristics for further study of the density, interior structure, equation of state or composition of exoplanets. With the first determination of planetary masses and radii, a discrepancy between the observation and theory arose. A significant fraction of the transiting exoplanets has larger radii than predicted by the theoretical models. Figure 4 shows a mass–radius diagram for selected transiting exoplanets and giant solar system planets. Model curves for several values of heavy element enrichment show the theoretical relation between the mass and radius of the planets (Baraffe et al., 2008). Figure 4 shows that the radius of large portion of exoplanets deviate significantly from the model.

New approaches for the modelling of the mass–radius relation had to be applied. Because most of the transiting planets were Hot Jupiters, the irradiation effects from the host star were taken into account. To fully understand the so called *radius anomaly*, many mechanisms have been proposed. They include additional heat sources (Showman & Guillot, 2002), enhanced opacities of the planetary atmospheres (Burrows et al.,

2007) or tidal effects (Bodenheimer et al., 2001). Unfortunately none of these theories has so far been accepted as a unified theory describing all the observed phenomena.

Without any doubt the exoplanets form together with their host stars unique systems, so they cannot be treated separately. The evolution of these objects is closely tied and the closer the objects are to each other, the more pronounced is the mutual influence on each other.

This thesis consists of two main parts. In Chapter 1 we study light curves of transiting exoplanets. Sections 1.2 and 1.3 deal with the analysis of transits of extrasolar planets Wasp-10 b and TrES-3 b. We determine the orbital and physical characteristics of these planetary systems. Section 1.4 is focused on the modelling of the out-of-eclipse light curve of KOI-13.01, which is an exoplanet candidate discovered by the Kepler mission. Models are compared with data. Chapter 2 is devoted to the search for enhanced chromospheric activity of the stars harboring exoplanets. We perform statistical tests to determine whether there is a connection between the close-in exoplanets and the activity of the host star

CHAPTER 1

LIGHT CURVES OF TRANSITING EXTRA-SOLAR PLANETS

One of the most important groups among the extrasolar planets are the transiting exoplanets. Their name is derived from the orientation of their orbit with respect to the observer. The inclination of the orbit is so fortunate that the planet is seen as passing in front of the parent star. The planet blocks part of the light coming from the star which can be observed as a dip in the light curve—the so called *transit*. The light curve shows more features than just those caused by a transit. After the transit event, the flux coming to the observer is continuously increasing. This effect is known as *out-of-eclipse* light curve variation. When the exoplanet is obscured by the star, a drop in the light curve, called *occultation* or *secondary eclipse*, occurs. This phenomenon is caused by the loss of the light coming from the exoplanet itself. All these features are illustrated in Figure 1.1.

Currently there are more than 300 known transiting exoplanets (Schneider et al., 2011). Two separate teams, Henry et al. (2000) and Charbonneau et al. (2000), ob-

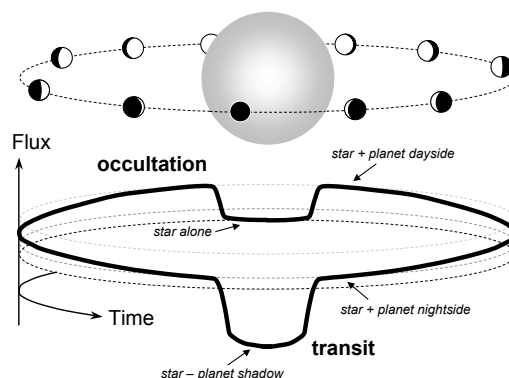


Figure 1.1: Schematic diagram of all light curve features. Transit, occultation and out-of-eclipse variation are shown. Taken from Winn (2011).

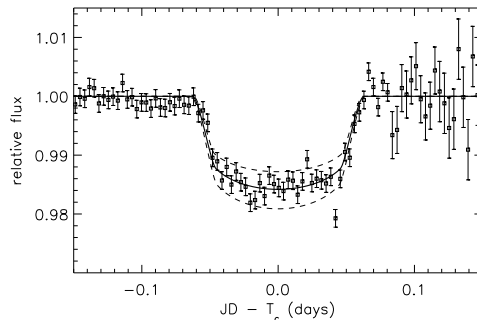


Figure 1.2: First observation of transit – extrasolar planet HD 209458 b. Taken from Charbonneau et al. (2000).

served the first transit of the HD 209458 system. The first light curve is shown in Figure 1.2.

An occultation is especially observable in the infrared part of the spectrum and was first observed with the Spitzer Space Telescope at a wavelength of $8\ \mu\text{m}$. Two discoveries were announced simultaneously: Charbonneau et al. (2005) observed an occultation of TrES-1 b (Figure 1.3) and Deming et al. (2005) observed an occultation of HD 209458 b. In the case of a circular orbit, both a transit and an occultation occur. If the orbit is eccentric, it is possible that only one of these events might occur in the light curve.

To observe changes in the out-of-eclipse part of the light curve – the part between the transit and occultation – very precise photometry is required. That is why the first observation of out-of-eclipse variations was made with the Spitzer space telescope (Knutson et al., 2007). One of the first light curve variations in system HD 189733 is given in Figure 1.4.

Transiting exoplanets are unique sources for studying the properties of exoplanets, like the planet’s radius, mass, orbit, temperature and atmospheric constituents.

1.1 Transits

The most pronounced feature in the light curve of a transiting exoplanet is without any doubt the transit. Figure 1.5 schematically depicts the phases of the transit – the four contacts of the transit and the corresponding shape of the light curve. The first/fourth contact occurs when the disk of the planet reaches/leaves the edge of the star. The second/third contact occurs when the whole disk of the planet is within the disk of the star. The most important parameters are also indicated in Figure 1.5: the duration of the whole transit event T_D , the depth of the transit ΔF , and the duration of the central part of the transit T_M . In most cases, the central part of the transit is

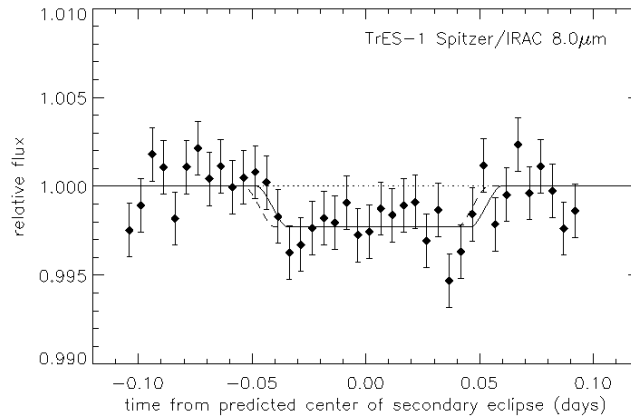


Figure 1.3: The first detection of an occultation. Depicted is the light curve of the TrES-1 system obtained with the Spitzer space telescope at a wavelength of $8\ \mu\text{m}$. (Charbonneau et al., 2005).

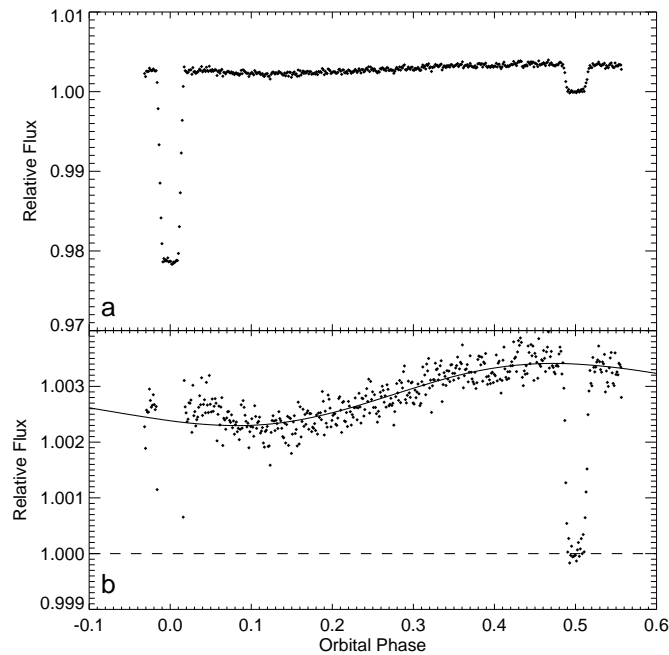


Figure 1.4: Phase variation of the light curve of the HD 189733 system at $8\ \mu\text{m}$ taken with the Spitzer Space Telescope. *Top:* Both transit and occultation visible. *Bottom:* Detail of the occultation and out-of-eclipse variation; the transit is omitted. (Knutson et al., 2007).

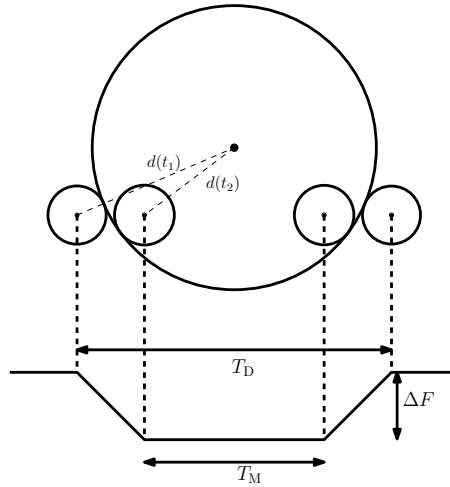


Figure 1.5: Schematic diagram of a transit event and the corresponding light curve. Depicted are the depth of the transit ΔF , duration of the transit T_D (between first and fourth contact) and the duration of the central part of the transit T_M (between second and third contact). $d(t_1)$ and $d(t_2)$ are the distances between the centres of the star and planet at times t_1 and t_2 .

indistinguishable from the ingress and egress parts of the light curve. In the simplified case, if the brightness is uniform over the stellar disk, the ratio of the planet and star radii can be determined from the depth of the transit:

$$\frac{\Delta F}{F_*} = \frac{R_p^2}{R_*^2}, \quad (1.1)$$

where ΔF is the drop in the flux during the transit, F_* is the flux from the star, R_p is the radius of the planet and R_* is the radius of the star.

The transit duration can be expressed as:

$$T_D = \frac{P}{\pi} \arcsin \left(\frac{\sqrt{(R_* + R_p)^2 - a^2 \cos^2 i}}{a(1 - \cos^2 i)^{1/2}} \right), \quad (1.2)$$

where P is the orbital period of the planet, a is the semi-major axis, and i is the inclination of the orbit. Expression (1.2) was derived under the assumption that the orbit is circular. This assumption was used in the subsequent analysis of the shape of the transit light curve and is valid for most Hot Jupiters. To describe the course of the light curve during the transit as a function of time, we followed the methods from a paper by Mandel & Agol (2002). Throughout the modelling process, the planet was assumed to be an opaque dark sphere, which obscures the light of a spherical star.

In the first case, a star of uniform brightness was assumed. As the planet moves in its orbit, it is occulting a bigger and bigger part of the stellar disk, as seen from the

observer's perspective. The resulting ratio of the obscured and unobscured flux F_r can be expressed as:

$$F_r(p, z) = 1 - \lambda(p, z), \quad (1.3)$$

where parameters z and p are defined as $z = d/R_*$, where d is the distance of the planetary and stellar centres, and $p = R_p/R_*$ respectively. $\lambda(p, z) = 0$ is a function describing the position of the planetary disk with respect to the stellar disk. $\lambda(p, z) = 0$ when the planet is outside the stellar disk and $\lambda(p, z) = p^2$ when the planet is fully within the stellar disk. In the case, when the planet is only partially seen within the stellar disk ($|1 - p| < z \leq 1 + p$), λ could be expressed as:

$$\lambda(p, z) = \frac{1}{\pi} \left[p^2 \kappa_0 + \kappa_1 - \sqrt{\frac{4z^2 - (1 + z^2 - p^2)^2}{4}} \right], \quad (1.4)$$

where $\kappa_1 = \arccos[(1 - p^2 + z^2)/2z]$ and $\kappa_0 = \arccos[(p^2 + z^2 - 1)/2pz]$.

If limb darkening of the host star is assumed—the brightness of the stellar disk is not uniform, the expression for the flux is given by:

$$F(p, z) = \left[\int_0^1 dr 2r I(r) \right]^{-1} \int_0^1 dr I(r) \frac{d[F_r(p/r, z/r)r^2]}{dr} \quad (1.5)$$

where $F_r(p, z)$ is defined in Equation (1.3), r is the normalized radial coordinate on the disk of the star ($0 \leq r \leq 1$), the specific intensity of the stellar disk $I(r)$ is expressed as a function of the μ parameter, which is defined as:

$$\mu \equiv \cos \theta = \sqrt{1 - r^2}, \quad (1.6)$$

where θ is an angle between the line of sight and the normal to the stellar surface. The distribution of the specific intensity can be described by various limb darkening laws. For the analysis of transiting light curves, as described in Section 1.2, the quadratic limb darkening law was used:

$$I(\mu)/I(1) = 1 - c_1(1 - \mu) - c_2(1 - \mu)^2, \quad (1.7)$$

where $I(\mu)$ is the intensity at the place defined by μ , $I(1)$ is the intensity at the center of the disk and c_1 and c_2 are the coefficients of limb darkening. These coefficients represent the properties of the stars itself. They are calculated for the surface gravity $\log g$, effective temperature T_{eff} , metallicity $[M/H]$ and microturbulent velocity v_c of the star. The limb darkening creates the U shape of the transit light curve, see Figure 1.2.

To describe the light curve as a function of time, the planetary orbital parameters must be known and the z parameter can be then expressed as:

$$z = d(t)/r_* = a/r_* \left((\sin \omega t)^2 + (\cos i \cos \omega t)^2 \right)^{1/2}, \quad (1.8)$$

where ω is the orbital frequency, a is the semi-major axis, t is the time measured from the center of the transit and the orbital eccentricity was assumed to be zero. Distance of the planetary and stellar centers as a function of time, $d(t)$, is depicted in Figure 1.5.

This procedure is implemented in the Fortran 77 subroutine `occultquad` (Mandel & Agol, 2002) available at www.astro.washington.edu/agol/. This subroutine was used among other in our Fortran 77 codes `lcquad4.f` and `montechyby4.f` listed in the appendix A and B, respectively. These codes were used in the subsequent analysis of transit light curves of exoplanetary systems Wasp-10 and TrES-3 described in the following section.

1.2 Wasp-10

Wasp-10, alias GSC 02752-00114, is a K5 dwarf star. In 2008 a transiting Hot Jupiter, Wasp-10 b, was discovered on a close-in orbit of ~ 3 days (Christian et al., 2009). The relatively small radius of the star ($\sim 0.78 R_{\odot}$) results in a quite deep transit depth of 33 mmag. Such a high value makes the system one of the best candidates for observations with small aperture telescopes, and is also one of the reasons we decided to observe this system. Christian et al. (2009) determined the planetary radius to be $R_p = 1.28 R_J$, and estimated the rotational age of the star to lie between 600 Myr and 1 Gyr.

Soon after the discovery of Wasp-10 b, the properties of the exoplanet were revisited by Johnson et al. (2009). They used the Orthogonal Parallel Transfer Imaging Camera (OPTIC) on the University of Hawaii 2.2 m telescope at Mauna Kea to cover the whole transit event and they significantly improved the precision of the planetary radius determination. However, contrary to the discovery paper, they determined a very different radius for the planet: $R_p = 1.08 R_J$, which is 16 % smaller than the value given in the discovery paper. The origin of the discrepancy was not entirely clear.

Given the knowledge available at the time, we acquired four full transit events of transiting exoplanetary system Wasp-10. Our goal was to revisit the system's parameters, and especially to determine the planetary radius. All the procedures and techniques we used throughout the data analysis are described in the following Subsections (1.2.1–1.2.4).

1.2.1 Observations and data reduction

We observed four full transits of extrasolar planet Wasp-10 b (Krejčová et al., 2010) with the Newton 508/2500 mm telescope located at the Stará Lesná observatory (High Tatra Mountains, Slovakia). The telescope was equipped with a SBIG ST-10XME (KAF-3200ME chip) CCD camera, and the observations were carried out in the R

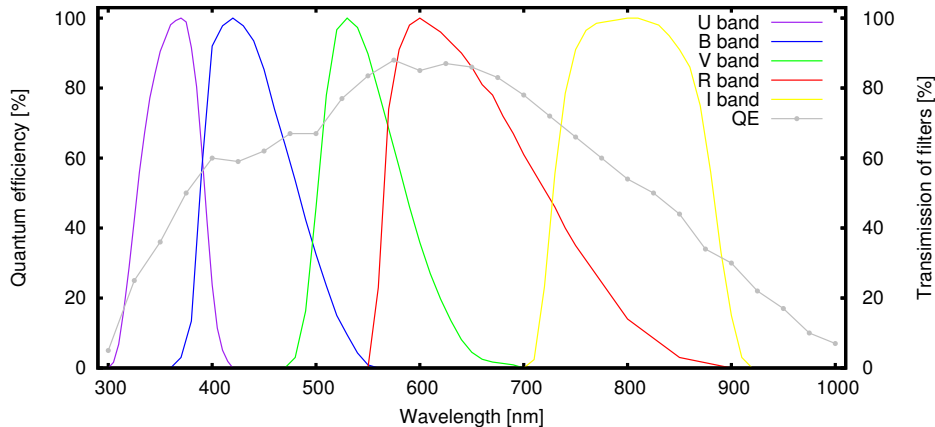


Figure 1.6: Quantum efficiency of the chip KAF-3200ME and the transmissivity of individual filters *UBVRI*, used with the 50 cm telescope located in Stará Lesná in Slovakia, for the observation of exoplanetary system Wasp-10. Quantum efficiency is displayed with grey line – left vertical axis, the transmissivity of the filters in corresponding colours – right vertical axis. Transmission curves (Bessell, 1990) are taken from the Asiago Database on Photometric Systems (ADPS).¹

filter (Johnson–Cousins *UBVRI* system). The characteristics of the CCD camera and the filters that it was equipped with are depicted in Figure 1.6. More detailed information about observations, including the date of observation, number of frames taken each night and their exposure times are summarized in Table 1.1.

The standard calibration procedure, including bias, dark frame, and flat field correction, was applied to all CCD frames. Aperture photometry was performed using the C-munipack software package².

For the standard photometry process, one comparison star and multiple check stars are usually selected in the observing field. However, a single comparison star can suffer various imperfections, e.g. hot pixels or cosmic ray particles captured within the star aperture. All these effects could be indistinguishable from each other and could influence the accuracy of photometry. Therefore, instead of using a single comparison star, we carefully selected several suitable stars in the field and created from them a single “artificial comparison star”. Using this procedure (in the literature called *ensemble photometry*), possible negative effects introduced by the use of a single comparison star could be suppressed. The field stars used for calculating an artificial comparison star were selected based on their spectral type, colour and signal-to-noise ratio.

Calculations leading to the creation of the artificial comparison star were performed as follows. For each of the selected stars, its flux was calculated from its magnitude

¹<http://ulisse.pd.astro.it/Astro/ADPS/>

²<http://c-munipack.sourceforge.net>

Table 1.1: Information about our Wasp-10 observation. Observatory: G1, Stará Lesná, Slovakia; latitude: $20^{\circ}17'21''$ E, longitude: $49^{\circ}09'06''$ N, altitude: 785 m. Equipment: Newton reflector, diameter: 50.8 cm, focal length: 250 cm.

Night	Bandpass	Exp. time [s]	# of frames	Mid-transit time [HJD]	Epoch
4/5.11.2008	<i>R</i>	30	357	2454775.37589	135
31.8./1.9.2009	<i>R</i>	20	520	2455075.37075	232
4/5.10.2009	<i>R</i>	30	355	2455109.39060	243
7/8.10.2009	<i>R</i>	30	350	2455112.48453	244

(using Pogson’s equation). Then the mean of the flux of this sample of stars was calculated for each frame separately. The resulting average value was converted back into magnitudes and used in the photometry process. With this technique a 1σ accuracy of about 3–5 mmag per 1 CCD exposure was obtained, depending on observing conditions.

The resulting light curves were also linearly detrended. The out-of-transit data were used to determine the slope of the line and were consequently applied to the light curves.

All four observed transit light curves of exoplanetary system Wasp-10 are plotted in Figure 1.7 together with the errorbars determined from the aperture photometry.

1.2.2 Data analysis

The light curve of transiting exoplanet provides us with information about the physical and orbital parameters of the system. Using data we obtained, we were able to derive some of them.

The orbital period, P_{orb} , was determined by a linear fit according to the following equation for the known mid-transit times $T_c(E)$ and the epoch E :

$$T_c(E) = T_c(0) + EP_{\text{orb}}, \quad (1.9)$$

where $T_c(E)$ is the mid-transit time for the epoch E (epochs of the observations are given in Table 1.1) and $T_c(0)$ is the mid-transit time for $E = 0$. We combined our measured data with the mid-transit times from previous studies and from the Exoplanet Transit Database–ETD (Poddaný et al., 2010). The resulting orbital period of exoplanet Wasp-10 b is given in Table 1.2.

In order to determine the other parameters of the system, the FORTRAN 77 code `1cqquad4.f` was written. The code is presented in Appendix A of this work. This code

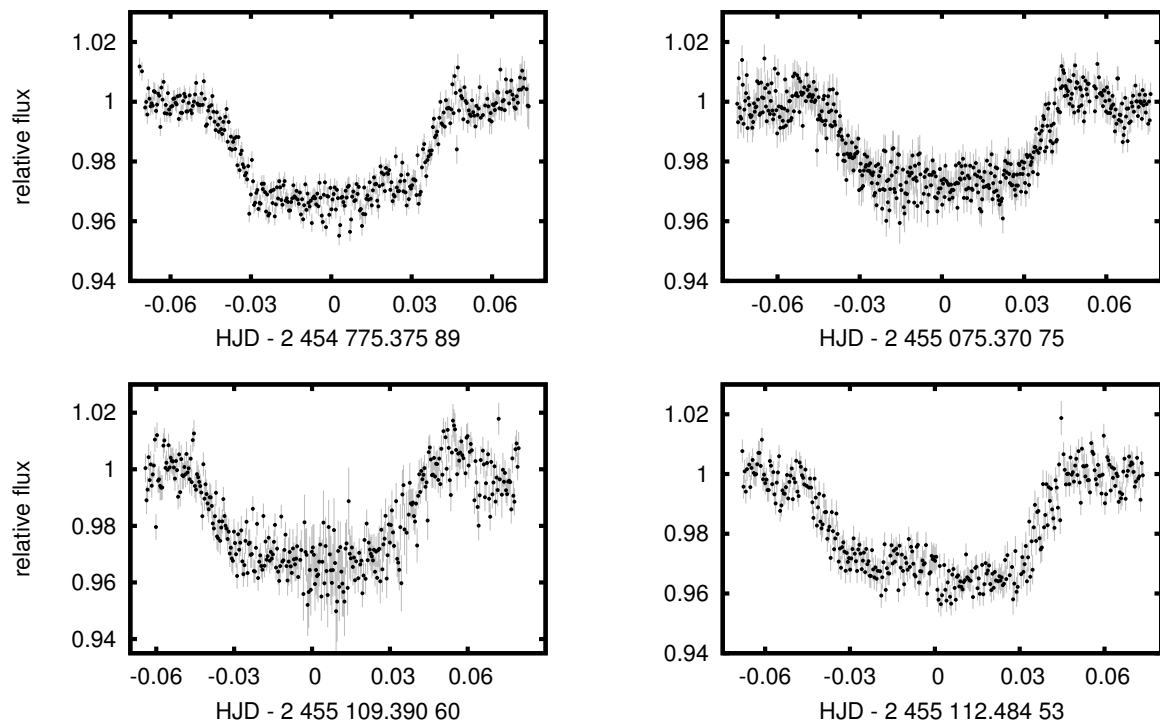


Figure 1.7: Observations of light curves of the transiting exoplanet Wasp-10 b. Data were taken at Stará Lesná observatory (Slovakia) during 4 nights: from top left 04/11/08, 31/08/09, 04/10/09 and 07/10/09 (dd/mm/yy).

finds the best synthetic light curve which best match the observed data as well as the corresponding system parameters. We searched for the optimal values of the following parameters: planet to star radius ratio R_p/R_* , inclination i , the mid-transit time T_c , and the star radius to semi-major axis ratio R_*/a . To obtain an analytical transit light curve we used the subroutine `occultquad` from Mandel & Agol (2002) assuming the quadratic limb darkening law in the form stated in Equation (1.7). The limb darkening coefficients were linearly interpolated from Claret (2000) for the following star parameters: $T_{\text{eff}} = 4675 \text{ K}$, $\log(g) = 4.5 \text{ (cgs)}$ and $[M/H] = 0.0$ (based on the results of Christian et al., 2009). The corresponding coefficients for the R band were found to be $c_1 = 0.5846$ and $c_2 = 0.1689$.

To find a best-fit light curve and the system parameters, we used the downhill simplex minimization method implemented in routine `AMOEB`A (Press et al., 1992). We find the minimum value of the χ^2 function, which we used as an estimator of the goodness of the fit. The χ^2 function is defined as:

$$\chi^2 = \sum_{i=1}^N \left(\frac{m_i - d_i}{\sigma_i} \right)^2, \quad (1.10)$$

where m_i is the model value, d_i is the measured value of the flux, and σ_i is the uncertainty of the i^{th} measurement. The sum in the equation is taken over all of the N measurements. The values of the orbital period of the planet and the limb darkening coefficients were held fixed throughout the minimization process.

We applied this procedure to a single light curve composed of four original transit light curves, so it consists of more than 1 500 individual exposures. This composed light curve together with the best-fit solution is plotted in Figure 1.8. The residuals of the data from the best-fit light curve are displayed in the bottom half of this Figure. The residuals deviate from the best-fit by no more than 2%. Four parameters, obtained as a result of the `1cquad4.f` code are stated in Table 1.2. This table also includes values of planetary radius R_p and stellar radius R_* calculated from our resulting parameters R_p/R_* and R_*/a assuming a known value of semi-major axis $a = 0.0369^{+0.0012}_{-0.0014} \text{ AU}$, which was taken from a spectroscopic study of Christian et al. (2009). The last parameter stated in Table 1.2 is the duration of the transit, T_D , which was calculated making use of Equation (1.2). For comparison parameters obtained by Christian et al. (2009) and Johnson et al. (2009) are given as well.

1.2.3 Monte Carlo simulations

To estimate the uncertainties of the calculated transit parameters, we developed the code `montechyby.f`. It is written in the FORTRAN 77 language and is given in Appendix B. This code uses the Monte Carlo simulation method (hereafter MC) as

Table 1.2: Parameters of the extrasolar system Wasp-10 compared with the results from Christian et al. (2009) and Johnson et al. (2009). R_p is the planet radius, R_* is the host star radius, i is the inclination of the orbit, P_{orb} is the orbital period, and T_D is the transit duration assuming the semi-major axis $a = 0.0369_{-0.0014}^{+0.0012}$ AU taken from Christian et al. (2009).

Parameter	Our work	Christian et al. (2009)	Johnson et al. (2009)
R_p/R_*	0.1675 ± 0.0010	0.1703 ± 0.0029	$0.15918_{-0.00115}^{+0.0005}$
R_*/a	0.0935 ± 0.0011	—	0.086 ± 0.009
i [°]	87.32 ± 0.11	$86.9_{-0.5}^{+0.6}$	$88.49_{-0.17}^{+0.22}$
P_{orb} [days]	$3.092731 \pm 1 \times 10^{-6}$	$3.0927636_{-0.000021}^{+0.0000094}$	—
R_p [R_J]	1.22 ± 0.05	$1.28_{-0.091}^{+0.077}$	1.08 ± 0.02
R_* [R_\odot]	0.75 ± 0.03	$0.775_{-0.040}^{+0.043}$	0.698 ± 0.012
T_D [days]	$0.0974 \pm 8 \times 10^{-4}$	$0.098181_{-0.0015}^{+0.0019}$	$0.092796_{-0.00028}^{+0.00033}$

described in Press et al. (1992). The MC method allows us to calculate the errors of parameters determined in the preceding section by means of the minimization method. The MC method is based on the generation of many artificial data sets, which are supposed to simulate the repeated measurements of a single event. These multiple measurements can subsequently be used for the desired error estimation.

As a first step the characteristics of the residuals (bottom part of the Figure 1.8) distribution had to be determined. We assume the distribution of residuals to be Gaussian for which we calculate its parameters μ (mean) and σ (standard deviation). Around each of the measured value (which was supposed to be the mean value of the distribution), 10^5 points with this distribution were generated.

In the next step 10^4 synthetic light curves were created which represents the multiple measurements. Each of the synthetic light curves has the same number of data points as the original light curve. For generating the synthetic light curve, random sampling with replacement of the previously generated data points was performed. Each of the new light curve was processed following the same procedure as described in Subsection 1.2.2. This means that for each of the light curves, four parameters were determined. As a result we obtained 10^4 sets of synthetic parameters.

If we assume a normal distribution, we can calculate the mean \bar{x} of each of the four parameters:

$$\bar{x} = \frac{1}{N} \sum_{i=1}^N x_i, \quad (1.11)$$

where N is the number of data points in the sample and x_i are the individual measurements. To determine the standard deviation 1σ for each parameter we used the

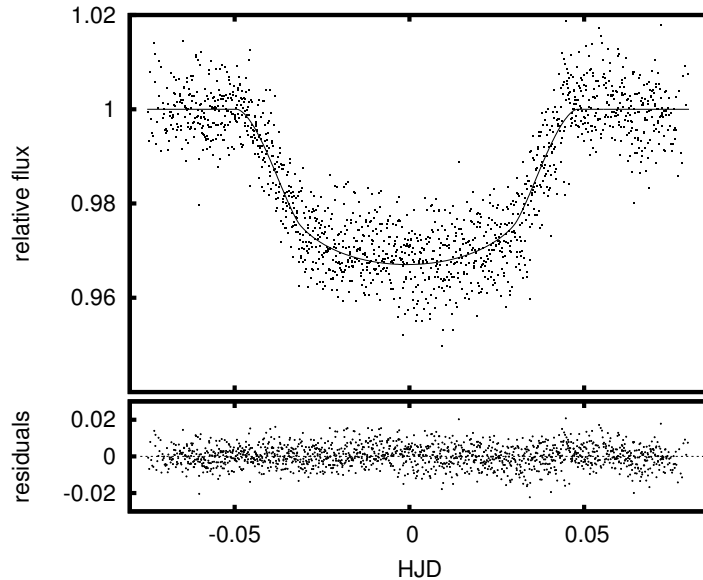


Figure 1.8: *Top:* Composition of 1533 data points from the four nights: 4/11/08, 31/8/09, 4/10/09 and 7/10/09 (dd/mm/yy) of the exoplanetary system Wasp-10 b. The observations were made in the R filter ($UBVRI$ system). The solid line is the best-fit transit curve. *Bottom:* Residuals from the best-fit model.

relation:

$$\sigma = \sqrt{\frac{1}{N-1} \sum_{i=1}^N (x_i - \bar{x})^2}, \quad (1.12)$$

where x_i are the individual measurements and \bar{x} is the mean value of the sample mentioned in Equation (1.11).

The resulting values of the uncertainties for each of the parameters for the extrasolar system Wasp-10 are stated in Table 1.2.

1.2.4 Confidence regions

The minimum value χ_{\min}^2 corresponding to each set of MC parameters determined in preceding Section 1.2.3 was calculated as:

$$\chi_{\min}^2 = \sum_{i=1}^N \left(\frac{m_i - s_i}{\sigma_i} \right)^2, \quad (1.13)$$

where m_i is the original best-fit model value and s_i is the “MC measured” value, N is the number of original measurements. To visualize the distribution of errors

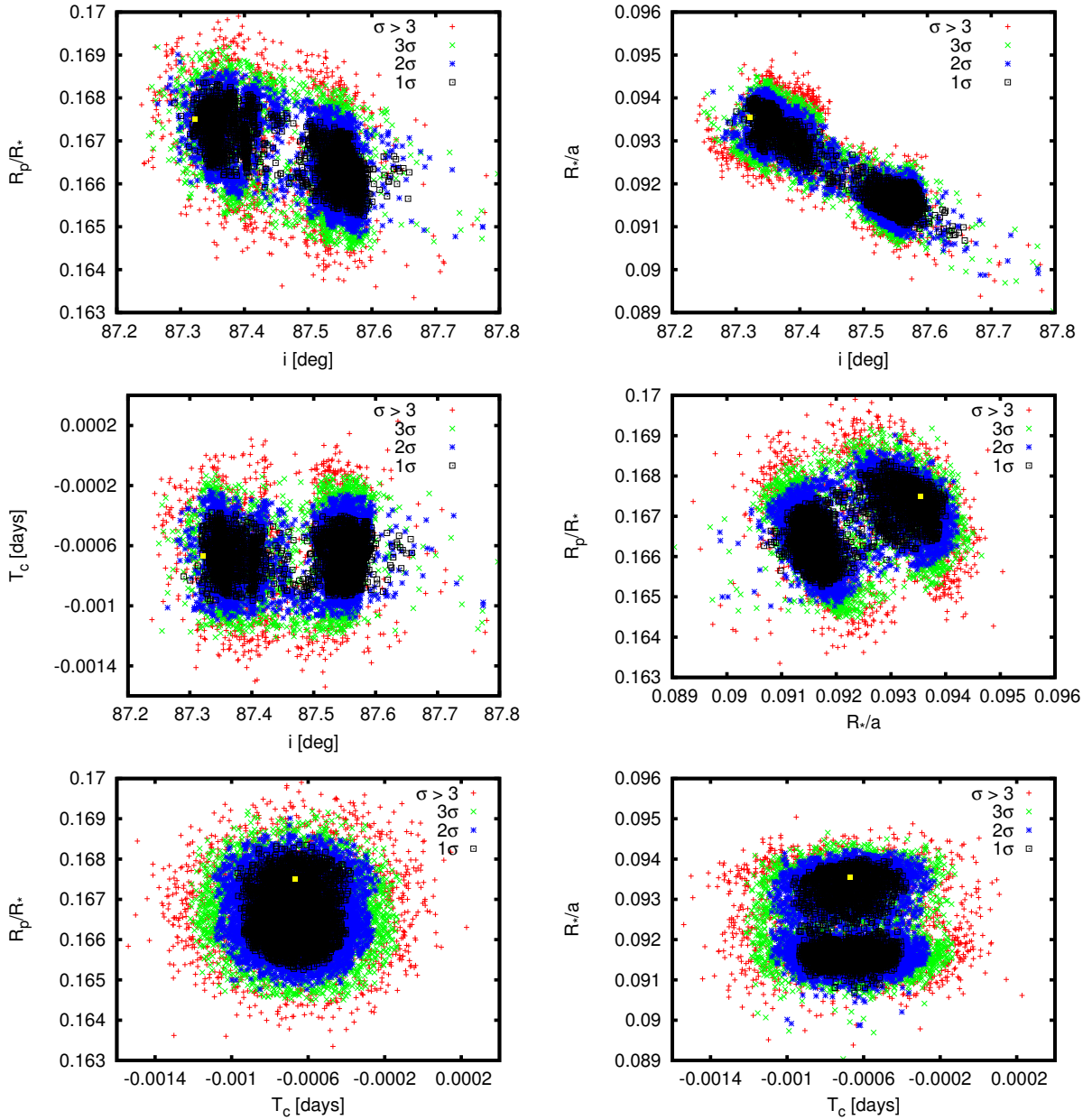


Figure 1.9: Confidence regions for system Wasp-10 depicted as a projection of the 4-dimensional space into a 2-dimensional parameter space. Regions of 1σ , 2σ and 3σ correspond to $\Delta\chi = 4.72$, 9.7 and 16.3 , respectively and are marked in different colours. i is the orbital inclination, R_p/R_* is the planet-to-star radius ratio, T_c is the mid-transit time, and R_*/a is the star radius to semi-major axis ratio. Our best solutions are marked on all plots with a yellow square.

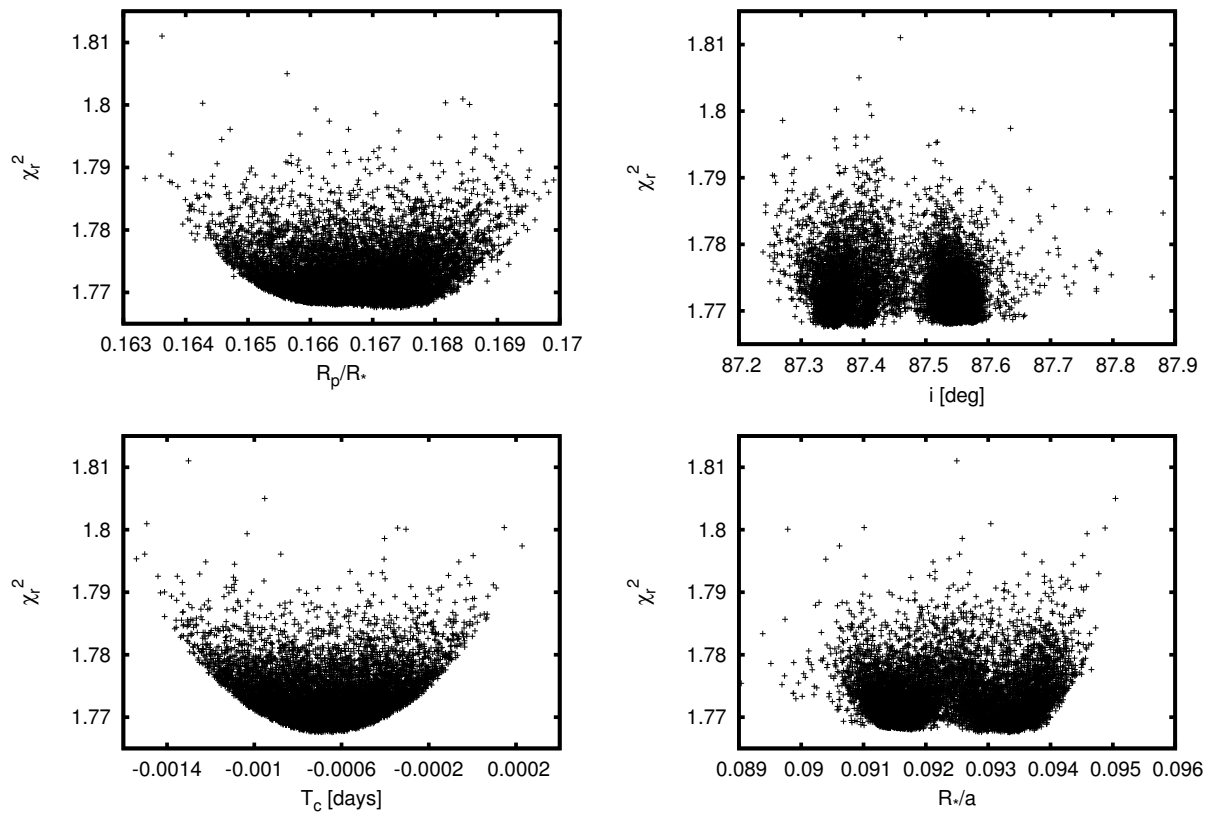


Figure 1.10: Dependence of the generated parameters on the reduced chi square.

of the system parameters, we constructed confidence intervals in 4-dimensional space of parameters R_p/R_* , i , T_c , and R_*/a . Figure 1.9 depicts the projection from 4-dimensional space into 2-dimensional regions. Each of the plots show the relation between two parameters. The different colours of data points indicate the 1σ , 2σ and 3σ regions with corresponding values of $\Delta\chi^2 = \chi_{\min}^2 - \chi_m^2 = 4.72$, 9.7 and 16.3 , respectively (Press et al., 1992). χ_m^2 is the χ^2 of the original best-fit model value stated in Equation (1.10). The yellow square marks the best-fit solution for the system parameters.

Figure 1.10 shows the dependence of the four parameters R_p/R_* , i , T_c , and R_*/a on the reduced χ^2 , respectively. This quantity χ_r^2 is defined as:

$$\chi_r^2 = \frac{\chi_{\min}^2}{N - M}, \quad (1.14)$$

where N is the number of measurements and M is the number of fitted parameters ($M = 4$).

From the shape of the dependence of the parameters in Figure 1.9 it can be seen that the three parameters R_p/R_* , i , and R_*/a correlate with one another, while T_c does not show any significant correlation with other parameters. The shape of the confidence regions show us the important properties of the determined parameters. Two separate concentrations of points in Figure 1.9 indicate two possible solutions for the system parameters. As can be seen in the figure, our determined parameters lie at the border of 1σ region in one of these concentrations. The second region correspond to slightly higher value of inclination and smaller values of planetary and stellar radius.

1.2.5 Discussion and conclusion

In this section the analysis of four full transit observations of exoplanet Wasp-10 b was presented. The composition of all four light curves together with the best-fit model light curve is plotted in Figure 1.8. The parameters of the system R_p/R_* , R_*/a , i , P_{orb} , and T_D were determined and are listed in Table 1.2. These are compared with the previously published results by Christian et al. (2009) and Johnson et al. (2009). The most important result of our work was the determination of the planetary radius $R_p = (1.22 \pm 0.05) R_J$ (assuming a semi-major axis of $a = 0.00369_{-0.0014}^{+0.0012}$ AU Christian et al., 2009). The value of the planetary radius that we determined is in agreement with the previously published data from Christian et al. (2009) rather than with the results of Johnson et al. (2009).

Our results were summarized in Contributions of the Astronomical Observatory Skalnaté Pleso in the paper Krejčová et al. (2010).

Independent of our work, Dittmann et al. (2010) presented their own photometric measurements of one transit of exoplanet Wasp-10 b. The observation was made with

the University of Arizona’s 1.55 m Kuiper telescope (located on Mount Bigelow, USA) using an Arizona-*I* filter. They found the value of the planetary radius to be $R_p \sim 1.2 R_J$, which is in close resemblance with the value presented by Christian et al. (2009) and also with our value.

Subsequently, our data of Wasp-10 b were used in the study of Maciejewski et al. (2011a). This study focused on the search for transit timing variations (TTV) using nine transit light curves. TTV’s with an amplitude of ~ 3.5 min were found. This was interpreted as indicative of the existence of a third body (second exoplanet) in the system. The mass of the new exoplanet was supposed to be $M_p \sim 0.1 M_J$, with orbital period $P_{\text{orb}} \sim 5.23$ days, which is close to the outer 5:3 mean motion resonance.

The host star shows brightness variability that could be caused by starspots. Smith et al. (2009) refined the period of rotation to be $P_{\text{orb}} = (11.95 \pm 0.05)$ days. The spots on the surface could generally lead to an overestimation of the transit depth and planetary radius.

Maciejewski et al. (2011b) continued with the study of Wasp-10 taking starspots into account. They analysed four new transits of Wasp-10 b and refined the parameters of the system. The newly determined value of planetary radius $R_p = 1.03_{-0.03}^{+0.07} R_J$ is in close agreement with the radius determined by Johnson et al. (2009).

Soon after, Sada et al. (2012) published the analysis of a transit light curve observation of the exoplanet Wasp-10 b. They used the Kitt Peak National Observatory (KPNO) 2.1 m telescope (*J* band) and the VC (Kitt Peak Visitor’s Center) telescope (*z'* band). Their estimate of the planetary radius (in *J* band) is in close agreement with Johnson et al. (2009).

Very recently Barros et al. (2013) presented a consistent analysis of 22 previously published light curves of Wasp-10 b (including our data from Stará Lesná Observatory) as well as eight new light curves, obtained with the Faulkes Telescope North and with the Liverpool Telescope. The hypothesis accounting for a second exoplanet in the system was rejected and stellar variability caused by starspots was confirmed.

To compare the resulting values of the radius of exoplanet Wasp-10 b, we plotted our results together with the results from Maciejewski et al. (2011b) in Figures 1.11 and 1.12. These figures illustrate the mass–radius diagram for selected transiting extrasolar planets. Model light curves for different levels of heavy element enrichment are added. Figure 1.11 represents the model without irradiation. Figure 1.12 shows the model with irradiation of the planet from the star at 0.045 AU.

1.3 TrES-3

This section deals with the analysis of a light curve of the transiting extrasolar planet TrES-3 b. The procedures used for the processing of the data of system Wasp-10

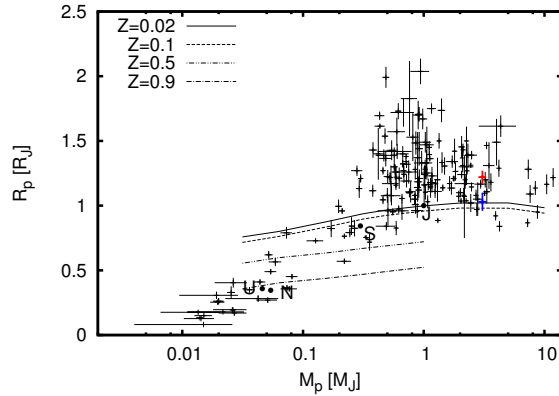


Figure 1.11: Mass–radius diagram for selected transiting exoplanets. The points represent measured data of individual exoplanets. The four lines indicate theoretical mass–radius relationships for different heavy element enrichments $Z = 0.02, 0.1, 0.5, 0.9$. $Z = 0.02$ is solar content of heavy elements. Models for the system correspond to an age of 5 Gyr and were taken from Baraffe et al. (2008). The red cross marks the value of the radius that we determined in this study and the blue cross indicates the results from Maciejewski et al. (2011b). Giant solar system planets Jupiter, Saturn, Uranus, and Neptune are marked with letters J, S, U, and N, respectively.

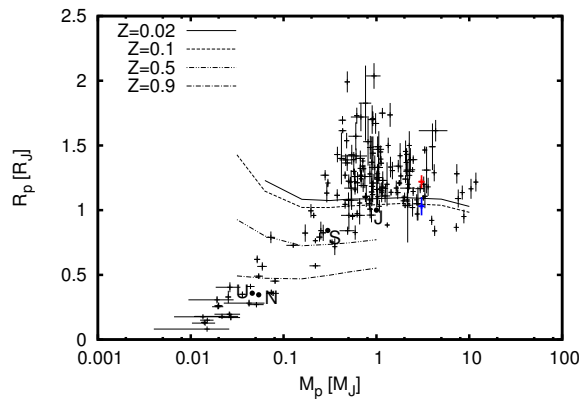


Figure 1.12: Mass–radius diagram for selected transiting exoplanets. The points represent measured data of individual exoplanets. The four lines indicate theoretical mass–radius relationships for different heavy element enrichments $Z = 0.02, 0.1, 0.5, 0.9$. $Z = 0.02$ is solar content of heavy elements. Models for the system correspond to an age of 5 Gyr, they assume the planet is irradiated by a star in the distance of 0.045 AU and were taken from Baraffe et al. (2008). The red cross marks the value of radius that we determined in this study and the blue cross indicates the results from Maciejewski et al. (2011b). Giant solar system planets Jupiter, Saturn, Uranus, and Neptune are marked with letters J, S, U, and N, respectively.

obtained with the 50 cm telescope described in the previous section were applied to the much more precise data of TrES-3, obtained with the 2.2 m telescope at Calar Alto Observatory.

TrES-3 b is a transiting Hot Jupiter, orbiting the G dwarf star GSC 03089–00929, with quite a short orbital period of ~ 1.3 days. It was discovered by O’Donovan et al. (2007), who did both spectroscopic and photometric observations. Soon after the discovery, the parameters of the system were revisited by e.g. Sozzetti et al. (2009), Colón et al. (2010), or Gibson et al. (2009). The planet is supposed to be rather massive ($\sim 1.9 M_J$) with a radius of $\sim 1.3 R_J$.

Since the orbit of TrES-3 b is supposed to be circular (O’Donovan et al., 2007), the search for a secondary eclipse followed soon after the discovery. Winn et al. (2008) attempted to measure six occultation light curves of system TrES-3, but they were unable to detect a secondary eclipse. De Mooij & Snellen (2009) detected a secondary eclipse using the Long-slit Intermediate Resolution Infrared Spectrograph (LIRIS) at the William Hershell telescope at La Palma. Their results were revisited by Croll et al. (2010) whose analysis yielded contradictory values for the depth of the secondary eclipse. Fressin et al. (2010) used the Infrared Array Camera (IRAC) mounted on the Spitzer Space Telescope to observe two secondary eclipses of TrES-3 in four IRAC channels (3.6, 4.5, 5.8 and 8.0 μm).

Seven transits of TrES-3 obtained via the NASA EPOXI Mission of Opportunity, were presented by Christiansen et al. (2011). They refined the parameters of the system and also mentioned the long-term variability of the light curve, caused by star spots. Later, Turner et al. (2013) observed nine primary transits of TrES-3 in several optical and near-UV photometric bands from June 2009 to April 2012 in order to detect its magnetic field. The authors determined the upper limit for the magnetic field strength of TrES-3 b to be between 0.013 and 1.3 G. They also presented a refinement of the physical parameters of TrES-3 b and a the first published near-UV light curve. The planetary radius was derived from the near-UV measurements to be $R_p = 1.386^{+0.248}_{-0.144} R_J$. This value is consistent with the planetary radius determined in the optical part of the spectrum. Kundurthy et al. (2013) present the observation of eleven transits of TrES-3 b, which span over 2 years. They estimated the system parameters to be consistent with previous estimates and they searched for transit timing and depth variations. Unfortunately, they did not reveal any evidence for transit timing variations, but they were able to rule out super-earth and gas giant companions in low order mean motion resonance with TrES-3 b.

Table 1.3: Parameters of the exoplanet system TrES-3. In the second column are results of our analysis, in the third column are results presented in the work of Sozzetti et al. (2009). R_p/R_* is the planet to star radius ratio, R_*/a is the star radius to semi major axis ratio, i is the inclination of the orbit, P_{orb} is the orbital period, R_p is the planet radius, R_* is the host star radius, and T_D is the transit duration assuming a semi-major axis $a = 0.02282^{+0.00023}_{-0.00040}$ AU taken from Sozzetti et al. (2009).

Parameter	Our work	Sozzetti et al. (2009)
P_{orb} [days]	1.306186	$1.30618581 \pm 1 \cdot 10^{-8}$
R_p/R_*	0.1644 ± 0.0047	0.1655 ± 0.002
R_*/a	0.1682 ± 0.0032	$0.1687^{+0.014}_{-0.041}$
i [°]	81.86 ± 0.28	81.85 ± 0.16
R_* [R_\odot]	$0.826^{+0.024}_{-0.03}$	$0.829^{+0.015}_{-0.022}$
R_p [R_J]	$1.321^{+0.077}_{-0.084}$	$1.336^{+0.031}_{-0.037}$
T_D [hours]	1.320 ± 0.023	—

1.3.1 Observations and data reduction

One full transit event of the TrES-3 system was observed in the R filter with the 2.2 m telescope located at the Calar Alto Observatory in Spain ($37^\circ 13' 25''$ N, $2^\circ 32' 46''$ W). A SITe CCD detector (2048×2048 pix) was used at the Ritchey–Chrétien focus. The resulting light curve consists of 157 data points, the exposure times ranged from 30 to 35 s. Data were reduced with the software pipeline developed for the Semi-Automatic Variability Search sky survey (Niedzielski et al., 2003) and aperture photometry was applied.

1.3.2 Data analysis and confidence regions

For the analysis of TrES-3 data, the same procedure as described in Subsection 1.2.2 was used. The codes `lcquad4.f` and `montechyby4.f` were used to determine four system parameters: R_p/R_* (planet to star radius ratio), i (orbital inclination), T_c (centre of the transit) and R_*/a (stellar radius to semi-major axis ratio) and their errors. In these codes the formulae of Mandel & Agol (2002) to model the best-fit transit light curve were used. We used the quadratic limb darkening law. The corresponding limb darkening coefficients were linearly interpolated from Claret (2000) for the following star parameters (taken from work of Sozzetti et al., 2009): $T_{\text{eff}} = 5650$ K, $\log(g) = 4.4$ (cgs), and $[M/H] = -0.19$. The values of the limb darkening coefficients were $c_1 = 0.341$ and $c_2 = 0.318$.

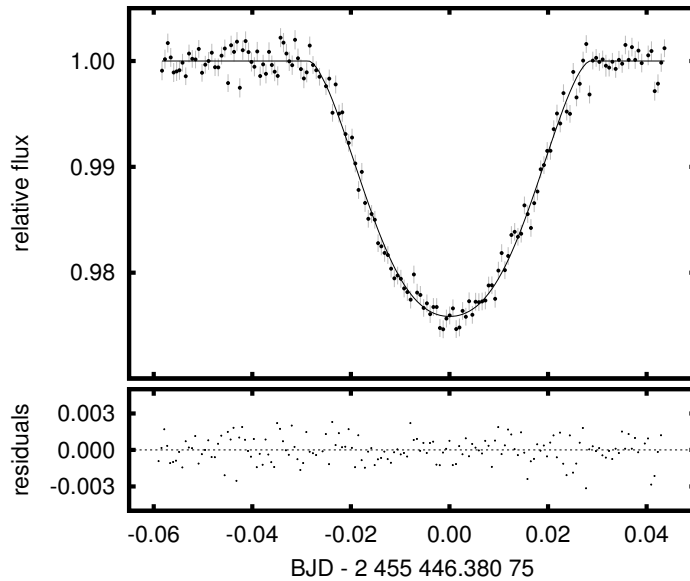


Figure 1.13: *Top:* Transit light curve of TrES-3b obtained on September 9, 2010. The observation was made in filter R on Calar Alto observatory. The solid line is the best-fit transit curve. *Bottom:* Residuals from the best-fit model.

The resulting system parameters are given in Table 1.3. For comparison, the parameters from Sozzetti et al. (2009) are presented as well. The observed data together with the best-fit light curve are depicted in Figure 1.13.

The confidence intervals in 2-dimensional space are given in Figure 1.14. The procedure used to create them was the same as in Subsection 1.2.4. The different coloured data points indicate the 1σ , 2σ and 3σ region with corresponding values of $\Delta\chi^2 = \chi_{\min}^2 - \chi_m^2 = 4.72$, 9.7 and 16.3 respectively. The yellow square marks the best-fit solution for the system parameters. The dependence of the parameters on the reduced chi square value are depicted in Figure 1.15.

1.3.3 Discussion and conclusion

In this section, the light curve of transiting exoplanet TrES-3 was analysed. The four important system parameters were determined: orbital inclination i , planet to star radius ratio R_p/R_* , mid-transit time T_c and stellar radius to semi-major axis ratio R_*/a . It was found that all the values of these parameters were in a good agreement with the previously presented results. The resulting data with the best-fit light curve is shown in Figure 1.13 and the system parameters in Table 1.3. We also studied the

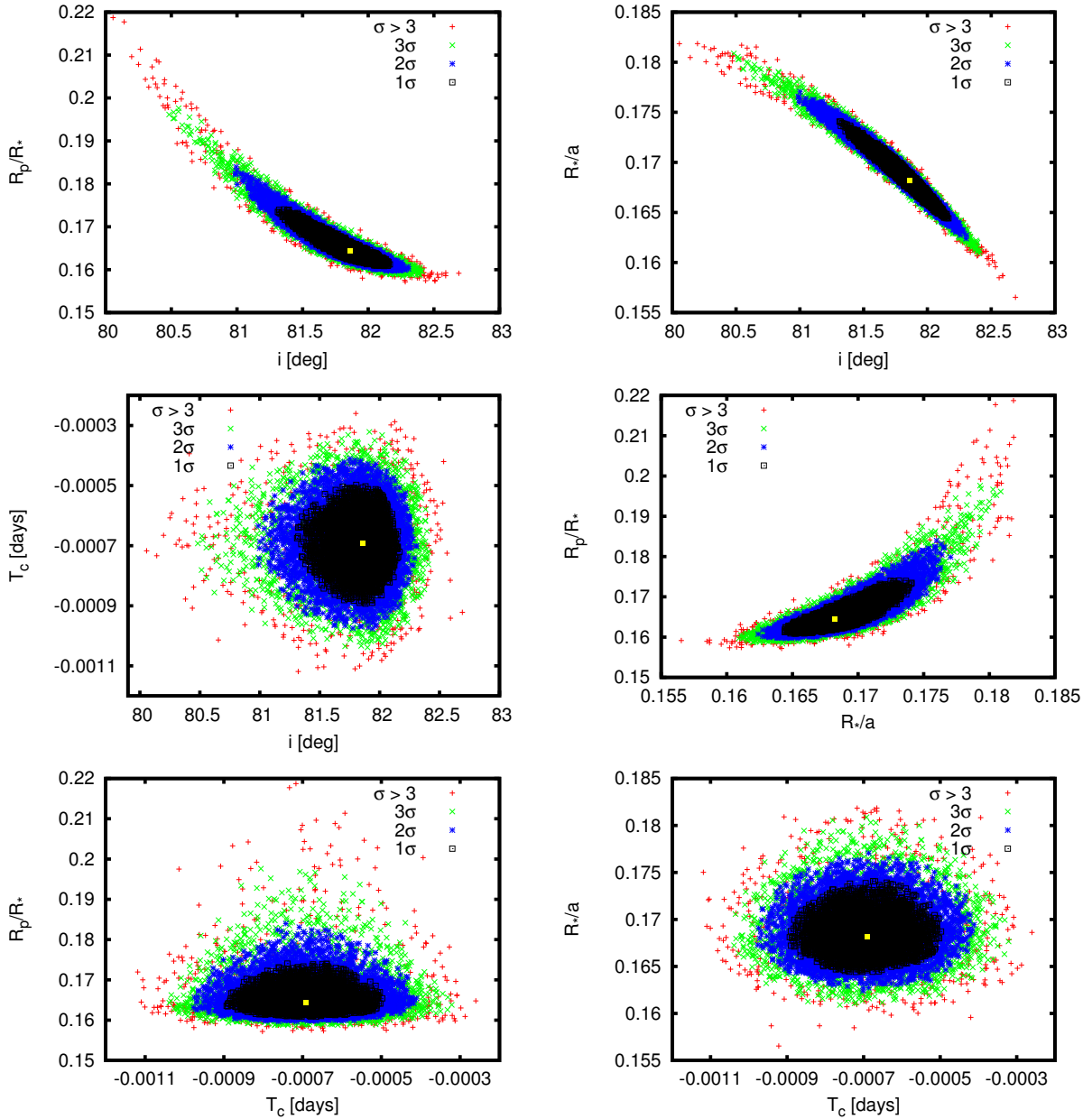


Figure 1.14: Confidence region for system TrES-3 depicted as a projection of the 4-dimensional region into the 2-dimensional parameter space. Regions of 1σ , 2σ and 3σ corresponding to $\Delta\chi = 4.72$, 9.7 and 16.3 respectively, are marked with different colours. The solutions are marked on all plots with a yellow square.

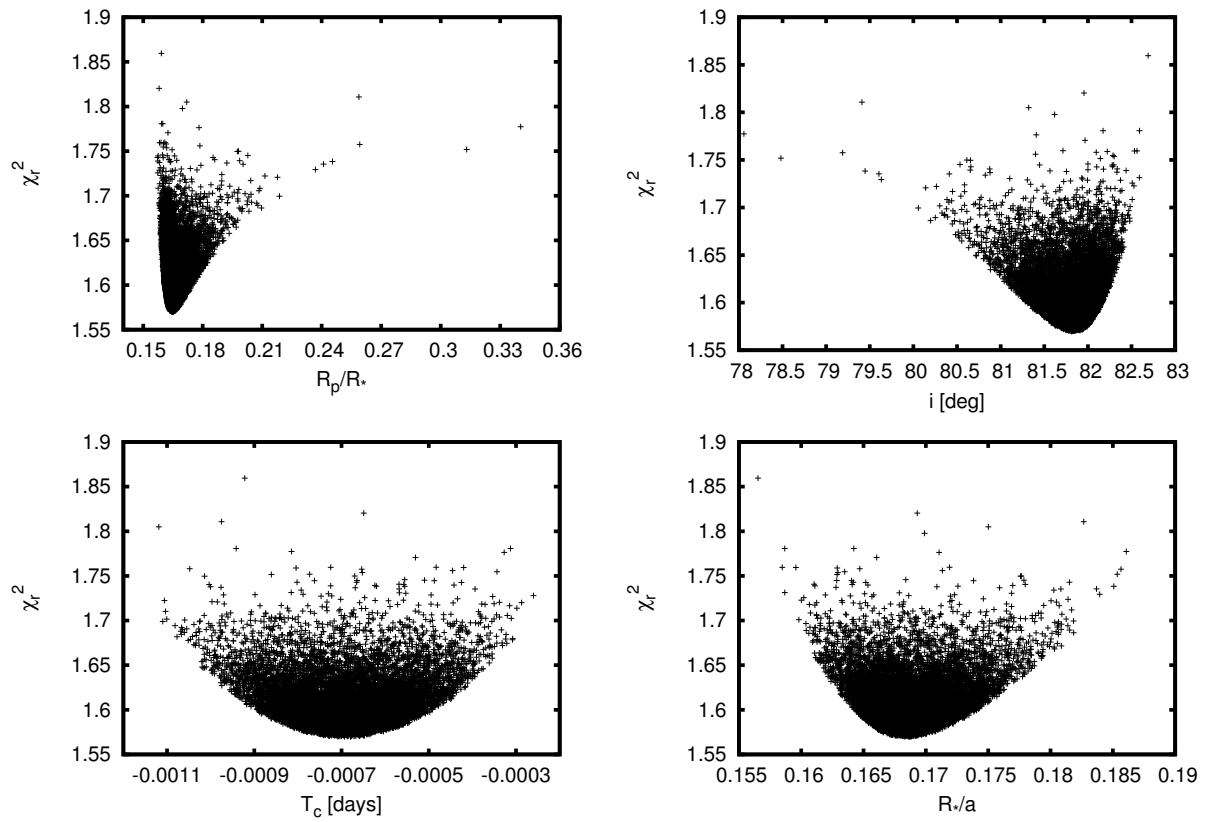


Figure 1.15: Dependence of the generated parameters on the reduced chi square.

confidence intervals of our determined parameters. These are depicted in Figure 1.14 together with the resulting values of the parameters.

The orbital inclination of exoplanet TrES-3 was investigated. TrES-3 b has a low orbital inclination ($\sim 82^\circ$). The lower value of the inclination for the TrES-3 system for the planetary disk to be fully projected onto the stellar disk is defined as:

$$\cos i = \frac{R_* - R_p}{a} = 81.8^\circ, \quad (1.15)$$

where i is the orbital inclination, a is the semi-major axis, R_* and R_p are the radii of the star and planet respectively (assuming the parameters from Sozzetti et al., 2009). In case, when $R_* - R_p < a \cos i < R_* + R_p$, the grazing transit occurs. This means that only part of the planetary disk is obscuring the disk of the star.

The results of this analysis were published in Vaňko et al. (2013).

1.4 Modelling of out-of-eclipse light curves

This section is focused on the modelling of the out-of-eclipse light curves of extrasolar planet candidate KOI-13.01, discovered by the Kepler mission. The main motivation for this study was to put constraints on the Bond albedo of the planet and on the processes of heat redistribution over the planetary surface. The modelled light curves were compared with real data from the Kepler space mission.

1.4.1 Out-of-eclipse light curve variation

Photometric light curve variation in-between the primary and secondary transits (introduced in Chapter 1) can result from multiple effects. These are the ellipsoidal variations caused by the tidal distortion of the star by the gravity of its planet observable mainly in the optical region, tidal distortions of the planet observable mainly in the infrared part of spectra, reflection of the light coming from the host star from the surface of the planet, thermal emission from the planet itself and Doppler boosting (beaming effect). The magnitude of these effects occurring in the light curves of exoplanets is in most cases too small to be observable from the ground. Recently, several space missions like CoRoT or Kepler allowed the observation with required photometric accuracy.

In the following paragraphs the individual effects that produce the observed out-of-eclipse light curve variations are described.

Ellipsoidal variation

Ellipsoidal variation is a feature well known from observations of close-in binary stars. The proximity of these two objects results in tidal forces which change the shapes

of the stars in such a way that they cannot be considered to be spherical anymore. They gain teardrop shapes which are described by the Roche potential theory. For small departures from the sphere the shape can be approximated by a triaxial ellipsoid (hence the name ellipsoidal variation). The maximum surface area of the distorted stars is seen when both objects are viewed side-on. This occurs at the orbital phases 0.25 and 0.75 and the stars appear brightest in these phases. When the elongation of the stars lie in the line of sight, the stars appear to be fainter. The light curve showing this effect is given in Figure 1.16, labeled with letter E. The maximum amplitude at the phases 0.25 and 0.75 can be seen clearly. The transit event (inferior conjunction) occurs at phase 0 and occultation (superior conjunction) at phase 0.5. Ellipsoidal variations of the parent star, caused by an orbiting exoplanet, were first detected in the Hat-P-7 system using Kepler mission data (Welsh et al., 2010). Non-spherical shapes of exoplanet, caused by their stars' gravity distortion, were noted for Wasp-12 b by Li et al. (2010) and studied by Budaj (2011) using a sample of 78 transiting extrasolar planets.

Gravity darkening

Gravity darkening is an effect resulting from a nonspherical shape of the star. Such a star has a larger radius at the equator than at its poles. As a result, the effective gravity changes over the stellar surface. It is highest at the poles and smallest at the subsolar point. Consequently the stellar temperature and brightness is higher at the poles than at the equator as well. The surface temperature as a function of the gravity is described by von Zeipel theorem (von Zeipel, 1924):

$$\frac{T}{T_p} = \left(\frac{g}{g_p} \right)^\beta, \quad (1.16)$$

where g is the normalized surface gravity, β is the gravity darkening coefficient and its value is 0.25 for stars without convective envelopes (case of KOI-13 host star). T_p and g_p are the temperature and gravity at the rotation pole, respectively.

Reflected light

The most pronounced component of the out-of-eclipse light curve is composed of two connected effects. The first one is the light from the host star reflected by the day side of the planetary surface and the second one is the emission of light from the planet itself. The reflected light bears the information about the star and peaks at shorter wavelengths than the thermal radiation from the planet (see Figure 1).

The ratio of the flux reflected from the planet $F_{p,\lambda}(\alpha)$ to the flux coming from the star $F_{*,\lambda}(\alpha)$ can be expressed as:

$$\frac{F_{p,\lambda}(\alpha)}{F_{*,\lambda}} = A_g \left(\frac{R_p}{a} \right)^2 \Phi_\alpha \quad (1.17)$$

where α is a phase angle, a is the distance between the planet and the star, A_g is a wavelength dependent geometric albedo. $\Phi(\alpha)$ is a phase function which, in the simplest case, could be approximated as:

$$\Phi(\alpha) = \frac{1}{\pi} (\sin \alpha + (\pi - \alpha) \cos \alpha) \quad (1.18)$$

which assumes that the planet is a Lambert sphere. A Lambert surface is an ideal surface which scatters light incident on it isotropically—in the same way in all directions. The geometric albedo $A_g(\lambda)$ is the ratio of a planet's flux at zero phase angle (full phase) to the flux from a Lambert disk at the same distance and with the same cross-sectional area as the planet.

The reflected light from the exoplanet as seen by an observer depends on the position of the planet with respect to the central star and the observer. This is described by the *phase angle* α , which is an angle connecting the observer, planet and the star, with the vertex of the angle in the planet. Phase angle is defined so, that $\alpha = 0^\circ$ at superior conjunction (the planet is behind the star from the observer's point of view), $\alpha = 90^\circ$ when the planet is at quadrature (the greatest elongation) and $\alpha = 180^\circ$ at inferior conjunction (planet is in front of the star). The phase function, Equation (1.18), and the flux ratio relation, Equation (1.17), have maximum value for the phase angle $\alpha = 0^\circ$; $\Phi(0) \equiv 1$.

Another very important quantity is the Bond albedo A_B . The Bond albedo is the fraction of incident stellar energy scattered back into space by the planet, into all directions and at all frequencies.

The shape of the light curve describing the reflected and thermal components is shown in Figure 1.16 and marked with letter R.

The equilibrium temperature, T_{eq} , of KOI-13.01 can be calculated assuming the incoming stellar radiation is in balance with the outward radiation from the planet. It is also assumed that the energy received by the day side is efficiently redistributed over the whole surface (i.e. also to the night side). Then,

$$T_{\text{eq}} = \frac{1}{2} \left(\frac{(1 - A_B)L_*}{\sigma \pi a^2} \right)^{1/4} \approx 3400 \text{ K}, \quad (1.19)$$

where A_B is the Bond albedo (which we assumed to be zero), L_* is the luminosity of the star—assumed to be $L_* = 30.5 L_\odot$ (Szabó et al., 2011), σ is the Stefan–Boltzmann constant, and a is the distance of the planet from the star.

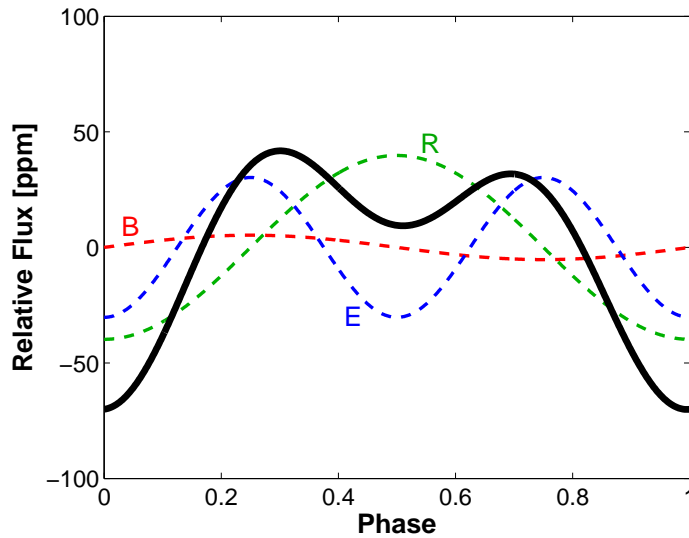


Figure 1.16: Synthetic light curves of KOI-13.01 representing sinusoidal signals of three effects: ellipsoidal variations (E), reflection effect (R), and beaming effect (B), separately. The solid black line is the sum of the three effects. Taken from Shporer et al. (2011).

Doppler boosting

Doppler boosting (consequence of beaming effect) is an effect arising as a consequence of the moving source of the light. The total (bolometric) flux coming from the star as seen by the observer is boosted or deboosted with respect to the direction of the source movement.

This effect was observed from the ground (Maxted et al., 2000), but was predicted to be observable in exoplanetary systems with space missions like Kepler and CoRoT (Loeb & Gaudi, 2003). Consequently, it was observed in the CoRoT-3 system (Mazeh & Faigler, 2010).

Because of the relatively low velocities of the parent stars, the variability amplitude of this effect is the lowest of all of the previously discussed effects. The most significant feature of this effect is that the maxima of the light curve become asymmetric. The variations caused by the beaming effect only are plotted in Figure 1.16. The modelled light curve is marked with letter B.

1.4.2 KOI-13.01

KOI-13.01 is a transiting exoplanetary candidate discovered in 2011 by the Kepler mission (Borucki et al., 2011), together with another 1235 planetary candidates. The abbreviation KOI stands for Kepler Object of Interest. These objects did not pass the

follow-up observations to be accepted as exoplanets though. Consequently they were categorized as planetary candidates instead (Borucki & Kepler Team, 2010).

The host star of KOI-13.01 is a member of the visual double star system BD+46 2629.¹ Both stars KOI-13 A and KOI-13 B are rapidly rotating ($\sim 70 \text{ km s}^{-1}$) A type stars with effective temperatures of 8 500 and 8 200 K, respectively (Szabó et al., 2011). According to the CCDM catalogue (Dommagnet & Nys, 2002), the apparent magnitudes of the stars are $V_A = 9.9 \text{ mag}$ and $V_B = 10.2 \text{ mag}$. The exoplanet candidate KOI-13.01 is orbiting the brighter star KOI-13 A with an orbital period of $\sim 1.76 \text{ days}$ (Mislis & Hodgkin, 2012; Szabó et al., 2011). In the discovery paper (Borucki et al., 2011), the radius of the planet was estimated as $R_p = 20.5 R_\oplus \sim 1.83 R_J$, which made KOI-13.01 one of the biggest known exoplanets. The photometric study of Barnes et al. (2011) determined the orbital inclination $i = 85.9 \pm 0.4^\circ$ and planetary radius to be $R_p = 1.445 \pm 0.016 R_J$. The value of the radius is in disagreement with the previously presented value from the study of Szabó et al. (2011), where the spectroscopically determined radius $R_p = 2.2 R_J$ indicated a much larger object. The independent confirmation of the mass of KOI-13.01 ($M_p = 8.3 \pm 1.25 M_J$) indicated that this object is rather a planet than a brown dwarf (Mislis & Hodgkin, 2012).

The light curve of KOI-13.01 shows primary and secondary transits and out-of-eclipse light curve variations as was reported by Szabó et al. (2011). These out-of-eclipse variations are caused by ellipsoidal modulations (result of the tidal distortion of the star), by the stellar light reflected by the planet, thermal emission from the planet, and by the doppler boosting. All of these effects were studied in more detail by e.g. Shporer et al. (2011) or Mislis & Hodgkin (2012). They fitted the approximate analytical formulae to the observed data and put constraints on the mass of the exoplanet.

1.4.3 Models of light curves

Contrary to the previous papers, we focused on the numerical models of light curve of KOI-13.01. We present our results in the following sections.

SHELLSPEC code

To calculate the synthetic light curves of transiting system KOI-13.01, we used the SHELLSPEC code (Budaj & Richards, 2004, version 25). The SHELLSPEC code, written in Fortran 77, is designed to calculate light curves, spectra and images of interacting binaries and extrasolar planets immersed in a moving circumstellar environment,

¹Recently, Santerne et al. (2012) discovered a third stellar companion KOI-13 γ with a mass of between $0.4 M_\odot$ and $1 M_\odot$. This star probably orbits the brighter star KOI-13 A with orbital period of $65.831 \pm 0.029 \text{ days}$ and eccentricity 0.52 ± 0.02 . This new stellar companion does not affect the photometric mass determination of KOI-13.01.

which is optically thin. The model takes into account reflected light from the planet, absorption and emission of the light from the planet, heat redistribution over the surface, and Roche geometry.¹

An important part of the code is the independent subroutine `Roche`. As the name suggests, this subroutine calculates the Roche shapes of the primary and secondary (star and planet in our case) components in the detached system. To include the Roche shape of the objects into the SHELLSPEC calculations, we determined the fill-in parameter of star, f_* , and planet, f_p , separately. These parameters are defined as:

$$f_* = x_s/L_{1x}, \quad (1.20)$$

$$f_p = (1 - x_s)(1 - L_{1x}), \quad (1.21)$$

where x_s is the x coordinate of the substellar point (point on the surface of the star closest to the planet). L_{1x} is the x coordinate of the L1 point $L1(L_{1x},0,0)$. This parameter characterizes how much the shape of the body departs from a spherical shape. The Roche shape assumes a circular orbit, synchronous rotation, alignment of the rotation and orbital axes of the detached component, and that the gravity of the objects is given by a point mass approximation. The values for the KOI-13.01 system host star and exoplanet were calculated as $f_p = 0.2302$ and $f_* = 0.3638$. The value of the fill-in parameters were consequently used as an input into the SHELLSPEC code.

Reflection effect

To calculate the theoretical light curves of transiting planet KOI-13.01, the modified model of reflection effect was used in the SHELLSPEC code.

The standard reflection effect is a process occurring in close binary systems. One star is irradiated by the other, and part of this energy is converted into heat. This process consequently raises the local temperature and this is reradiated as energy on the day side of the star. The rest of the incoming energy is absorbed and penetrates the star. As the temperature on the day side of the star rises, the secondary reflection effect occurs. The second star is irradiated by the first one. To fully describe these effects, several reflections are usually assumed (see e.g. Wilson, 1990, for a review of the reflection effect in binary stars).

In the case where the second object is a planet (or cool star) the situation is slightly different. The standard model of the reflection effect in interacting binaries neglects the reflection of light from the second object. For cool, strongly irradiated objects, reflected light can be substantial. Another important process that occurs within cold

¹The SHELLSPEC code is available at www.ta3.sk/~budaj/shellspec.html.

objects is the transportation of energy from the day to the night side of the planet. The energy transported to the night side can subsequently be reradiated from there as well. In the following, we take into account three separate processes. These are *reflection* of the light off the companion, *heating* of the irradiated surface by the absorbed light, and *heat redistribution* over the planetary surface.

The model of the reflection effect used in SHELLSPEC includes several free parameters. The first one is *Bond albedo* A_B , introduced in Section 1.4.1. The value of the Bond albedo spans from 0 to 1. In the case when $A_B = 1$, all the incident radiation is reflected into space. The second parameter is the *heat redistribution parameter* $P_r = \langle 0, 1 \rangle$. This parameter indicates how much heat is redistributed from certain point to other places and how much is reradiated locally. If $P_r = 0$, all the absorbed heat is reradiated locally and nothing is transported to other locations. The third parameter is the *zonal temperature redistribution parameter* $P_a = \langle 0, 1 \rangle$. This parameter is a measure of the effectiveness of the homogeneous heat redistribution over the surface versus the zonal distribution. If $P_a = 1$, then the heat is homogeneously redistributed over the surface. $P_a = 0$ means zonal redistribution and that the heat flows only along the parallels.

Other important parameters that enter the calculations are the fill-in parameter $f_i = \langle 0, 1 \rangle$ (discussed above), the mass ratio q of the two objects, the gravity darkening coefficient β , and the quadratic limb darkening coefficients taken from Sing (2010).

1.4.4 Kepler data analysis

For our analysis, we used the publicly available data obtained within the Kepler mission in the quarters Q0–Q9. These data are accessible via the Kepler mission archive.¹ The Kepler mission is designed to search for extrasolar planets, especially Earth-sized ones, via the transiting method. The Kepler instrument consist of a 0.95 m Schmidt telescope fitted with a detector composed of an array of 42 CCDs. This equipment works in a way similar to a photometer. The telescope is pointing into one fixed field in the Cygnus constellation. The wavelength range of the detector is 420–900 nm. Figure 1.17 shows the combined spectral response for all elements of the device.

Data available in the archive were processed by the automatic pipeline performing aperture photometry. For our analysis we used *short cadence* data² of KOI-13.01, which

¹All the data presented in this section were obtained from the Mikulski Archive for Space Telescopes (MAST). STScI is operated by the Association of Universities for Research in Astronomy, Inc., under NASA contract NAS5-26555. Support for MAST for non-HST data is provided by the NASA Office of Space Science via grant NNX09AF08G and by other grants and contracts.

²Kepler archive also offers a second format of observed data, designated *long cadence* data. These are 270 frames coadded for a total of 1766 s bins. We did not use this format of data, because of its absence in some of the quarters.

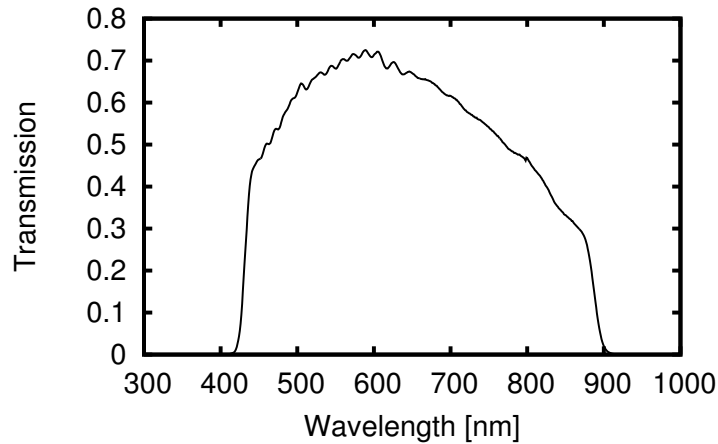


Figure 1.17: Kepler photometer total spectral response. Taken from Kepler Instrument Handbook <http://archive.stsci.edu/kepler/documents.html>.

are one minute sums of nine separate integrations. The length of each integration time is 6.54 s. It consists of the exposure time (6.02 s) and readout time (0.52 s). From these data we determined the orbital period of the planet to be $P_{\text{orb}} = 1.76357(82)$ days using the Fourier method. Subsequently we phase-folded and linearly normalized the data with this period. The phase was set so that the transit occur at the phase of 0.5. During the process, a phase interval of $\langle 0.42, 0.58 \rangle$, which contains the transit, was excluded from the fitting (computing reasons). The light curve obtained within this procedure was then subject to a running window averaging. For a part of the light curve with transit a running window with the width of 0.001 and the step of 0.000 1 in the phase was used. For the out-of-eclipse part of the light curve the width of 0.01 and the step of 0.001 was used. Consequently the average value within each window position was calculated. The resulting phase-folded and normalized light curve together with the smoothed light curve is plotted in Figure 1.18. Figure 1.19 shows the detail of the occultation and out-of-eclipse variation. The light curve was normalized with respect to the bottom part of occultation. This normalized light curve was binned (the size of the bin was 0.001) and the resulting data set was used in our consequent analysis in Figures 1.20–1.27.

Since the parent star is a component of the binary system, separated by $1.18 \pm 0.03''$ (Szabó et al., 2011), which is less than the pixel size ($4''/\text{pix}$) of the Kepler CCDs, we corrected the light curve for the flux from the second companion KOI-13B. The brightness difference of both components in the Kepler magnitude is $\Delta V = 0.2 \pm 0.04$ mag, with KOI-13A containing 55% of the light. So the resulting light curve was obtained by multiplying the excess flux by ~ 1.818 (Szabó et al., 2011). By excess flux is meant the part of the normalized light curve with the absence of the transit.

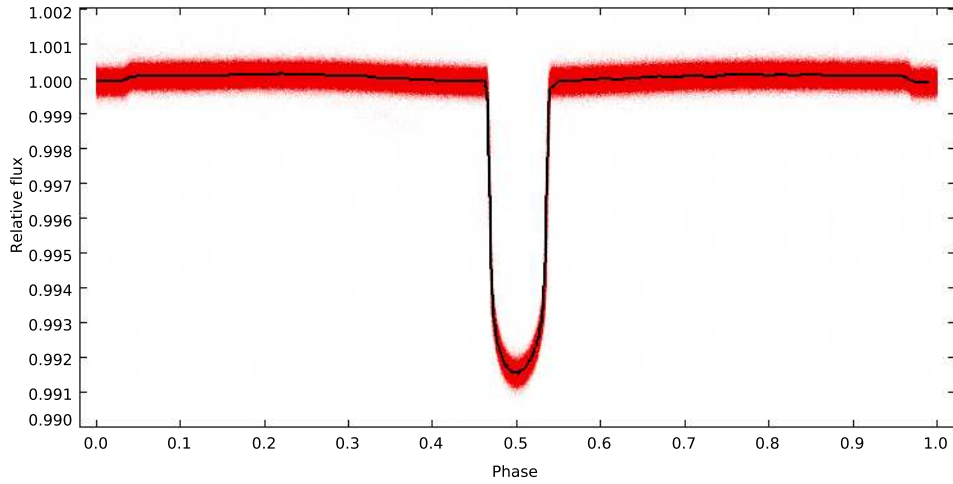


Figure 1.18: Phase-folded light curve of KOI-13.01. Transit (phase 0.5) and occultation (phase 0) are clearly seen. Light curve consists of more than one million individual exposures. The solid line indicates the smoothed light curve.

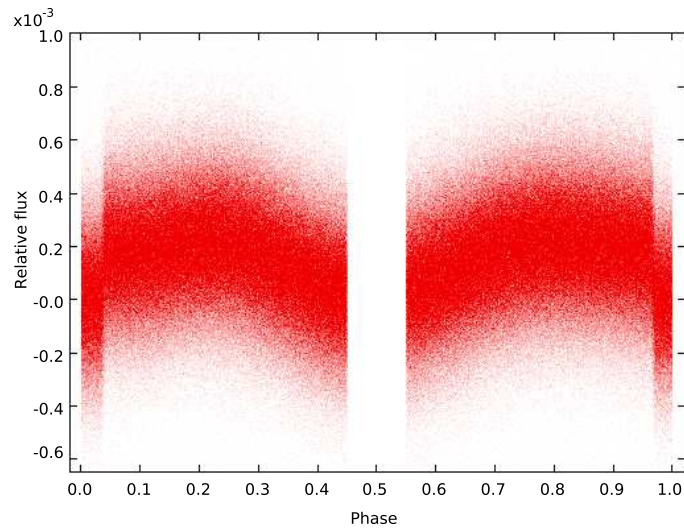


Figure 1.19: Phase-folded light curve of KOI-13.01. Detail of out-of-eclipse variations and secondary eclipse. Light curve consists of more than one million individual exposures.

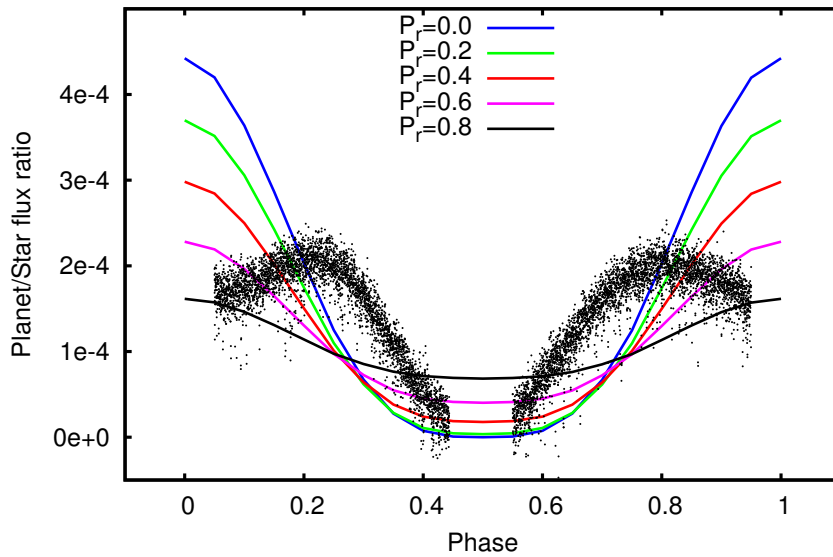


Figure 1.20: Theoretical phase-folded light curves (colour lines) and Kepler data (black points). Kepler light curve consist of more than 8×10^5 individual exposures. The primary (phase 0.5) and secondary (phase 0) transit data are omitted. Theoretical light curves were calculated assuming black body approximation for Bond albedo $A_B = 0$ and homogeneous zonal temperature redistribution parameter $P_a = 1$.

1.4.5 Results

In order to study the out-of-eclipse part of the light curve of the exoplanetary system KOI-13.01, several theoretical light curves were calculated and compared with the real data. All the light curves presented in this section were calculated for $\lambda = 600$ nm, which is close to the maximum spectral response of Kepler photometer at 575 nm. Two models of energy distribution on the planet and star were used – the black and non-black body models. The free parameters A_B , P_r and P_a were varied in all the models and their impact on the light curve shape was studied.

Black body approximation

The most straightforward way to model the energy distribution on the planet and the star, was the usage of black body approximation.

For every two fixed values of the Bond albedo $A_B = 0$ and $A_B = 0.5$ and one value of temperature redistribution parameter $P_a = 1$, we calculated five light curves with different heat redistribution parameter $P_r = 0.0, 0.2, 0.4, 0.6$, and 0.8 . The results are in Figures 1.20 and 1.21. In both figures, the real Kepler data of KOI-13.01 are also plotted.

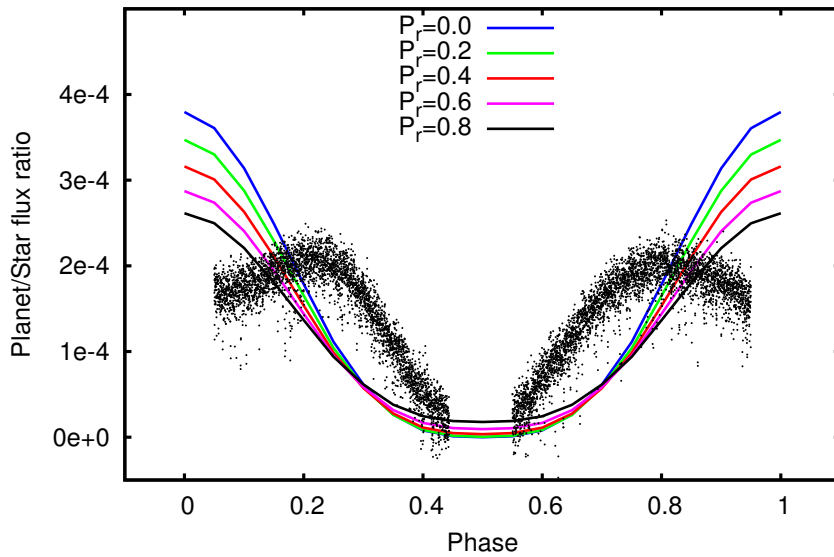


Figure 1.21: Theoretical phase-folded light curves (colour lines) and Kepler data (black points). Kepler light curve consist of more than 8×10^5 individual exposures. The primary (phase 0.5) and secondary (phase 0) transit data are omitted. Light curves were calculated assuming black body approximation for Bond albedo $A_B = 0.5$ and homogeneous zonal temperature redistribution parameter $P_a = 1$.

Non-black body approximation

To apply a more realistic approach, the non-black body model of the energy distribution of the planet and the star was used. Models for the star were taken from Atlas9 stellar atmosphere models from Kurucz and Castelli (Castelli & Kurucz, 2004).¹ The assumed parameters of the star for the model were $T_{\text{eff}} = 8750$ K, $\log g = 4.0$ (cgs) $[M/H] = 0.0$, and $v_{\text{turb}} = 2.0 \text{ km s}^{-1}$. Models calculated by program coolTlusty were used for the planets for $T < 1800$ K (Hubeny & Burrows, 2007). For $1800 < T < 3500$ K models from the Phoenix program were used (Allard et al., 2003). In the case of KOI-13.01, the temperature of the sub-stellar point can reach 5 000 K. On that account we applied also models for the temperature range of 3500–5500 K from Castelli & Kurucz (2004).

Figures 1.22–1.27 show the light curves calculated for different combinations of free parameters. Figures 1.22, 1.23, and 1.24 show five light curves each, where the value of the Bond albedo was fixed at $A_B = 0.0, 0.3, \text{ and } 0.5$, respectively. For each of the albedo values light curves were calculated while varying the value of $P_r = 0.0, 0.2, 0.4, 0.6, \text{ and } 0.8$. The value of P_a was fixed to one.

Figures 1.25, 1.26, and 1.27 show the models calculated for various fixed values of the albedo A_B and heat redistribution parameter P_r . Each figure shows six light curves

¹<http://wwwuser.oat.ts.astro.it/castelli/grids/gridp00k2odfnew/fp00k2tab.html>

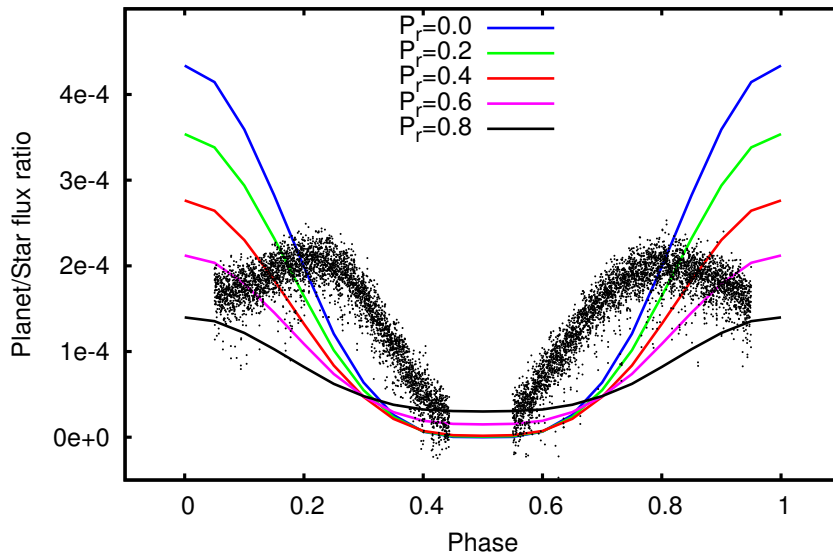


Figure 1.22: Theoretical phase-folded light curves (colour lines) and Kepler data (black points). Kepler light curve consist of more than 8×10^5 individual exposures. The primary (phase 0.5) and secondary (phase 0) transit data are omitted. Light curves assuming non-black body approximation were calculated for Bond albedo $A_B = 0$ and homogeneous zonal temperature redistribution parameter $P_a = 1$. Each light curve stands for different heat redistribution parameter P_r .

for different values of the zonal temperature parameter $P_a = 0.0, 0.2, 0.4, 0.6, 0.8,$ and 1.0 .

1.4.6 Discussion and conclusion

In this Section the variations of the out-of-eclipse part of the light curve of transiting exoplanet KOI-13.01 were studied. KOI-13.01 is, with its proximity to the host star of spectral type A and consequent high temperature, one of the best candidates for studying the out-of-eclipse light curve variations.

We modelled the synthetic light curves with the SHELLSPEC code, assuming reflection of the light coming from the host star, heating of the irradiated planetary surface and consequent heat redistribution over the planetary surface. The modelled light curves were compared with real data of exoplanetary system KOI-13.01 obtained within the Kepler mission.

For modelling of the energy distribution of the planet and star, black body (Figures 1.20 and 1.21) and non-black body models were used (Figures 1.22–1.27). We studied the effect of Bond albedo, heat redistribution over the planetary surface and the effectivity of the heat redistribution on the shape of the light curve. In our analysis,

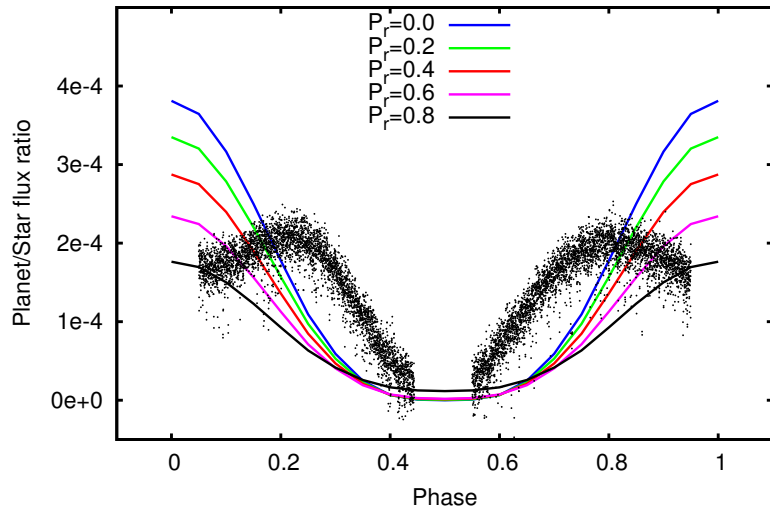


Figure 1.23: Theoretical phase-folded light curves (colour lines) and Kepler data (black points). Kepler light curve consist of more than 8×10^5 individual exposures. The primary (phase 0.5) and secondary (phase 0) transit data are omitted. Light curves assuming non-black body approximation were calculated for Bond albedo $A_B = 0.3$ and homogeneous zonal temperature redistribution parameter. Each light curve stands for different heat redistribution parameter P_r .

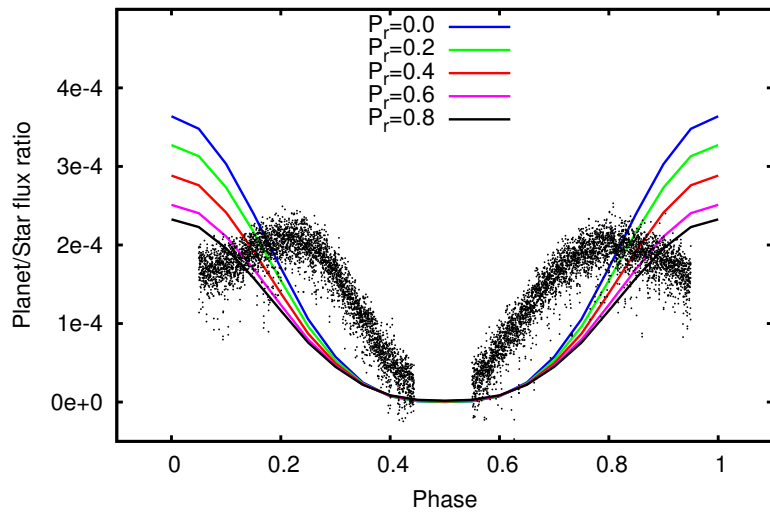


Figure 1.24: Theoretical phase-folded light curves (colour lines) and Kepler data (black points). Kepler light curve consist of more than 8×10^5 individual exposures. The primary (phase 0.5) and secondary (phase 0) transit data are omitted. Light curves assuming non-black body approximation for Bond albedo $A_B = 0.5$ and homogeneous zonal temperature redistribution parameter. Each light curve stands for different heat redistribution parameter P_r .

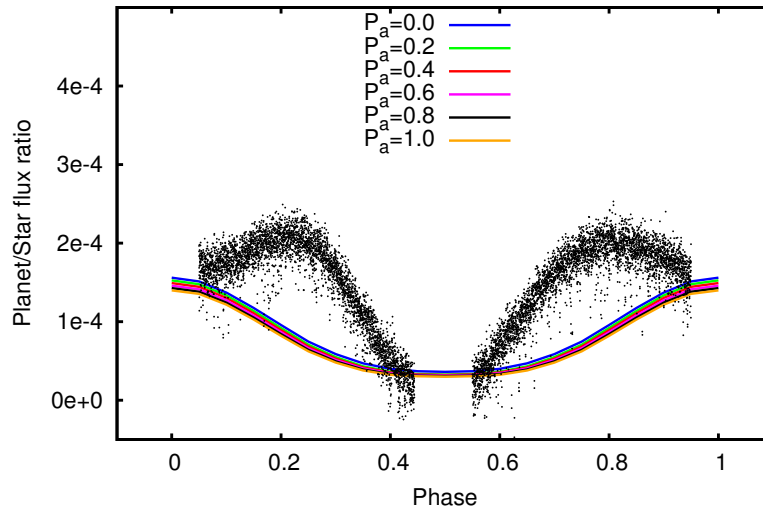


Figure 1.25: Theoretical phase-folded light curves (colour lines) and Kepler data (black points). Kepler light curve consist of more than 8×10^5 individual exposures. The primary (phase 0.5) and secondary (phase 0) transit data are omitted. Light curves assuming non-black body approximation for Bond albedo $A_B = 0.0$ and heat redistribution parameter $P_T = 0.8$. Each light curve stands for different value of degree of the inhomogeneity of the heat transport P_a .

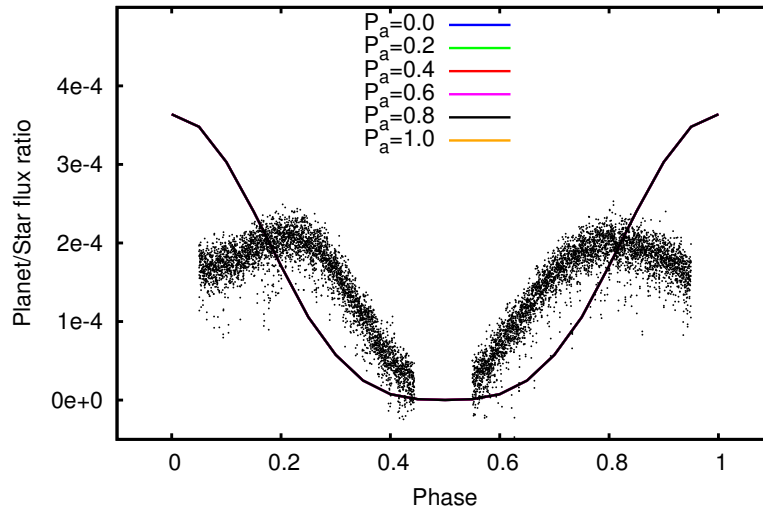


Figure 1.26: Theoretical phase-folded light curves (colour lines) and Kepler data (black points). Kepler light curve consist of more than 8×10^5 individual exposures. The primary (phase 0.5) and secondary (phase 0) transit data are omitted. Light curves assuming non-black body approximation for Bond albedo $A_B = 0.5$ and heat redistribution parameter $P_T = 0.0$. Each light curve stands for different value of degree of the inhomogeneity of the heat transport P_a .

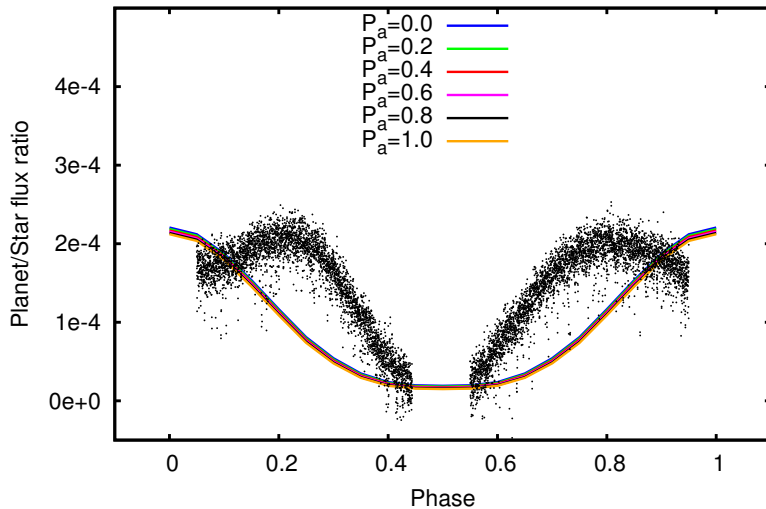


Figure 1.27: Theoretical phase-folded light curves (colour lines) and Kepler data (black points). Kepler light curve consist of more than 8×10^5 individual exposures. The primary (phase 0.5) and secondary (phase 0) transit data are omitted. Light curves assuming non-black body approximation for Bond albedo $A_B = 0.0$ and heat redistribution parameter $P_r = 0.6$. Each light curve stands for different value of degree of the inhomogeneity of the heat transport P_a .

we concentrated on the modelling of the reflected and thermal component, which are the most pronounced effects in the light curve (we did not take into account ellipsoidal variations and boosting effect). Consequently, our interpretation of results is based on the areas of the light curve in the vicinity of transit and occultation (phases 0.5 and 0). The effects of ellipsoidal variations and boosting are most pronounced at the phases 0.25 and 0.75.

The plots 1.20–1.27 indicate that the light curve (composed of Kepler data points) better correspond to the models with rather low values of the Bond albedo A_B and higher values of the heat redistribution parameter P_r . We estimated the value of Bond albedo to be $A_B < 0.3$ and the value of the heat redistribution parameter to be $P_r > 0.6$. The zonal temperature redistribution parameter P_a does not seem to influence the shape of the light curve significantly (Figures 1.25–1.27). This analysis shows that the atmosphere of extrasolar planet KOI-13.01 should be non-reflective and dark, and that the process of heat transfer is rather significant for this planet.

Our results correspond with the previously published studies about exoplanetary albedos. Cowan & Agol (2011) statistically studied albedos of 24 transiting exoplanets and concluded that all these exoplanets are consistent with the low value of Bond albedo. Mazeh et al. (2012) derived the Bond albedo and geometrical albedo of KOI-13.01 as a function of the day-side planetary temperature. The value of the Bond

albedo is supposed to be rather low (< 0.4) for a day-side temperature higher than 3400 K.

Results described in this section were presented in the form of a poster at the Sagan Exoplanet Summer Workshop held in Pasadena in the USA in 2012.

CHAPTER 2

STAR–PLANET INTERACTION

2.1 Introduction

Planetary and stellar system bodies (stars, planets, their satellites) are not isolated objects. They could influence or interact with one another in many possible ways. The way of the interaction is usually quite complex. We know many such examples from our own solar system. One that is worth mentioning is the Jupiter–Io system (de Pater & Lissauer, 2001). As a result of Io’s close proximity to Jupiter, it is constantly heated by tidal forces from Jupiter, which leads to melting of Io’s interior. Another effect is the interaction of Io with Jupiter’s magnetosphere. The rotation period of Jupiter is less than 10 hours and the orbital period of Io is 1.77 days. As Io moves through the magnetosphere, which tend to corotate with Jupiter, an electric potential difference between Io and Jupiter arises. The potential difference causes a current of nearly 10^6 A to flow along the magnetic field lines between Jupiter and Io. On the other hand, most of the charged particles trapped in Jupiter’s magnetic field came from Io.

One of the major groups of extrasolar planets discovered so far is (as mentioned in Introduction) Hot Jupiters. These Jupiter-sized planets orbit their parent stars at very close distance. Consequently a vast number of interesting effects could occur between them. Evaporation of the planet (Vidal-Madjar et al., 2003; Hubbard et al., 2007); precession of the periastron due to general relativity (Jordán & Bakos, 2008), strong irradiation of the planet and its effect on the planetary radius (Guillot & Showman, 2002; Burrows et al., 2007) or atmospheric and stratospheric processes (Hubeny et al., 2003; Burrows et al., 2008; Fortney et al., 2008) are only a few examples from the long list.

One of the most interesting effects which are expected to occur between the star and exoplanet are the tidal and magnetic interaction. Cuntz et al. (2000) made a first attempt to estimate the magnitude of such a possible tidal and magnetic interactions. They calculated the relative strength of the star–planet interactions for 12 selected exoplanetary systems with the distance of $d \lesssim 0.1$ AU. Most of the host stars in the sample

were solar-type stars, which were supposed to have chromospheres, transition regions and coronae. In case the planet somehow influences the star, it would affect mainly the upper layers of the stellar atmosphere, because of its low density and proximity to the planet.

The tides raised on the star affect the convective zone, as well as the outer layers of the star. In the case the $P_{\text{rot}} \neq P_{\text{orb}}$ (systems are not rotationally synchronized) the tidal bulge rises and drops down to cause the expansion and contraction of the outer layers. This process causes the flows and waves, which result in a significantly higher production of nonradiative energy. This will lead to enhanced heating and a higher level of stellar activity. Magnetic interaction is supposed to occur between stellar active regions and the extrasolar planet magnetosphere. The magnetosphere of Hot Jupiters is expected to strongly resemble that of the Jovian one in the work of Cuntz et al. (2000). They found, that the strength of tidal and magnetic interaction depends among others on the separation of the objects, size of the planet and magnetic field strength of the star and planet.

This problem is similar to processes occurring in the RS Canum Venaticorum (hereafter RS CVn) systems (Hall, 1976). RS CVn are chromospherically active detached binaries with periods of approximately 0.5 to 14 days (for some types the period can reach 140 days). These systems consist of a slightly evolved stars of spectral type F, G or early K and of luminosity class II–V. They are active as a result of the relatively rapid rotation of at least one component. The majority of the RS CVn binaries have the rotation of their active components synchronized with their orbital motion (Schrijver & Zwaan, 2000). The enhanced activity caused by this interaction is manifested by starspots, chromospheric and coronal activity, and flares. As a consequence of the presence of unevenly distributed starspots (these could cover a significant part of the stellar surface) across the surface, the system shows photometric variability. In RS CVn systems, the observed levels of chromospheric and coronal activity are higher than for single stars of the same spectral class.

Rubenstein & Schaefer (2000) suggested that the superflares observed on nine F–G main-sequence stars, which is an effect very similar to the one detected in RS CVn systems, can be caused by the close proximity of an exoplanet and its consequent interaction.

This chapter is focused on the search for star–planet interaction in exoplanetary systems. Our goal of this work was to investigate the possible correlation between the stellar activity and the orbital and physical parameters of the orbiting exoplanet.

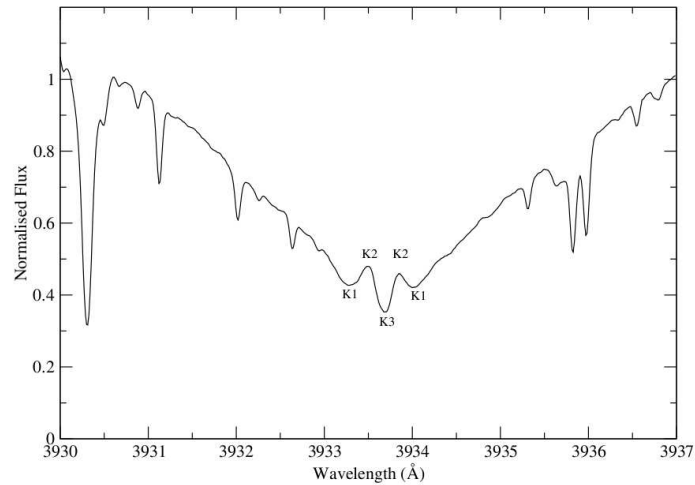


Figure 2.1: The core of the Ca II K line in the spectrum of the Sun. Taken from Shkolnik (2004).

2.1.1 Ca II H and K lines

The most suitable regions of the spectra for observing chromospheric and coronal activity are UV, EUV and X-rays. These were observed from space by, e.g. the IUE, ROSAT, and XMM-Newton missions. However, the chromospheric activity can be also observed in the optical region from the ground in the cores of several spectral lines: the H and K lines of singly ionized calcium (3933, 3968 Å), the D lines of neutral sodium (5889, 5895 Å), He I D₃ (5876 Å) and H α (6563 Å). Of these, Ca II H and K lines were of special interest. These lines are very strong and their core is formed in the chromosphere of the star, hence were used for surveys of stellar chromospheric activity, see Hall (2008) and references therein.

Figure 2.1 shows the structure of the Ca II K line of the Sun. K1 point marks the turn over part of the absorption feature when it changes into the emission. It is formed at the top of the photosphere. The feature denoted as K2 is a double-peaked emission that is formed in the chromosphere at temperature of about 8 000 K. The self-reversal core (due to the large optical depth of the line) is marked as K3 and is produced at the top of the chromosphere where the temperature reaches 20 000 K. Figure 2.2 shows the atmospheric model of the Sun and the depths where different spectral lines are formed, the origin of Ca II H and K lines included.

The presence of the emission components in the cores of the Ca II H and K resonance lines in the spectra of many stars of spectral type G and later has been a known fact for a long time. Eberhard & Schwarzschild (1913) found out that the stellar K and H

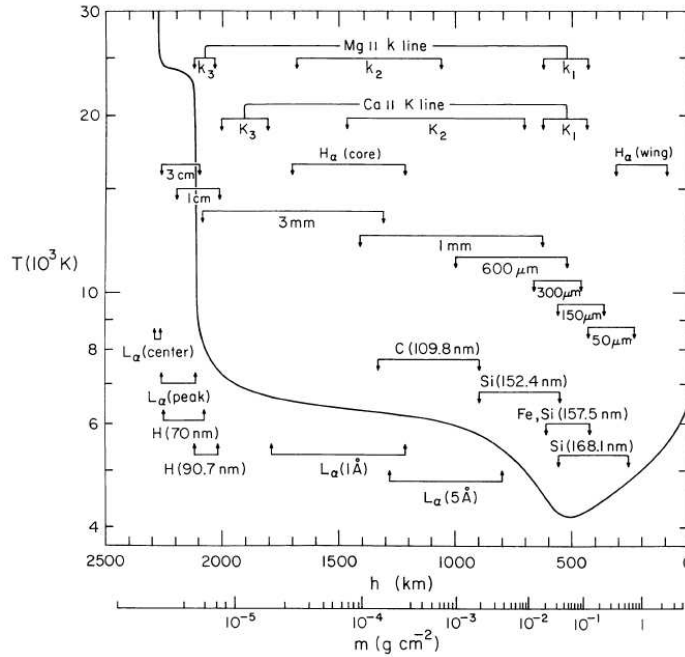


Figure 2.2: The average quiet-Sun temperature distribution. The approximate depths where the various continua and lines originate are indicated. The plot is adopted from Vernazza et al. (1981).

lines of calcium show a sharp reversal, with the calcium emission in the middle of the absorption line just as it is observed in the Sun.

2.1.2 Mt. Wilson observations

The Ca II H and K lines were chosen by O.C. Wilson for a long-term, ground-based survey of stellar activity in order to reveal the analog of the Sun's 11 year activity cycle in other stars (Wilson, 1968, 1978). This systematic research, which took place on Mount Wilson Observatory began in 1966 and continued for more than 40 years. The original instrument used for the observations was the photoelectric coude scanner at the 100 inch telescope. In 1977 it was replaced by a four channel (*R, V, H, K*) spectrophotometer (Vaughan et al., 1978) The photoelectric coude scanner was then removed from the 100 inch telescope and moved to the 60 inch telescope.

Amongst the most important results of this survey, summarized in Duncan et al. (1991) and Baliunas et al. (1995), was the discovery of activity cycles in solar-type stars, similar to those of the Sun. In addition a number of stars showed evidence of uncompleted cycles of duration greater than 11 years, and many showed real variability at time scales from one day to several months.

The survey contributed towards an understanding of the evolution of stellar activity and stellar rotation. With the Mt. Wilson project it was proved that chromospheric activity of main-sequence stars decreases with age and that their rotational periods can be determined from the rotational modulation of Ca II H and K emission (Vaughan et al., 1981).

For a quantitative description of the Ca II H and K line flux, an instrumental S index was introduced (Middelkoop, 1982):

$$S \equiv \alpha \frac{N_H + N_K}{N_R + N_V}, \quad (2.1)$$

where $\alpha = 2.4$ is the constant of proportionality, N_H , N_K , N_R , and N_V are the number of counts in the corresponding channels. R (3991.07–4011.07 Å) and V (3891.07–3911.07 Å) channels are 20 Å-wide continuum bands. Triangular shaped channels H and K are centered on the cores of the Ca II H and K lines.

S index has a disadvantage that it cannot be used to compare stars of different spectral types. It includes both the chromospheric emission and the flux from the photosphere. As the continuum flux decreases through the spectral type sequence, the S index tends to increase. A new parameter $-\log R'_{\text{HK}}$ was introduced in order to remove the photospheric component from the S index and to determine the fraction of a star's luminosity that is in the Ca II H and K lines (Middelkoop, 1982; Noyes et al., 1984; Wright et al., 2004). The R'_{HK} parameter is calculated as:

$$R'_{\text{HK}} = R_{\text{HK}} - R_{\text{phot}}, \quad (2.2)$$

where

$$R_{\text{HK}} = 1.340 \times 10^{-4} C_{\text{ef}} S. \quad (2.3)$$

The colour-dependent conversion factor $C_{\text{ef}}(B - V)$ is:

$$\log C_{\text{ef}}(B - V) = 1.13(B - V)^3 - 3.91(B - V)^2 + 2.84(B - V) - 0.47, \quad (2.4)$$

where the R_{phot} is a photospheric component. This relation was derived only for main-sequence stars with $0.45 \leq (B - V) \leq 1.50$. The R_{phot} parameter is then calculated as:

$$\log R_{\text{phot}} = -4.898 + 1.918(B - V)^2 - 2.893(B - V)^3. \quad (2.5)$$

The resulting parameter $\log R'_{\text{HK}}$ increases with higher activity.

2.2 Search for star–planet interaction

As stated in previous sections, the idea of possible influence of the stars by orbiting objects (planets, stars) is not new. In the last decade, the extensive searches for star–planet interaction in the whole energy spectrum from the ground as well as from space

were carried out. In this section I give only brief review about this phenomenon, mentioning the most important results.

Shkolnik et al. (2003, 2005, 2008) presented a set of papers concerning the search for modulation (variation) of selected lines in the spectra of stars with close-in exoplanets in phase with the planetary orbit. They observed selected stars with exoplanets with the 3.6 m Canada-France-Hawaii Telescope in the optical region. Their observing runs span over several years and they monitor the activity preferentially in the cores of Ca II H and K lines. As a result they found an evidence for variations in Ca II emission connected with the orbital period of close-in exoplanet.

Knutson et al. (2010) studied the correlation between the activity of the host star and the type of the atmosphere of exoplanet. For a sample of 50 transiting exoplanets they measured the strength of the Ca II H and K lines and consequently determined the $\log R'_{\text{HK}}$ parameter (defined by Equation 2.2). They found that planets orbiting chromospherically active stars have so-called “non-inverted” atmospheres (HD 189733, Tres-1, Tres-3, and Wasp-4), while atmospheres of planets orbiting quiet stars show a strong high-altitude temperature inversion (e.g. HD 209458, Tres-2, Tres-4, Hat-p-7, and Wasp-1). This finding was explained as that the more active stars emit more in the UV region and this radiation destroys the high-altitude absorber responsible for the formation of temperature inversions.

Based on the data from Knutson et al. (2010), Hartman (2010) searched for a correlation between stellar activity (described by the $\log R'_{\text{HK}}$ parameter) and 12 different exoplanetary parameters. They found a correlation between the planet surface gravity $\log g_p$ and the $\log R'_{\text{HK}}$ parameter with greater than 99.5% confidence. However the nature of this correlation was not sufficiently clarified.

Gonzalez (2011) claims that stars with exoplanets have lower values of parameters $v \sin i$ and $\log R'_{\text{HK}}$ (i.e. less activity) than stars without exoplanets.

Kashyap et al. (2008) searched for X-ray activity in more than 200 planet-hosting stars. They found a statistically significant evidence that stars with close-in planets are more active than the stars with exoplanets located further out.

The complex study of star–planet interaction in the X-ray region was made by Poppenhaeger et al. (2010). They studied the stellar X-ray activity of all known exoplanet host stars within a distance of 30 pc. Their sample consisted of 72 exoplanetary systems and they used the quantity L_x/L_{bol} as an activity indicator. L_x is the X-ray luminosity of the star and L_{bol} is its bolometric luminosity. They did not find any correlation between the coronal activity of the star and the planetary parameters semi-major axis a , mass of the planet M_p , and M_p/a . The dependencies observed in the sample were dismissed by the authors as statistical fluctuations or selection effects.

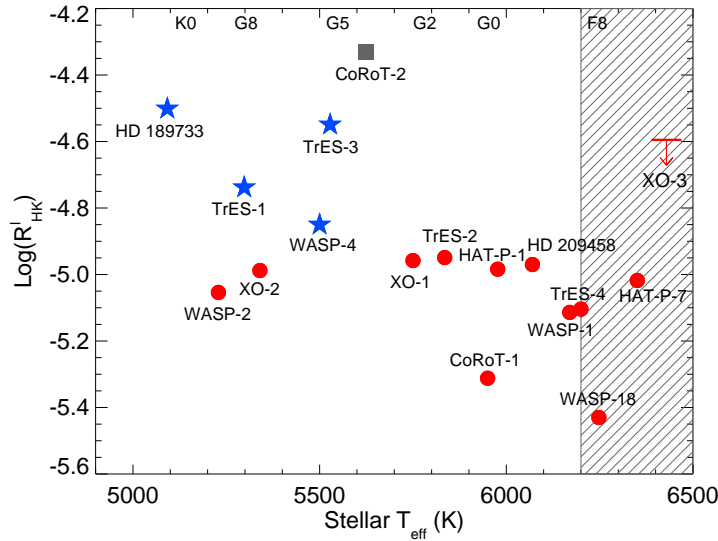


Figure 2.3: Dependence of the $\log R'_{\text{HK}}$ parameter on stellar effective temperature. Exoplanets with temperature inversion orbiting less active stars are marked with circles. The star symbols are for exoplanets without temperature inversion. The grey area on the right side of the plot marks the region for which the $\log R'_{\text{HK}}$ parameter is not defined. Taken from Knutson et al. (2010).

Scharf (2010) studied the X-ray emission of stars hosting planets. He found a positive correlation between the X-ray luminosity of the parent stars and the $M_p \sin i$ parameter of most close-in exoplanets with periastron distance $d_{\text{peri}} < 0.15$ AU.

This interesting discovery motivated Poppenhaeger & Schmitt (2011) to re-analyse the data from Scharf (2010). They focused on possible selection effects which could occur in the selected sample. To make the sample of data robust enough, they included data from previous studies (Poppenhaeger et al., 2010) as well. They found that the dependence presented in Scharf (2010) is a consequence of selection effects caused by the flux limit of the data sample used in Scharf (2010) and also by planet detectability by the RV method.

Canto Martins et al. (2011) analysed a sample composed of stars with and without extrasolar planets. They searched for a dependence of the chromospheric and the X-ray emission flux on the planetary parameters $\log(1/a_p)$ and $\log(M_p/a_p)$ (where a_p is a semi-major axis and M_p is a planetary mass). As a chromospheric and coronal activity indicator they used parameters $\log R'_{\text{HK}}$ and $(\log L_x/L_{\text{bol}})$, respectively. Their sample consisted of 74 stars with exoplanets (detected by radial velocity method) and of 26 stars without extrasolar planets. Their statistical analysis did not reveal any convincing proof for the correlation between the chromospheric activity and the aforementioned planetary parameters.

Alves et al. (2010) investigated the projected rotational velocity, $v \sin i$, and stellar angular momentum of 147 stars with extrasolar planets and 85 stars with no companions. Exoplanetary systems covered in the sample were detected by the RV technique only. The most interesting result of their work was that the angular momentum of stars without exoplanets shows a clear deficit when compared to stars with planets. This effect is most pronounced for stars with mass higher than $1.25 M_{\odot}$.

2.3 Spectroscopic observations and data

In this Section the observing strategies and reduction process of data used for the subsequent statistical analysis are described.

Stellar spectra used in our study originate from two different sources. The main source is the publicly available Keck HIRES spectrograph archive and the sample consists of 206 stars with exoplanets. These data were enhanced by our own observations of four stars (HD 179949, HD 212301, HD 149143 and Wasp-18) with a close-in exoplanet. We obtained these data with the FEROS spectrograph mounted on the 2.2 m ESO/MPG telescope in Chile. In all of the following plots, the data from 2.2 m telescope are marked as red squares.

The sample of data contains 210 exoplanet hosting stars with an effective temperature range of approximately 4 500 to 6 600 K. The semi-major axes of the exoplanets lie in the interval 0.016–5.15 AU.

2.3.1 2.2 m MPG/ESO telescope – Observations and data reduction

FEROS is a fibre-fed échelle spectrograph with a resolution of up to 48 000 and with a spectral coverage from 350 to 920 nm. It is mounted at the Cassegrain focus of the 2.2 m MPG/ESO telescope at La Silla observatory in Chile. A thorium-argon-neon lamp is used for wavelength calibration.

For the purpose of studying star–planet interaction, we observed four exoplanetary systems HD 179949, HD 212301, HD 149143, and Wasp-18 with the FEROS instrument. We selected these systems from the list of discovered exoplanets according to the expected amplitude of variability parameter $M_p \sin i / P_{\text{orb}}$ multiplied by an expected S/N. We ruled out the exoplanets with orbital periods larger than was the duration of the observing run. The spectra of the objects together with the calibration frames (bias, flat, and calibration frames) were taken during five and half consecutive nights. For the consequent statistical analysis described in Section 2.4 only data from the night with the best observing conditions (18/19.9.2010) were used.

Reduction process

The echelle spectra were reduced following the standard procedures. Packages suitable for echelle spectra implemented in IRAF¹ were used.

For the combination of biases the package `ccdred`, task `zerocombine` was used and an average frame was created. *Minmax* rejection was used, whereby a fraction of the highest and lowest pixels were rejected to omit over exposed pixels. After that the bias was subtracted from flats, comps and objects using package `imutil`, task `imarith`. This task is performing basic operations with frames, like addition, subtraction, multiplication, etc. The corrected flats were combined into one master flat with package `ccdred`, task `flatcombine`. In the next step we removed the large scale variability seen in the master flat using the task `apflatten` in the package `echelle`, leaving only pixel-to-pixel variation. This task finds the individual orders, fits the selected function to the intensity along the dispersion and normalizes the flat field with the fit. To avoid a possible zero signal between the orders (numerical reasons), this task replaces the points with a low signal with the integer stated for the *threshold* parameter.

Object frames were divided by the resulting master flat using the package `imutil`, task `imarith`. After that a mask for bad pixels was created using package `proto`, task `fixpix`. Bad pixels were found manually in one flatfield frame and the resulting mask was applied to all the object frames.

The next step was the extraction of the apertures from the 2-dimensional spectra. This was done by the summation of pixels across the dispersion axis. Package `echelle`, task `apsum` was used. This task was also applied to the wavelength calibration frames. The extracted spectra need to be calibrated for the wavelength. For this the calibration frames of the ThArNe lamps were taken. These are spectra with precisely defined and calibrated emission features. By comparing them to the spectra of an object, it is possible to assign accurate wavelength values to the spectra of the object. As a first step, the identification of the spectral lines in the calibration frame must be done. For this, the package `echelle`, task `ecidentify` was used, where the database of emission spectral lines for the employed lamp was used. After that, the spectra with identified lines are applied to the object frames and the spectra are wavelength calibrated.

The continuum of the spectra of the object need to be normalized, for which the package `echelle`, task `continuum` was used. This task fits the continuum with a spline function of specified order and then the spectrum is divided by it.

One of the last steps is the combination of individual spectra of each object into a single spectrum. This was done by the package `onedspec`, task `scombine`. Finally

¹<http://iraf.noao.edu/>

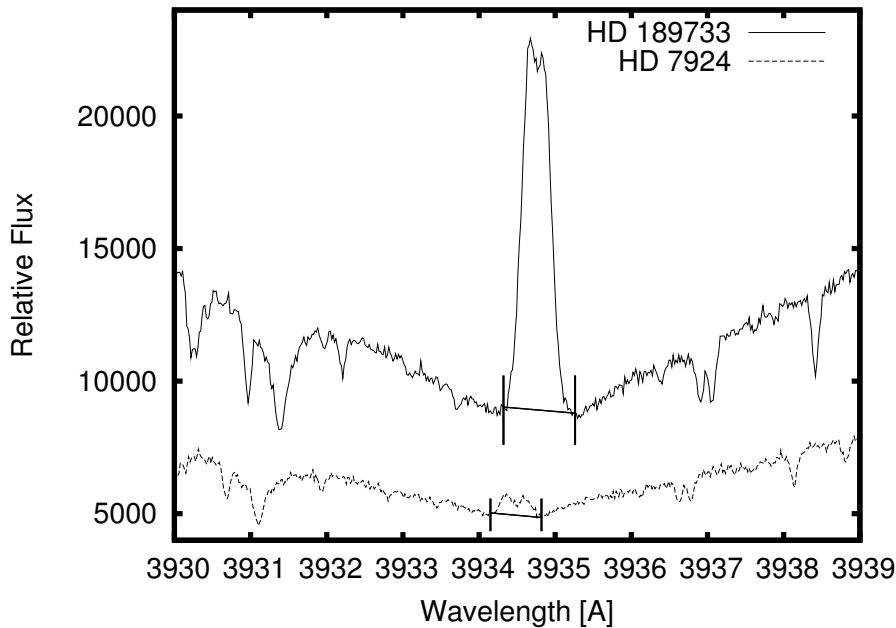


Figure 2.4: Illustration of the core of the Ca II K line in two different stars. We measured only the equivalent width of the core of the line with the central reversal. By definition, equivalent width is negative for emission and positive for absorption.

heliocentric correction was calculated (package `rv`, task `rvcorrect`) and applied to the spectra (package `echelle`, task `dopcor`).

2.3.2 Keck HIRES archive data

The main part of the data used in the statistical study comes from the HIRES instrument mounted on the Keck I telescope.¹ HIRES stands for High Resolution Echelle Spectrometer with a resolution of up to 85 000. The instrument is mounted at the Nasmyth focus and its range spans from 0.3 to 1.1 μm (Vogt et al., 1994).

For our analysis, we used data from the archive of the HIRES instrument.² From the archive we carefully selected only those spectra with a signal-to-noise ratio high enough to measure the precise equivalent width (hereafter EQW) of the Ca II K emission. The data in the archive were reduced by an automated reduction pipeline based upon the HIRES data reduction package MAKEE.³

¹This research has made use of the Keck Observatory Archive (KOA), which is operated by the W.M. Keck Observatory and the NASA Exoplanet Science Institute (NExSci), under contract with the National Aeronautics and Space Administration.

²<http://www2.keck.hawaii.edu/koa/public/koa.php>

³<http://www.astro.caltech.edu/~tb/makee/index.html>

2.3.3 Equivalent width measurements

For each spectrum in the sample, we measured the EQW (in Å) of the central reversal in the core of lines Ca II K and Ca II H. The IRAF software was used for this purpose, namely the package `onedspec`, task `splot`. Figure 2.4 illustrates a placement of the pseudo-continuum in our measurements. The advantage of using such a simple EQW measurement is that this is defined on a short spectral interval that is about one Å wide. Consequently, it is not sensitive to the various calibrations (continuum rectification, blaze function removal) inherent in echelle spectroscopy. For comparison, the $\log R'_{\text{HK}}$ index relies on the information from four spectral channels covering about a 100 Å wide interval. If extracted from echelle spectra, it is much more sensitive to a proper flux calibration and subject to added uncertainties.

Originally, we measured the EQW of the cores of both Ca II K and Ca II H lines. For the analysis, we decided to use the EQW of Ca II K only, because the Ca II H line is strongly blended by the H ϵ Balmer line. Nevertheless, as a check, we plotted two dependencies: T_{eff} vs. $\text{EQW}_{\text{Ca II H}}$ in Figure 2.12 and semi-major axis vs. $\text{EQW}_{\text{Ca II H}}$ in Figure 2.13.

For comparison with our EQW values, we also used the parameter $\log R'_{\text{HK}}$ defined in Equation (2.2). Values of this parameter were taken from the works of Wright et al. (2004), Knutson et al. (2010), and Isaacson & Fischer (2010).

The list of all the exoplanets, their properties, and measured equivalent width together with the $\log R'_{\text{HK}}$ parameter used in this study, are in Appendix D.

2.4 Statistical analysis of the data sample

Most of the previous studies focused on either the monitoring of stellar activity of an individual star connected with the orbital period of an exoplanet, or on comparing two samples of stars, mostly with and without exoplanets. The main goal of this section was to search for a possible correlation between exoplanetary orbital and physical parameters and stellar activity in the sample of stars with exoplanets.

In Figure 2.5 (top part) the EQW of Ca II K emission core versus the effective temperature T_{eff} of the star is depicted. By definition, the EQW is negative for emission. Consequently, lower values mean higher emission and higher chromospheric activity. The dependence of EQW on temperature is immediately apparent, mostly in the lower temperature region. The EQW decreases in this region, which means that the core emission increases towards lower temperatures. This feature is not surprising and is partially a result of the fact, that the photospheric flux in the core of the Ca II K line is lower for cooler stars than for hotter stars. At the same time, the data points that

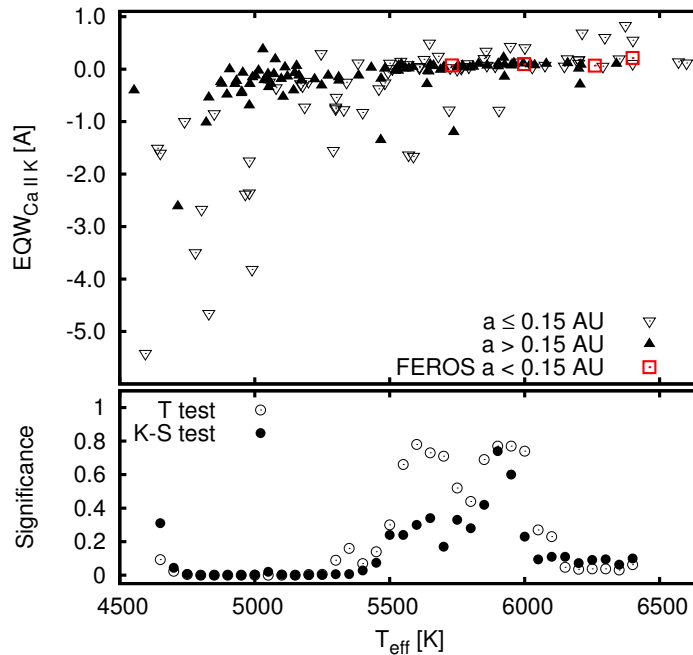


Figure 2.5: *Top:* dependence of the equivalent width of the Ca II K emission on the temperature of the parent star. Triangles denote data from HIRES, red squares denote data from FEROS. Exoplanetary systems with $a \leq 0.15$ AU are marked with empty triangles, systems with $a > 0.15$ AU are marked with full triangles. FEROS sample consists of exoplanets with semi-major axis $a < 0.15$ AU only. *Bottom:* results of statistical Student’s t -test (empty circles) and Kolmogorov–Smirnov test (full circles) for each of the temperature window as described in the text.

symbolize stars with $T_{\text{eff}} > 5500$ K show only a narrow spread of Ca II K EQWs, while cooler stars have a broad range of these values.

In the first step, we aimed to study the possible connections between the semi-major axes of extrasolar planets and the EQW of Ca II K line core. In the top part of Figure 2.5 we distinguished between stars with close-in and far-out exoplanets. Stars harboring planets with semi-major axes shorter than 0.15 AU are marked with upside down white triangles, while the rest, with semi-major axes longer than 0.15 AU, are marked with black triangles. We divided the sample in this way for two reasons. The first one was the visual inspection of Figure 2.9. A second reason for this division is the theoretical assumption that most exoplanets orbiting solar-type stars with orbital distance less than 0.15 AU are presumed to rotate synchronously with their orbital period (Bodenheimer et al., 2001). The fact that stars with close-in planets tend to have higher Ca II K emission (lower EQWs) than stars with distant planets, can be

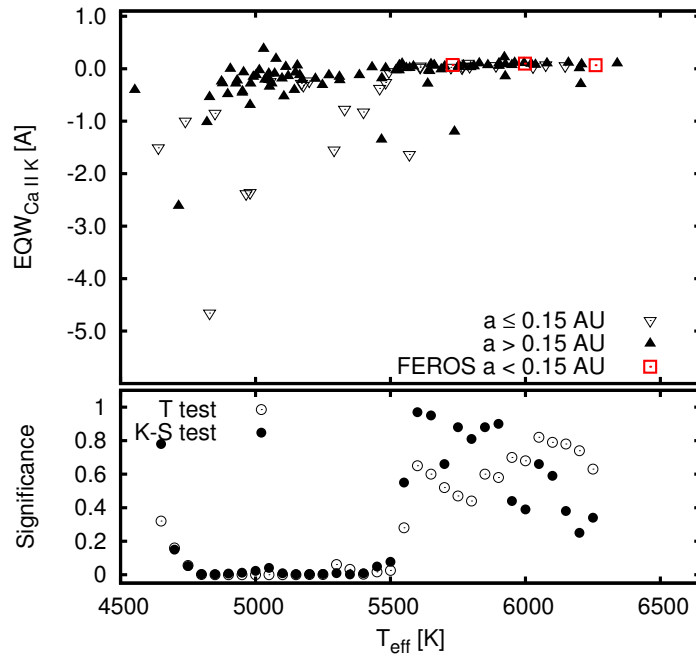


Figure 2.6: *Top:* dependence of the equivalent width of the Ca II K emission on the temperature of the parent star for systems discovered by the RV method only. Triangles denote data from HIRES, red squares denote data from FEROS. Exoplanetary systems with $a \leq 0.15$ AU are marked with empty triangles, systems with $a > 0.15$ AU are marked with full triangles. FEROS sample consists of exoplanets with semi-major axis $a < 0.15$ AU only. *Bottom:* results of statistical Student’s t -test (empty circles) and Kolmogorov–Smirnov test (full circles) for each of the temperature window as described in the text.

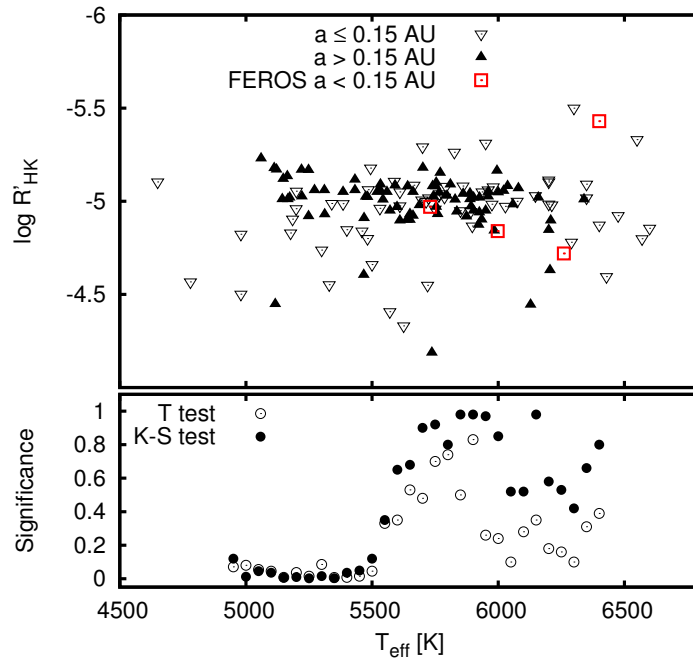


Figure 2.7: *Top:* dependence of the activity index $\log R'_{\text{HK}}$ on the temperature of the parent star. Triangles denote data from HIRES, red squares denote data from FEROS. Exoplanetary systems with $a \leq 0.15$ AU are marked with empty triangles, systems with $a > 0.15$ AU are marked with full triangles. FEROS sample consists of exoplanets with semi-major axis $a < 0.15$ AU only. *Bottom:* results of statistical Student's t -test (empty circles) and Kolmogorov–Smirnov test (full circles) for each of the temperature window as described in the text.

readily seen in Figure 2.5. In Figure 2.9 a difference in activity scatter for close and distant planets can be seen as well.

To verify whether this visual finding is statistically significant, we performed two statistical tests on these two data samples. The first one was the *Student's t-test* (hereafter T test) and the second one was the *Kolmogorov–Smirnov test* (hereafter K–S test) see Appendix C. We studied whether the sample of stars with close-in exoplanets differs in a statistically significant way from the sample of stars with distant planets.

In the case of Student's *t*-test, the null hypothesis is the statement: Two data sets have the same mean. Two means are significantly different if the Student's distribution probability density function $A(t | \nu)$ is higher than our pre-selected value. This value is usually 0.95 or 0.99. Consequently the significance level at which the hypothesis that the means are equal is disproved, is defined as: $1 - A(t | \nu)$. The significance is a number between 0 and 1. A small significance value (0.05 or 0.01) means that the obtained difference is very significant.

For the K–S test is the null hypothesis the statement: Two data sets are drawn from the same population distribution function.

Instead of studying both samples directly, we selected a running window that was 400 K wide and that ran along the temperature axis in steps of 50 K. Only a definite number of data points from each sample fell inside each window. The statistical tests mentioned above were performed on these restricted data samples. The bottom panel of Figure 2.5 shows the resulting values of significance level, labeled as significance in all the plots for each test, and these are plotted versus the center of the current temperature window. The results of the tests (as a function of temperature) show whether the two samples have the same mean or originate from the same distribution function. Figure 2.5 shows that in the region of smaller temperatures ($T_{\text{eff}} \leq 5\,500$ K) the significance is less than 0.05 for both the K–S and T test respectively. The null hypotheses can be disproved on the selected level of significance for the stars with the temperature smaller than 5 500 K. Consequently the difference between the stars with close-in and distant exoplanets is statistically significant for cooler stars with $T_{\text{eff}} \leq 5\,500$ K. On the other hand, the statistical test applied to the hot stars did not show any statistical significance to indicate that the two samples are different.

Before interpreting these results, the selection effects in the sample need to be taken into account. To investigate the impact of selection effects on our results, we omitted the stars with transiting exoplanets from our sample. In Figure 2.6 we plotted the temperature–EQW dependence for this restricted data set. On this reduced data sample, we performed the same statistical tests as for the complete sample, by choosing the same temperature binning for the running window. The results are plotted in the bottom panel of Figure 2.6. Even if the transit data are excluded, the tests show a significant difference between the stars with close-in and distant exoplanets for the

cold stars. However, the size of the sample (especially the number of exoplanets on close-in orbits) has substantially decreased, which made the results of statistical tests less trustworthy.

To verify these trends, we also explored the dependence of the $\log R'_{\text{HK}}$ parameter on the effective temperature of the star (Figure 2.7). This parameter does not show a strong temperature dependence and was described in more detail in Section 2.1.2. Two samples, distinguished by triangle marks according to the semi-major axis of the orbiting exoplanet, can be seen in the top panel of the figure. It is apparent that stars with close-in planets show a wider range of $\log R'_{\text{HK}}$ values than the stars with more distant planets. Cooler stars ($T_{\text{eff}} \leq 5500$ K) with close-in planets have higher values of $\log R'_{\text{HK}}$ and thus higher chromospheric activity.

We performed the same statistical test with the same procedure as described in the paragraphs above. The result is plotted in the bottom part of Figure 2.7. The vertical axis in this figure (and in all the following figures with $\log R'_{\text{HK}}$ parameter dependence) is in the reverse order. The higher value of $\log R'_{\text{HK}}$ parameter, the higher is the stellar activity. The motivation was to unify the direction of increasing stellar activity with the EQW dependencies. The statistical test yielded almost the same result as in the previous cases. The difference between stars with close-in and distant planets is statistically significant for $T_{\text{eff}} \leq 5500$ K. The values of the significance resulting from both statistical tests lie mostly under the 0.05 value and the hypotheses, that the two samples come from one distribution function and have the same mean could be disproved at the 0.05 significance level.

Figure 2.8 depicts the temperature- $\log R'_{\text{HK}}$ dependency for the stars with exoplanets discovered by the RV technique only. The same tests as in the previous cases were applied and the resulting significance value is smaller than 0.05 for the cooler stars.

Semi-major axis dependence

In the preceding section we found statistically significant evidence that the chromospheric activity of the cold stars is connected with the semi-major axis of the orbiting exoplanet. We thus continue exploring the possibility of such a connection in this section. Figure 2.9 gives a plot of the dependence of the EQW of the Ca I K emission on the semi-major axis. Following the results of the statistical tests depicted in Figures 2.5–2.8, we selected only systems with $T_{\text{eff}} \leq 5500$ K. Two distinctive populations are clearly visible in the plot in Figure 2.9. Stars with close-in exoplanets ($a \leq 0.15$ AU) have a broad range of the Ca I K emission, while stars with distant planets ($a > 0.15$ AU) have a narrow range of weak Ca I K emission. As before a distinction is made in the plot between stars with planets discovered by the RV and transit methods. Apparently a significant fraction of stars with close-in exoplanets (but not all of them) have a high Ca I K emission. However, this result may again be

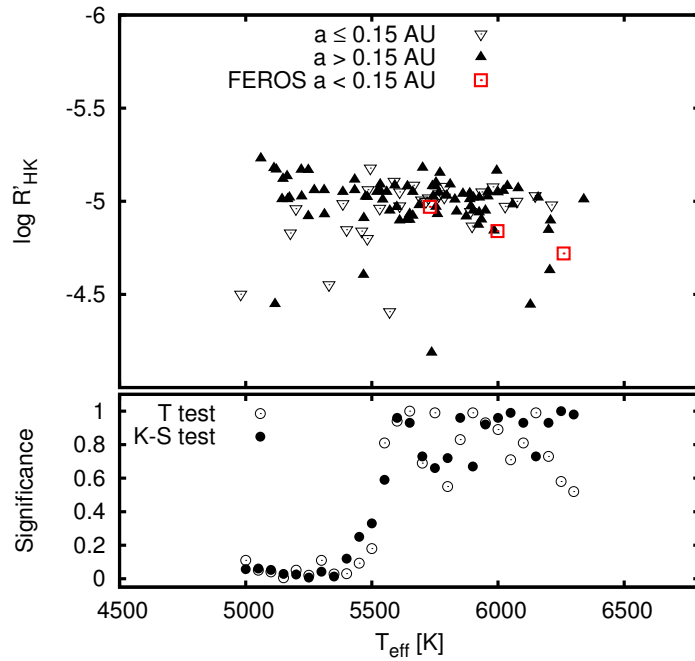


Figure 2.8: *Top:* dependence of the activity index $\log R'_{\text{HK}}$ on the temperature of the parent star for systems discovered by the RV method only. Triangles denote data from HIRES, red squares denote data from FEROS. Exoplanetary systems with $a \leq 0.15$ AU are marked with empty triangles, systems with $a > 0.15$ AU are marked with full triangles. FEROS sample consists of exoplanets with semi-major axis $a < 0.15$ AU only. *Bottom:* results of statistical Student's t -test (empty circles) and Kolmogorov–Smirnov test (full circles) for each of the temperature window as described in the text.

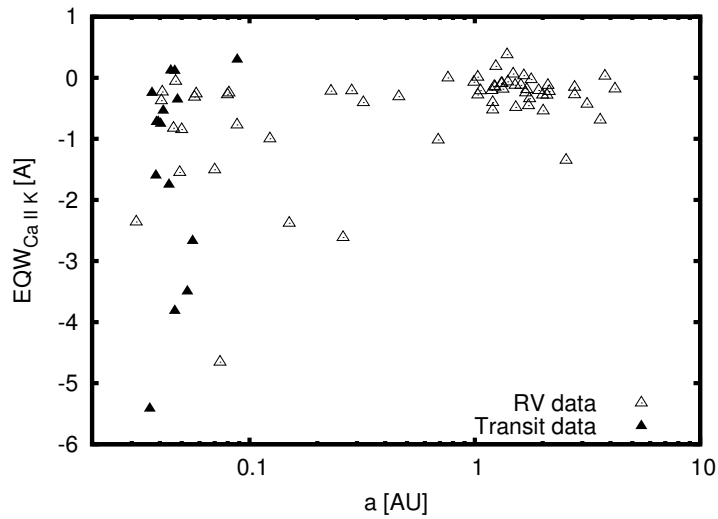


Figure 2.9: Dependence of the EQW of Ca II K emission on the semi-major axis. Included are only systems with $T_{\text{eff}} \leq 5500$ K. Empty triangles are exoplanetary systems discovered by the RV technique, full triangles are systems discovered by the transit method. Note that the semi-major axis is logarithmic.

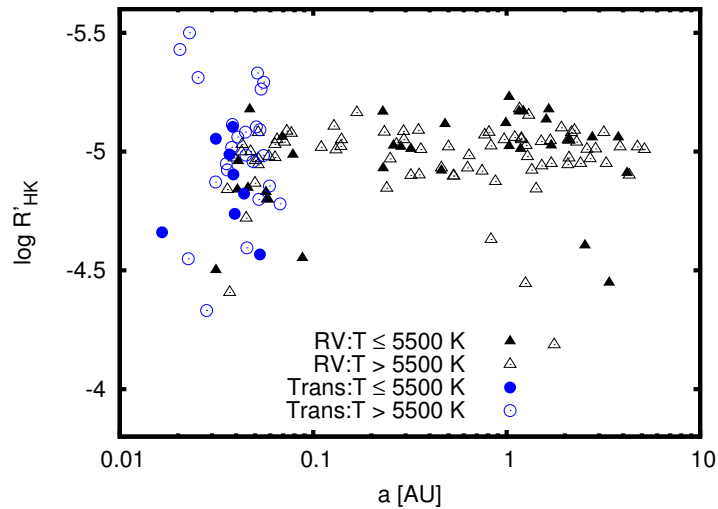


Figure 2.10: Dependence of the activity index $\log R'_{\text{HK}}$ on the semi-major axis. Triangles are exoplanetary systems discovered by the RV technique, circles are systems discovered by the transit method. Note that the semi-major axis is logarithmic.

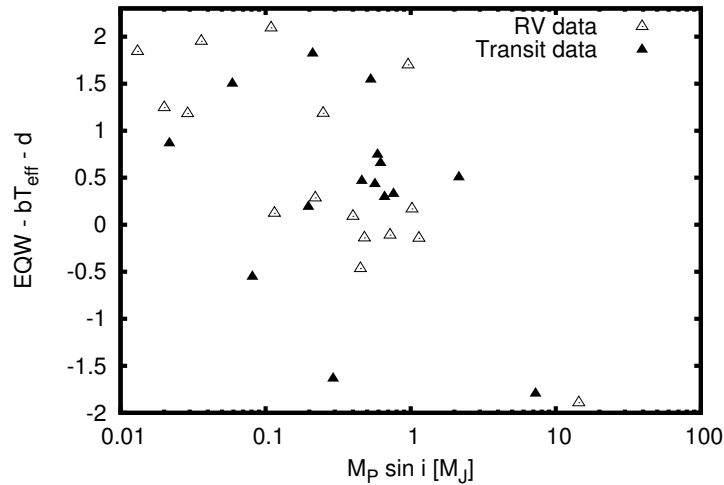


Figure 2.11: Dependence of the modified equivalent width of the Ca II K emission on planet mass. Only stars with $T_{\text{eff}} \leq 5500$ K and $a \leq 0.15$ AU are considered. Empty triangles denote stars with planets detected by the RV method, full triangles the transit method.

affected by selection biases. (It is more difficult to detect distant planets around active stars.)

We also explored the $\log R'_{\text{HK}}$ parameter as a function of the semi-major axis. This is illustrated in Figure 2.10, where is plotted the whole sample of exoplanetary systems without any restrictions. As in the previous case, this figure shows a clear distinction between the stars with close-in planets with semi-major axis less than 0.15 AU and the stars with distant planets. This is mainly caused by hotter stars with transiting exoplanets. Should we concentrate on cold stars with exoplanets detected by the RV technique only, there might be a trend for stars with close-in planets to have higher $\log R'_{\text{HK}}$ values than stars with distant planets, but it is not as pronounced as in the EQW measurements.

Mass dependence

The previous analysis result raises a question as to the reason for the high range of the EQW of Ca II K emission in the sample of cold stars with close-in planets. This phenomenon can have a variety of explanations. It can be connected with the planet orbital period, stellar activity cycle, or stellar ages. It can be a result of any other process that affects the stellar chromosphere. We explored whether the scatter may come from the eccentricity of the orbit, but we could not find any convincing evidence for the eccentricity effect. If there is a dependence of the Ca II K emission on the semi-major axis of the planet, there ought to be some dependence on the mass of the planet,

M_p , as well. This dependence would have to be continuously reduced in the case of sufficiently small planets. However only $M_p \sin i$ is known for most of the extrasolar planets. Nevertheless we selected all stars with temperatures $T \leq 5500$ K and with semi-major axes $a \leq 0.15$ AU and fitted their EQWs of the Ca II K emission using the following function:

$$EQW(M_p, T_{\text{eff}}) = bT_{\text{eff}} + c \log(M_p \sin i) + d, \quad (2.6)$$

where M_p is in the units of Jupiter mass. The usage of this function was motivated by the intention to study the dependence of the mass of the planet on the EQW. However, as was stated above, the EQW depends strongly on the temperature of the star. So the EQW in the expression (2.6) is studied as a function of stellar temperature and planetary mass. Within the fitting procedure we found the following coefficients:

$$b = 3.65 \times 10^{-3} \pm 5.7 \times 10^{-4} \quad [\text{\AA}K^{-1}], \quad (2.7)$$

$$c = -0.392 \pm 0.097 \quad [\text{\AA}], \quad (2.8)$$

$$d = -20.4 \pm 2.9 \quad [\text{\AA}]. \quad (2.9)$$

The b coefficient is significant beyond 6σ , so temperature dependence is very clear. However, the c coefficient is also significant beyond 4σ , and it indicates the statistically significant correlation of the chromospheric activity with the mass of the planet. We applied a statistical F -test to justify the usage of an additional parameter (planet mass) in the above mentioned fitting procedure. The null hypothesis was in this case a statement: The model with 3 parameters does not give a significantly better fit than the 2-parameter fit. The test shows that the significance of the 3-parameter fit (Equation (2.6)) over the 2-parameter fit defined as:

$$EQW(T_{\text{eff}}) = bT_{\text{eff}} + d, \quad (2.10)$$

is 0.003. This means that on the chosen level of significance of 0.05, the test disproved the null hypothesis. These results are illustrated in Figure 2.11, where we plot the modified equivalent width of the Ca II K emission as a function of $m_p \sin i$, showing stars with planets detected by the RV and transit methods. The modified equivalent width is EQW corrected for the strong temperature dependence, namely: $EQW - bT_{\text{eff}} - d$. Lower values of EQW mean higher emission, and thus the host stars with more massive planets show more chromospheric activity. However this correlation might also be affected by the selection effect that it is more difficult to detect a less massive planet around a more active star.

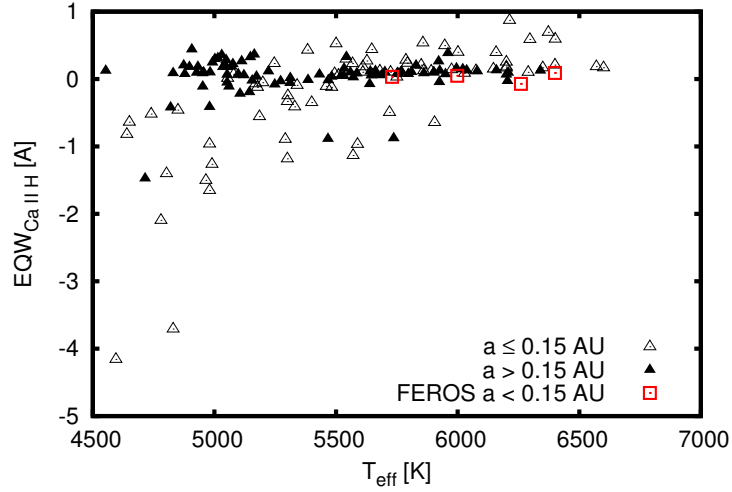


Figure 2.12: Dependence of the equivalent width of Ca II H emission on the temperature of the star. Empty triangles are exoplanetary systems with $a \leq 0.15$ AU, full triangles are systems with $a > 0.15$ AU and red squares are our data from FEROS.

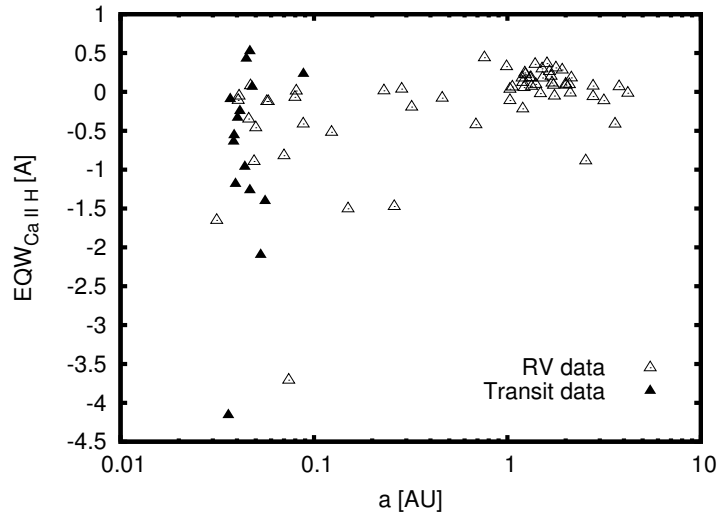


Figure 2.13: Dependence of the equivalent width of Ca II H emission on the semi-major axis. Empty triangles are exoplanetary systems discovered by RV technique, full triangles are systems discovered by transit method.

2.5 Conclusion

In this chapter we focused on the study of possible interaction between the host star and orbiting exoplanet. We searched for possible correlation between the stellar chromospheric activity and the orbital and physical parameters of the exoplanet. As an activity indicators were used two parameters – the equivalent width (EQW) of the core of the Ca II K line and $\log R'_{\text{HK}}$ index. Our sample of more than 200 exoplanetary systems consists of data obtained with two different instruments. The major part of the data were taken from the archive of instrument HIRES, mounted on the Keck I telescope. Data obtained with instrument FEROS located on La Silla in Chile form the minor part of the sample.

Our main aim was the statistical study of the diversity of two subsamples of original data, which were sorted out according to the semi-major axis a of the orbiting exoplanet. First group consisted of stars with close-in exoplanets (semi-major axis less than 0.15 AU) and the second one consisted of systems with exoplanets located further out (semi-major axis greater than 0.15 AU).

For this purpose we performed two statistical tests – the Kolmogorov–Smirnov test and Student’s t -test on our two data samples. As a result we found statistically significant evidence that the EQW of the Ca II K emission in the spectra of planet host stars with effective temperature less than 5 500 K as well as their $\log R'_{\text{HK}}$ activity index depend on the semi-major axis of the exoplanet (see Figures 2.5 and 2.7). More specifically, cool stars ($T_{\text{eff}} \leq 5\,500\text{ K}$) with close-in planets ($a \leq 0.15\text{ AU}$) generally have higher Ca II K emission than stars with more distant planets. This means that a close-in planet can affect the level of the chromospheric activity of its host star and can heat the chromosphere of the star.

We also considered the selection effects caused by the discovery method of exoplanets, since these can significantly distort the results. Our sample of more than 200 stars consists of exoplanetary systems discovered by two different methods. These are the RV method and the transit method (both these methods are described in the Introduction together with the biases which are characteristic for each method). These two techniques have very different criteria for selecting the exoplanetary candidates. The RV measurements concentrate on low-activity stars, whereas transit technique does not put any constraints concerning activity on the stars. In more detail, the general sample of transiting exoplanets is biased towards the planets on close-in orbit. As a consequence, the scatter among the data in the top part of Figure 2.5 (close-in exoplanets orbiting cooler star) was caused mainly by a selection effect. Nevertheless, we performed the same statistical test on the exoplanetary systems, divided according to the semi-major axis and discovered by RV technique only. The results are given in the

Figures 2.6 and 2.8. The results of the statistical tests remained to be significant, even for such a restricted sample.

Moreover, we have found statistically significant evidence that the Ca II K emission of the host star (for $T_{\text{eff}} \leq 5\,500\text{ K}$ and $a \leq 0.15\text{ AU}$) increases with the mass of the planet.

The biggest disadvantage of the analysis performed in this chapter is the size of the RV exoplanets sample. The statistical tests depicted in Figures 2.6 and 2.8 are based on quite a low number of exoplanets with semi-major axes smaller than 0.15 AU. The need for a larger data sample is evident in this case. Moreover the trends and correlation may be affected by selection effects and should be revisited when less biased sample of stars with planets becomes available.

Our results were presented in the paper Krejčová & Budaj (2012). Recently Shkolnik (2013) presented a study in the far ultraviolet (FUV) and near ultraviolet (NUV) region of 272 stars hosting extrasolar planets. She concentrated on the search for increased stellar activity caused by star–planet interaction. She found a statistically significant evidence, that the stars with close-in exoplanets discovered by RV technique are more FUV-active than the stars with more distant planets.

If the findings based on the Ca II K emission prove to be valid for more unbiased sample it raises the question of how this star–planet interaction works and why it operates up to $a = 0.15\text{ AU}$? If it was caused by the tides of the planet, one would expect that the stellar activity would gradually decrease with a , which seems not to be the case. We suggest that it may be due to the magnetic interaction that scales with the magnetic field of the planet. This magnetic field may be very sensitive to the rotation profile of the planet, which is subject to strong synchronization.

APPENDIX A

LCQUAD4.F – PARAMETER DETERMINATION (FORTRAN77 CODE)

```
C      A program to fit the observed light-curve of a planet transit
C      Analytic expressions of Mandel & Agol are  $\chi^2$  minimized
C      by a simplex method to get:
C      p=Rplanet/Rstar
C      dinc=inclination of the orbit
C      tmin=time of the mid transit
C      rstar/a=radius of the star relative to the semimajor axis
C
C      input:
C      lcquad4.in –fixed u1,u2 quadratic limb darkening coeff.
C                  aorb is only formal and is used only to calculate
C                  the starting value and final rstar/a
C      lc.dat – time measured from the center of the transit R
C              in days, normalized flux, sigma (error)
C      output:
C      screen –coordinates of the final simplex
C      lc.out   1.column – time with homogeneous step,
C              2.column – normalized flux with the limb darkening
C              3.column – normalized flux without the limb darkening
C      lc.out2  1.column time of observation
C              2.column is not important
C              3.column best fit lightcurve
C              normalized flux with the limb darkening
C              4.column residuals of the data from fit
C              (observed – calculated)
C
C      implicit double precision (a-h,o-z)
C      parameter(ndat=10000,mdim=5,ndim=4)
C      dimension amu0(ndat),amu1(ndat),z(ndat),x(ndim),xx(ndim)
p      ,tdat(ndat),time(ndat),amudat(ndat),sigdat(ndat)
p      ,pmtrx(mdim,ndim),y(mdim)
C      open(2,file='lcquad4.in',status='old')
C      read(2,*)
C      read(2,*)u1,u2
C      read(2,*)
C      read(2,*)porb,aorb,dtime
C      read(2,*)
C      read(2,*)p,dinc,rstar,tmin
C      read(2,*)
```

```

    read(2,*)dp, ddinc, drstar, dtmin
    close(2)
    open(2, file='lc.dat', status='old')
    i=1
10  read(2,*,end=20,err=20) tdat(i), amudat(i), sigdat(i)
    tdat(i)=tdat(i)*3600.d0*24.d0
    i=i+1
    goto 10
20  nz=i-1
    write(6,*)'nz=',nz
    close(2)
    emjup=1.89914e30
    rjup=7.149e9
    rsun=6.9599e10
    grav=6.673d-8
    emsol=1.9892e33
    au=1.4960e13
    pi=3.14159265358d0
    porb=porb*24.d0*3600.d0
    dinc=dinc/180.d0*pi
    aorb=aorb*au
    dtime=dtime*24.d0*3600.d0
    tmin=tmin*24.d0*3600.d0
    dtmin=dtmin*24.d0*3600.d0
    rstar=rstar*rsun/aorb
    drstar=drstar*rsun/aorb
    ddinc=ddinc/180.d0*pi

C    definition of the initial simplex
    x(1)=p
    x(2)=dinc
    x(3)=tmin
    x(4)=rstar
    xx(1)=x(1)
    xx(2)=x(2)
    xx(3)=x(3)
    xx(4)=x(4)
    pmtrx(1,1)=xx(1)
    pmtrx(1,2)=xx(2)
    pmtrx(1,3)=xx(3)
    pmtrx(1,4)=xx(4)
    y(1)=funk(nz, ndat, ndim, xx, tdat, amudat, sigdat, porb, aorb, u1, u2)
    xx(1)=x(1)+dp
    xx(2)=x(2)
    xx(3)=x(3)
    xx(4)=x(4)
    pmtrx(2,1)=xx(1)
    pmtrx(2,2)=xx(2)
    pmtrx(2,3)=xx(3)
    pmtrx(2,4)=xx(4)
    y(2)=funk(nz, ndat, ndim, xx, tdat, amudat, sigdat, porb, aorb, u1, u2)
    xx(1)=x(1)
    xx(2)=x(2)+ddinc
    xx(3)=x(3)
    xx(4)=x(4)
    pmtrx(3,1)=xx(1)
    pmtrx(3,2)=xx(2)
    pmtrx(3,3)=xx(3)
    pmtrx(3,4)=xx(4)
    y(3)=funk(nz, ndat, ndim, xx, tdat, amudat, sigdat, porb, aorb, u1, u2)

```

```

xx(1)=x(1)
xx(2)=x(2)
xx(3)=x(3)+dtmin
xx(4)=x(4)
pmtrx(4,1)=xx(1)
pmtrx(4,2)=xx(2)
pmtrx(4,3)=xx(3)
pmtrx(4,4)=xx(4)
y(4)=funkt(nz,ndat,ndim,xx,tdat,amudat,sigdat,porb,aorb,u1,u2)
xx(1)=x(1)
xx(2)=x(2)
xx(3)=x(3)
xx(4)=x(4)+drstar
pmtrx(5,1)=xx(1)
pmtrx(5,2)=xx(2)
pmtrx(5,3)=xx(3)
pmtrx(5,4)=xx(4)
y(5)=funkt(nz,ndat,ndim,xx,tdat,amudat,sigdat,porb,aorb,u1,u2)

call AMOEBA(pmtrx,Y,mdim,ndim,NDIM,1.d-4,ITER
p ,nz,ndat,amudat,tdat,sigdat,porb,aorb,u1,u2)
write(6,*)'iter=',iter
write(6,*)'Coordinates of the final simplex:'
write(6,*)'Rp/Rstar',dinc[deg],tmin[day],rstar/a:'
do i=1,mdim
write(6,*)pmtrx(i,1),pmtrx(i,2)*180.d0/pi
p ,pmtrx(i,3)/24.d0/3600.d0,pmtrx(i,4)
enddo
write(*,*)'Y',Y
C lightcurve1
p=pmtrx(1,1)
dinc=pmtrx(1,2)
tmin=pmtrx(1,3)
rstar=pmtrx(1,4)
C duration of the transit assuming circular orbit
tdur=(rstar+p*rstar)**2*aorb**2-(aorb*dcos(dinc))**2
tdur=tdur/aorb**2/(1.d0-(dcos(dinc))**2)
tdur=dsqrt(tdur)
tdur=dasin(tdur)
tdur=porb/pi*tdur
write(6,*)'transit duration assuming e=0 in days:'
write(6,*)tdur/24.d0/3600.d0
do i=1,nz
time(i)=-dtime+2.d0*dtime/dble(nz-1)*dble(i-1)
hlp=2.d0*pi*(time(i)-tmin)/porb
z(i)=1.d0/rstar*dsqrt(dsin(hlp)**2+dcos(dinc)**2*dcos(hlp)**2)
enddo
call occultquad(z,u1,u2,p,amu0,amu1,nz,ndat)
open(3,file='lc.out',status='unknown')
do i=1,nz
write(3,30)time(i)/3600.d0/24.d0,z(i),amu0(i),amu1(i)
enddo
30 format(e15.7,3e14.6)
close(3)
C lightcurve2
do i=1,nz
hlp=2.d0*pi*(tdat(i)-tmin)/porb
z(i)=1.d0/rstar*dsqrt(dsin(hlp)**2+dcos(dinc)**2*dcos(hlp)**2)
enddo
call occultquad(z,u1,u2,p,amu0,amu1,nz,ndat)

```

APPENDIX A. LCQUAD4.F – PARAMETER DETERMINATION

```

    open(3, file='lc.out2', status='unknown')
    do i=1,nz
      write(3,30) tdat(i)/3600.d0/24.d0, z(i), amuo1(i)
p      , amudat(i)-amu01(i)
    enddo
    close(3)
    stop
    end

C
=====
      function funk(nz, ndat, ndim, x, tdat, amudat, sigdat, porb, aorb, u1, u2)
C      function to be minimized
      implicit double precision (a-h, o-z)
      dimension amuo1(ndat), amu0(ndat)
p      , amudat(ndat), tdat(ndat), sigdat(ndat)
p      , z(ndat), x(ndim)
      p=x(1)
      dinc=x(2)
      tmin=x(3)
      rstar=x(4)
      pi=3.14159265358d0
      do i=1,nz
        hlp=2.d0*pi*(tdat(i)-tmin)/porb
        z(i)=1.d0/rstar*dsqrt(dsin(hlp)**2+dcos(dinc)**2*dcos(hlp)**2)
      enddo
      call occultquad(z, u1, u2, p, amuo1, amu0, nz, ndat)
      funk=0.d0
      do i=1,nz
        funk=funk+(amuo1(i)-amudat(i))**2/sigdat(i)**2
      enddo
      return
      end

C
=====
      subroutine occultquad(z0, u1, u2, p, muo1, mu0, nz, ndat)
C      This routine computes the lightcurve for occultation
C      of a quadratically limb-darkened source without microlensing.
C      Please cite Mandel & Agol (2002) if you make use of this routine
C      in your research.
C      Please report errors or bugs to agol@tapir.caltech.edu
      implicit none
      integer i, nz, ndat
      double precision z0(ndat), u1, u2, p, muo1(ndat), mu0(ndat),
&      mu(ndat), lambdad(ndat), etad(ndat), lambdae(ndat), lam,
&      pi, x1, x2, x3, z, omega, kap0, kap1, q, Kk, Ek, Pk, n, ellec, ellk, rj
      if(abs(p-0.5d0).lt.1.d-3) p=0.5d0

C
C Input:
C
C rs radius of the source (set to unity)
C z0 impact parameter in units of rs
C p occulting star size in units of rs
C u1 linear limb-darkening coefficient (gamma_1 in paper)
C u2 quadratic limb-darkening coefficient (gamma_2 in paper)
C
C Output:
C
C muo1 fraction of flux at each z0 for a limb-darkened source
C mu0 fraction of flux at each z0 for a uniform source
C

```

```

C Now, compute pure occultation curve:
  omega=1.d0-u1/3.d0-u2/6.d0
  pi=acos(-1.d0)
C Loop over each impact parameter:
  do i=1,nz
C substitute z=z0(i) to shorten expressions
  z=z0(i)
  x1=(p-z)**2
  x2=(p+z)**2
  x3=p**2-z**2
C the source is unocculted:
C Table 3, I.
  if(z.ge.1.d0+p) then
    lambdad(i)=0.d0
    etad(i)=0.d0
    lambdae(i)=0.d0
    goto 10
  endif
C the source is completely occulted:
C Table 3, II.
  if(p.ge.1.d0.and.z.le.p-1.d0) then
    lambdad(i)=1.d0
    etad(i)=1.d0
    lambdae(i)=1.d0
    goto 10
  endif
C the source is partly occulted and the occulting object crosses the limb:
C Equation (26):
  if(z.ge.abs(1.d0-p).and.z.le.1.d0+p) then
    kap1=acos(min((1.d0-p*p+z*z)/2.d0/z,1.d0))
    kap0=acos(min((p*p+z*z-1.d0)/2.d0/p/z,1.d0))
    lambdae(i)=p*p*kap0+kap1
    lambdae(i)=(lambdae(i)-0.5d0*sqrt(max(4.d0*z*z-
& (1.d0+z*z-p*p)**2,0.d0)))/pi
  endif
C the occulting object transits the source star (but doesn't
C completely cover it):
  if(z.le.1.d0-p) lambdae(i)=p*p
C the edge of the occulting star lies at the origin- special
C expressions in this case:
  if(abs(z-p).lt.1.d-4*(z+p)) then
C Table 3, Case V.:
  if(z.ge.0.5d0) then
    lam=0.5d0*pi
    q=0.5d0/p
    Kk=ellk(q)
    Ek=ellec(q)
C Equation 34: lambda_3
    lambdad(i)=1.d0/3.d0+16.d0*p/9.d0/pi*(2.d0*p*p-1.d0)*Ek-
& (32.d0*p**4-20.d0*p*p+3.d0)/9.d0/pi/p*Kk
C Equation 34: eta_1
    etad(i)=1.d0/2.d0/pi*(kap1+p*p*(p*p+2.d0*z*z)*kap0-
& (1.d0+5.d0*p*p+z*z)/4.d0*sqrt((1.d0-x1)*(x2-1.d0)))
    if(p.eq.0.5d0) then
C Case VIII: p=1/2, z=1/2
    lambdad(i)=1.d0/3.d0-4.d0/pi/9.d0
    etad(i)=3.d0/32.d0
    endif
    goto 10
  else

```

APPENDIX A. LCQUAD4.F – PARAMETER DETERMINATION

```

C Table 3, Case VI.:
    lam=0.5d0*pi
    q=2.d0*p
    Kk=ellk(q)
    Ek=ellec(q)
C Equation 34: lambda_4
    lambdad(i)=1.d0/3.d0+2.d0/9.d0/pi*(4.d0*(2.d0*p*p-1.d0)*Ek+
&
    (1.d0-4.d0*p*p)*Kk)
C Equation 34: eta_2
    etad(i)=p*p/2.d0*(p*p+2.d0*z*z)
    goto 10
endif
endif
C the occulting star partly occults the source and crosses the limb:
C Table 3, Case III:
    if((z.gt.0.5d0+abs(p-0.5d0).and.z.lt.1.d0+p).or.(p.gt.0.5d0.
&
    and.z.gt.abs(1.d0-p)*1.0001d0.and.z.lt.p)) then
    lam=0.5d0*pi
    q=sqrt((1.d0-(p-z)**2)/4.d0/z/p)
    Kk=ellk(q)
    Ek=ellec(q)
    n=1.d0/x1-1.d0
    Pk=Kk-n/3.d0*rj(0.d0,1.d0-q*q,1.d0,1.d0+n)
C Equation 34, lambda_1:
    lambdad(i)=1.d0/9.d0/pi/sqrt(p*z)*(((1.d0-x2)*(2.d0*x2+
&
    x1-3.d0)-3.d0*x3*(x2-2.d0))*Kk+4.d0*p*z*(z*z+
&
    7.d0*p*p-4.d0)*Ek-3.d0*x3/x1*Pk)
    if(z.lt.p) lambdad(i)=lambdad(i)+2.d0/3.d0
C Equation 34, eta_1:
    etad(i)=1.d0/2.d0/pi*(kap1+p*p*(p*p+2.d0*z*z)*kap0-
&
    (1.d0+5.d0*p*p+z*z)/4.d0*sqrt((1.d0-x1)*(x2-1.d0)))
    goto 10
endif
C the occulting star transits the source:
C Table 3, Case IV.:
    if(p.le.1.d0.and.z.le.(1.d0-p)*1.0001d0) then
    lam=0.5d0*pi
    q=sqrt((x2-x1)/(1.d0-x1))
    Kk=ellk(q)
    Ek=ellec(q)
    n=x2/x1-1.d0
    Pk=Kk-n/3.d0*rj(0.d0,1.d0-q*q,1.d0,1.d0+n)
C Equation 34, lambda_2:
    lambdad(i)=2.d0/9.d0/pi/sqrt(1.d0-x1)*((1.d0-5.d0*z*z+p*p+
&
    x3*x3)*Kk+(1.d0-x1)*(z*z+7.d0*p*p-4.d0)*Ek-3.d0*x3/x1*Pk)
    if(z.lt.p) lambdad(i)=lambdad(i)+2.d0/3.d0
    if(abs(p+z-1.d0).le.1.d-4) then
    lambdad(i)=2/3.d0/pi*acos(1.d0-2.d0*p)-4.d0/9.d0/pi*
&
    sqrt(p*(1.d0-p))*(3.d0+2.d0*p-8.d0*p*p)
    endif
C Equation 34, eta_2:
    etad(i)=p*p/2.d0*(p*p+2.d0*z*z)
    endif
10 continue
C Now, using equation (33):
    mu0(i)=1.d0-((1.d0-u1-2.d0*u2)*lambdae(i)+(u1+2.d0*u2)*
&
    lambdad(i)+u2*etad(i))/omega
C Equation 25:
    mu0(i)=1.d0-lambdae(i)
enddo

```

```

return
end

FUNCTION rc(x,y)
REAL*8 rc,x,y,ERRTOL,TINY,SQRTNY,BIG,TNMG,COMP1,COMP2,THIRD,C1,C2,
*C3,C4
PARAMETER (ERRTOL=.04d0,TINY=1.69d-38,SQRTNY=1.3d-19,BIG=3.d37,
*TNMG=TINY*BIG,COMP1=2.236d0/SQRTNY,COMP2=TNMG*TNMG/25.d0,
*THIRD=1.d0/3.d0,C1=.3d0,C2=1.d0/7.d0,C3=.375d0,C4=9.d0/22.d0)
REAL*8 alamb,ave,s,w,xt,yt
if(x.lt.0..or.y.eq.0..or.(x+abs(y)).lt.TINY.or.(x+
*abs(y)).gt.BIG.or.(y.lt.-COMP1.and.x.gt.0..and.x.lt.COMP2)) pause
*'invalid arguments in rc'
if(y.gt.0.d0)then
xt=x
yt=y
w=1.
else
xt=x-y
yt=-y
w=sqrt(x)/sqrt(xt)
endif
1 continue
alamb=2.d0*sqrt(xt)*sqrt(yt)+yt
xt=.25d0*(xt+alamb)
yt=.25d0*(yt+alamb)
ave=THIRD*(xt+yt+yt)
s=(yt-ave)/ave
if(abs(s).gt.ERRTOL)goto 1
rc=w*(1.d0+s*s*(C1+s*(C2+s*(C3+s*C4)))/sqrt(ave)
return
END

```

C (C) Copr. 1986-92 Numerical Recipes Software

```

FUNCTION rj(x,y,z,p)
REAL*8 rj,p,x,y,z,ERRTOL,TINY,BIG,C1,C2,C3,C4,C5,C6,C7,C8
PARAMETER (ERRTOL=.05d0,TINY=2.5d-13,BIG=9.d11,C1=3.d0/14.d0,
*C2=1.d0/3.d0,C3=3.d0/22.d0,C4=3.d0/26.d0,C5=.75d0*C3,
*C6=1.5d0*C4,C7=.5d0*C2,C8=C3+C3)
CU USES rc,rf
REAL*8 a,alamb,alpha,ave,b,beta,delp,delx,dely,delz,ea,eb,ec,ed,
*ee,fac,pt,rcx,rho,sqrtx,sqrty,sqrtz,sum,tau,xt,yt,zt,rc,rf
if(min(x,y,z).lt.0..or.min(x+y,x+z,y+z,abs(p)).lt.TINY.or.max(x,y,
*z,abs(p)).gt.BIG) pause 'invalid arguments in rj'
sum=0.d0
fac=1.d0
if(p.gt.0.d0)then
xt=x
yt=y
zt=z
pt=p
else
xt=min(x,y,z)
zt=max(x,y,z)
yt=x+y+z-xt-zt
a=1.d0/(yt-pt)
b=a*(zt-yt)*(yt-xt)
pt=yt+b
rho=xt*zt/yt
tau=p*pt/yt

```

```

        rcx=rc (rho , tau )
    endif
1  continue
    sqrtx=sqrt ( xt )
    sqrty=sqrt ( yt )
    sqrtz=sqrt ( zt )
    alamb=sqrtx*(sqrty+sqrtz)+sqrty*sqrtz
    alpha=(pt*(sqrtx+sqrty+sqrtz)+sqrtx*sqrty*sqrtz)**2
    beta=pt*(pt+alamb)**2
    sum=sum+fac*rc (alpha , beta )
    fac=.25d0*fac
    xt=.25d0*(xt+alamb)
    yt=.25d0*(yt+alamb)
    zt=.25d0*(zt+alamb)
    pt=.25d0*(pt+alamb)
    ave=.2d0*(xt+yt+zt+pt+pt)
    delx=(ave-xt)/ave
    dely=(ave-yt)/ave
    delz=(ave-zt)/ave
    delp=(ave-pt)/ave
    if (max (abs (delx) , abs (dely) , abs (delz) , abs (delp)) .gt .ERRTOL) goto 1
    ea=delx*(dely+delz)+dely*delz
    eb=delx*dely*delz
    ec=delp**2
    ed=ea-3.d0*ec
    ee=eb+2.d0*delp*(ea-ec)
    rj=3.d0*sum+fac*(1.d0+ed*(-C1+C5*ed-C6*ee)+eb*(C7+delp*
*(-C8+delp*C4))+delp*ea*(C2-delp*C3)-C2*delp*ec)/(ave*sqrt(ave))
    if (p.le .0.d0) rj=a*(b*rj+3.d0*(rcx-rf(xt,yt,zt)))
    return
END

```

C (C) Copr. 1986–92 Numerical Recipes Software

```

function ellec(k)
implicit none
double precision k,m1,a1,a2,a3,a4,b1,b2,b3,b4,ee1,ee2,ellec
C Computes polynomial approximation for the complete elliptic
C integral of the second kind (Hasting's approximation):
m1=1.d0-k*k
a1=0.44325141463d0
a2=0.06260601220d0
a3=0.04757383546d0
a4=0.01736506451d0
b1=0.24998368310d0
b2=0.09200180037d0
b3=0.04069697526d0
b4=0.00526449639d0
ee1=1.d0+m1*(a1+m1*(a2+m1*(a3+m1*a4)))
ee2=m1*(b1+m1*(b2+m1*(b3+m1*b4)))*log(1.d0/m1)
ellec=ee1+ee2
return
end

function ellk(k)
implicit none
double precision a0,a1,a2,a3,a4,b0,b1,b2,b3,b4,ellk,
& ek1,ek2,k,m1
C Computes polynomial approximation for the complete elliptic
C integral of the first kind (Hasting's approximation):
m1=1.d0-k*k

```

```

a0=1.38629436112 d0
a1=0.09666344259 d0
a2=0.03590092383 d0
a3=0.03742563713 d0
a4=0.01451196212 d0
b0=0.5d0
b1=0.12498593597 d0
b2=0.06880248576 d0
b3=0.03328355346 d0
b4=0.00441787012 d0
ek1=a0+m1*(a1+m1*(a2+m1*(a3+m1*a4)))
ek2=(b0+m1*(b1+m1*(b2+m1*(b3+m1*b4))))*log(m1)
ellk=ek1-ek2
return
end

```

FUNCTION rf(x,y,z)

REAL*8 rf,x,y,z,ERRTOL,TINY,BIG,THIRD,C1,C2,C3,C4

PARAMETER (ERRTOL=.08d0,TINY=1.5d-38,BIG=3.d37,THIRD=1.d0/3.d0,
*C1=1.d0/24.d0,C2=.1d0,C3=3.d0/44.d0,C4=1.d0/14.d0)

REAL*8 alamb,ave,delx,dely,delz,e2,e3,sqrtx,sqrty,sqrtz,xt,yt,zt

if (min(x,y,z).lt.0.d0.or.min(x+y,x+z,y+z).lt.TINY.or.max(x,y,
*z).gt.BIG)**pause** 'invalid arguments in rf'

xt=x

yt=y

zt=z

1 **continue**

sqrtx=sqrt(xt)

sqrty=sqrt(yt)

sqrtz=sqrt(zt)

alamb=sqrtx*(sqrty+sqrtz)+sqrty*sqrtz

xt=.25d0*(xt+alamb)

yt=.25d0*(yt+alamb)

zt=.25d0*(zt+alamb)

ave=THIRD*(xt+yt+zt)

delx=(ave-xt)/ave

dely=(ave-yt)/ave

delz=(ave-zt)/ave

if (max(abs(delx),abs(dely),abs(delz)).gt.ERRTOL)**goto** 1

e2=delx*dely-delz**2

e3=delx*dely*delz

rf=(1.d0+(C1*e2-C2-C3*e3)*e2+C4*e3)/sqrt(ave)

return

END

C (C) Copr. 1986-92 Numerical Recipes Software ONL&WR2.

C

SUBROUTINE AMOEBA(P,Y,MP,NP,NDIM,FTOL,ITER

p,nz,ndat,amudat,tdat,sigdat,porb,aorb,u1,u2)

implicit double precision (a-h,o-z)

dimension tdat(ndat),amudat(ndat),sigdat(ndat)

PARAMETER (NMAX=20,ALPHA=1.0,BETA=0.5,GAMMA=2.0,ITMAX=10000)

external funk

DIMENSION P(MP,NP),Y(MP),PR(NMAX),PRR(NMAX),PBAR(NMAX)

MPTS=NDIM+1

ITER=0

1 ILO=1

IF (Y(1).GT.Y(2))**THEN**

IHI=1

INHI=2

APPENDIX A. LCQUAD4.F – PARAMETER DETERMINATION

```

ELSE
  IHI=2
  INHI=1
ENDIF
DO 11 I=1,MPTS
  IF (Y(I).LT.Y(ILO)) ILO=I
  IF (Y(I).GT.Y(IHI))THEN
    INHI=IHI
    IHI=I
  ELSE IF (Y(I).GT.Y(INHI))THEN
    IF (I.NE.IHI) INHI=I
  ENDIF
11 CONTINUE
RTOL=2.*ABS(Y(IHI)-Y(ILO))/(ABS(Y(IHI))+ABS(Y(ILO)))
IF (RTOL.LT.FTOL)RETURN
IF (ITER.EQ.ITMAX) PAUSE 'Amoeba_>exceeding_>maximum_>iterations.'
ITER=ITER+1
DO 12 J=1,NDIM
  PBAR(J)=0.
12 CONTINUE
DO 14 I=1,MPTS
  IF (I.NE.IHI)THEN
    DO 13 J=1,NDIM
      PBAR(J)=PBAR(J)+P(I,J)
13 CONTINUE
    ENDIF
14 CONTINUE
DO 15 J=1,NDIM
  PBAR(J)=PBAR(J)/NDIM
  PR(J)=(1.+ALPHA)*PBAR(J)-ALPHA*P(IHI,J)
15 CONTINUE
c YPR=FUNK(PR)
ypr=funk (nz, ndat, ndim, pr, tdat, amudat, sigdat, porb, aorb, u1, u2)
IF (YPR.LE.Y(ILO))THEN
  DO 16 J=1,NDIM
    PRR(J)=GAMMA*PR(J)+(1.-GAMMA)*PBAR(J)
16 CONTINUE
c YPRR=FUNK(PRR)
yprr=funk (nz, ndat, ndim, prr, tdat, amudat, sigdat, porb, aorb, u1, u2)
IF (YPRR.LT.Y(ILO))THEN
  DO 17 J=1,NDIM
    P(IHI,J)=PRR(J)
17 CONTINUE
  Y(IHI)=YPRR
  ELSE
    DO 18 J=1,NDIM
      P(IHI,J)=PR(J)
18 CONTINUE
  Y(IHI)=YPR
  ENDIF
ELSE IF (YPR.GE.Y(INHI))THEN
  IF (YPR.LT.Y(IHI))THEN
    DO 19 J=1,NDIM
      P(IHI,J)=PR(J)
19 CONTINUE
  Y(IHI)=YPR
  ENDIF
DO 21 J=1,NDIM
  PRR(J)=BETA*P(IHI,J)+(1.-BETA)*PBAR(J)
21 CONTINUE

```

```

c      YPRR=FUNK(PRR)
      yprrr=funk(nz,ndat,ndim,pr,tdat,amudat,sigdat,porb,aorb,u1,u2)
      IF(YPRR.LT.Y(IHI))THEN
        DO 22 J=1,NDIM
          P(IHI,J)=PRR(J)
22      CONTINUE
        Y(IHI)=YPRR
      ELSE
        DO 24 I=1,MPTS
          IF(I.NE.ILO)THEN
            DO 23 J=1,NDIM
              PR(J)=0.5*(P(I,J)+P(ILO,J))
              P(I,J)=PR(J)
23      CONTINUE
          Y(I)=FUNK(PR)
c      y(i)=funk(nz,ndat,ndim,pr,tdat,amudat,sigdat
p      ,porb,aorb,u1,u2)
          ENDF
24      CONTINUE
        ENDF
      ELSE
        DO 25 J=1,NDIM
          P(IHI,J)=PR(J)
25      CONTINUE
        Y(IHI)=YPR
      ENDF
      GO TO 1
      END

```

C (C) Copr. 1986-92 Numerical Recipes

APPENDIX B

MONTECHYBY4.F – MONTE CARLO SIMULATION (FORTRAN77 CODE)

*C Program for calculation of the uncertainties of parameters calculated
C by program lcquad.f*

```
program montechyby
implicit none
integer ndat, i, j, k, N, LOW, HI, tt, p, r, q, us, ur
include 'merger.inp'
integer S(ndat, tt)
double precision A(ndat), AA(ndat), AAA(ndat), B(ndat), C(ndat),
p EE(ndat), nic(ndat), sig, MM(N, ndat), CC(ndat, tt), CCC(tt), DDD(tt),
p EEE(tt), FFF(tt), pol, ink, str, hve, spol, sink, sstr, shve, ssink,
p ssstr, sspol, sshve, chi2(tt), rchi2(tt)
```

C Input files :

```
lc.dat —> observed data
C      1.column time of observation centered to the middle of
C      the transit
C      2.column relative flux (normalized to unity)
C      3.errors from photometry
lc.out2 —> output of lcquad.f programme
C      1.column time of observation
C      2.column is not important
C      3.column best fit lightcurve
C      4.column residuals of the data from fit
C      (observed - calculated)
lcquad4.in —> subroutine squadra needs input values of
C      parameters see lcquad4.f
merger.inp —> number of measured data and the number
C      of generated random numbers
C Output
screen —> uncertainties of the parameters
C      file —> vysl_sera.txt —> matrix of generated
C      parameters
C      1.-4.column - generated parameters
C      5.column —> chi^2
C      6.column —> reduced chi^2
```

```
open(5, FILE = 'lc.dat')
do 10 i=1, ndat
read (5, *) A(i), AA(i), AAA(i)
```

```
10  enddo
    close(5)

    open(15,FILE = 'lc.out2')
    do 20 k=1,ndat
    read (15,*) B(k),nic(k),C(k),EE(k)
20  enddo
    close(15)
```

```
C=====
C Calculation of the parameters of the Normal distribution: mu(mean)
C and sigma(standard deviation) which characterize the residuals of
C the fit (Figure 1.8).
C=====
```

```
call Sigma(EE,ndat,sig)
```

```
C=====
C Generation of matrix MM(100000,ndat), in each column are randomly
C generated sets of numbers with normal distribution. The mean (mu)
C value of the distribution could be the measured data(AA) or the
C fitted value(C).
C=====
```

```
call nahodne(sig,C,N,ndat,MM)
```

```
C=====
C Routine Tirand generate a matrix with randomly generated numbers
C from the interval 1–10000. N is the number of digits generated in
C one cycle. Low/Hi is the upper and lower limit of the interval in
C which the numbers should lie. idum is an initialization for function
C ran2(idum) using seed. The output is the matrix S(ndat,tt).
C=====
```

```
LOW=1
HI=10000
```

```
call tirand(LOW,HI,ndat,tt,S)
```

```
do 80 p=1,tt
    do 90 r=1,ndat
    q=S(r,p)
    CC(r,p)=MM(q,r)
```

```
90  enddo
80  enddo
```

```
C=====
C Routine squadra generates parameters for the randomly generated
C synthetic sets of measurements. The output are four (number of
C fitted parameters) matrixes with 10000 rows CCC,DDD,EEE,FFF. Two
C additional columns with chi2 and rchi2 for each set of parameters
C are added into the output file vysl_sera.txt.
C=====
```

```
call squadra(CC,AAA,A,CCC,DDD,EEE,FFF,chi2,ndat,tt,rchi2,
p AA)
```

```
open(36,FILE = 'vysl_sera.txt')
do 14 j=1,tt
write (36,*) CCC(j),DDD(j),EEE(j),FFF(j),chi2(j)
p, rchi2(j)
14  enddo
close(36)
```

```
C=====
```

*C Computation of the standard deviation of each generated set of
C measurement.*

```

pol=0
ink=0
str=0
hve=0

do 3 us=1,tt
    pol=pol+CCC(us)
    ink=ink+DDD(us)
    str=str+EEE(us)
    hve=hve+FFF(us)
3 enddo

pol=pol/tt
ink=ink/tt
str=str/tt
hve=hve/tt

spol=0
sink=0
sstr=0
shve=0
do 2 ur=1,tt
    spol=spol+(pol-CCC(ur))**2
    sink=sink+(ink-DDD(ur))**2
   sstr=sstr+(str-EEE(ur))**2
    shve=shve+(hve-FFF(ur))**2
2 enddo

sspol=dsqrt(spol/(tt-1))
ssink=dsqrt(sink/(tt-1))
ssstr=dsqrt(sstr/(tt-1))
sshve=dsqrt(shve/(tt-1))

write(*,*) 'polomer', sspol
write(*,*) 'inklinace', ssink
write(*,*) 'stred', ssstr
write(*,*) 'hvezda/a', sshve

stop
end

```

C

```

SUBROUTINE Sigma(EE,ndat,sig)
implicit none
integer p,o,ndat
double precision my,suma,BB,sig,EE(ndat)
C Calculates the arithmetic mean from standard deviation.
my=0
do 10 p=1,ndat
    my=my+EE(p)
10 enddo
suma=my/ndat
C Computes the standard deviation of the data.
BB=0
do 20 o=1,ndat
    BB=BB+(suma-EE(o))**2
20 enddo

```

```

sig=dsqrt(BB/(ndat-1))
return
end

```

C

```

SUBROUTINE nahodne(sig,C,N,ndat,MM)
implicit none
integer m,o,N,ndat,seed,idum
double precision sig,MM(N,ndat),C(ndat)
real gasdev

idum=seed
do 70 m=1,ndat
    do 60 o=1,N
        MM(o,m)=(gasdev(idum)*sig)+C(m)
60    enddo
70 enddo
return
end

```

C

```

function gasdev(idum)
implicit none
integer idum,seed
double precision ran2
real gasdev

integer iset
real fac,gset,rsq,v1,v2,ran1
save iset,gset
data iset/0/
if (idum.lt.0) iset=0
if (iset.eq.0) then
1    v1=2.*(ran2(idum))-1.
    v2=2.*(ran2(idum))-1.
    rsq=v1**2+v2**2
    if (rsq.ge.1. .or. rsq.eq.0) goto 1
    fac=sqrt(-2.*log(rsq)/rsq)
    gset=v1*fac
    gasdev=v2*fac
    iset=1
else
    gasdev=gset
    iset=0
endif
return
end

```

C

```

function ran2(idum)
implicit none
integer idum,IM1,IM2,IMM1,IA1,IA2,IQ1,IQ2,IR1,IR2,NTAB,NDIV
double precision ran2,AM,EPS,RNMX
parameter (IM1=2147483563,IM2=2147483399,AM=1./IM1,
p IMM1=IM1-1,IA1=40014,IA2=40692,IQ1=53668,IQ2=52774,
p IR1=12211,IR2=3791,NTAB=32,NDIV=1+IMM1/NTAB,EPS=1.2e-7,
p RNMX=1.-EPS)

integer idum2,j,k,iv(NTAB),iy
save iv,iy,idum2
data idum2/123456789/,iv/NTAB*0/,iy/0/
if (idum.le.0) then
    idum=max(-idum,1)

```

```

        idum2=idum
        do 10 j=NTAB+8,1,-1
            k=idum/IQ1
            idum=IA1*(idum-k*IQ1)-k*IR1
            if (idum .lt. 0) idum=idum+IM1
            if (j .le. NTAB) iv(j)=idum
10        enddo
        iy=iv(1)
        endif
        k=idum/IQ1
        idum=IA1*(idum-k*IQ1)-k*IR1
        if (idum .lt. 0) idum=idum+IM1
        k=idum2/IQ2
        idum2=IA2*(idum2-k*IQ2)-k*IR2
        if (idum2 .lt. 0) idum2=idum2+IM2
        j=1+iy/NDIV
        iy=iv(j)-idum2
        iv(j)=idum
        if (iy .lt. 1) iy=iy+IMM1
        ran2=min(AM*iy ,RNMX)
        return
    end

```

SUBROUTINE tirand(LOW,HI,N,kk,S)

C Generate a random integer sequence: $S(1), S(2), \dots, S(N)$

C such that each element is in the closed interval $\langle \text{LOW}, \text{HI} \rangle$ and

C sampled WITH REPLACEMENT.

```

        implicit none
        INTEGER i , tk , idum , LOW , HI , kk , N , seed
        double precision U(N, kk) , X(N, kk) , ran2
        INTEGER S(N, kk) , IX(N, kk)
        idum=seed
        do 70 i=1,kk
            do 60 tk=1,N
                U(tk , i)=ran2(idum)
                X(tk , i)=dble((HI+1)-LOW)*U(tk , i) + dble(LOW)
                IX(tk , i)=X(tk , i)
                IF(X(tk , i).LT.0 .AND. IX(tk , i).NE.X(tk , i)) IX(tk , i)
p =X(tk , i)-1.D0
                S(tk , i)=IX(tk , i)
60        continue
70        continue
        return
    end

```

SUBROUTINE squadra(AA,BB,tcas ,CC,DD,EE,FF,chi2 , ndat , kk , rchi2 ,

p data)

implicit double precision (a-h,o-z)

integer wx,NN,kk , ll ,mm,tk ,tm,tn ,tp , tr , i , nz , tl , ndat , ii

parameter(mdim=5,ndim=4)

dimension amuo1(ndat) , amuo0(ndat) , z(ndat) , x(ndim) , xx(ndim)

p , tdat(ndat) , time(ndat) , amudat(ndat) , sigdat(ndat)

p , pmtrx(mdim,ndim) , y(mdim) , AA(ndat , kk) , BB(ndat) , CC(kk) , DD(kk) ,

p EE(kk) , tcas(ndat) , FF(kk) , chi2(kk) , rchi2(kk)

p , data(ndat)

NN=ndat

do 90 tr=1,kk

open(2 , file='lcquad4.in' , status='old')

read(2 , *)

```

        read(2,*) u1, u2
        read(2,*)
        read(2,*) porb, aorb, dtime
        read(2,*)
        read(2,*) p, dinc, rstar, tmin
        read(2,*)
        read(2,*) dp, ddinc, drstar, dtmin
        close(2)

        do 91 ii=1,NN
            amudat(ii)=AA(ii, tr)
            sigdat(ii)=BB(ii)
            tdat(ii)=tcas(ii)*3600.d0*24.d0
91    continue
        nz=NN
        emjup=1.89914e30
        rjup=7.149e9
        rsun=6.9599e10
        grav=6.673d-8
        emsol=1.9892e33
        au=1.496e13
        pi=3.14159265358d0
        porb=porb*24.d0*3600.d0
        dinc=dinc/180.d0*pi
        aorb=aorb*au
        dtime=dtime*24.d0*3600.d0
        tmin=tmin*24.d0*3600.d0
        dtmin=dtmin*24.d0*3600.d0
        rstar=rstar*rsun/aorb
        drstar=drstar*rsun/aorb
        ddinc=ddinc/180.d0*pi
        x(1)=p
        x(2)=dinc
        x(3)=tmin
        x(4)=rstar
        xx(1)=x(1)
        xx(2)=x(2)
        xx(3)=x(3)
        xx(4)=x(4)
        pmtrx(1,1)=xx(1)
        pmtrx(1,2)=xx(2)
        pmtrx(1,3)=xx(3)
        pmtrx(1,4)=xx(4)
        y(1)=funk(nz, ndat, ndim, xx, tdat, amudat, sigdat, porb, aorb, u1, u2, NN)
        xx(1)=x(1)+dp
        xx(2)=x(2)
        xx(3)=x(3)
        xx(4)=x(4)
        pmtrx(2,1)=xx(1)
        pmtrx(2,2)=xx(2)
        pmtrx(2,3)=xx(3)
        pmtrx(2,4)=xx(4)
        y(2)=funk(nz, ndat, ndim, xx, tdat, amudat, sigdat, porb, aorb, u1, u2, NN)
        xx(1)=x(1)
        xx(2)=x(2)+ddinc
        xx(3)=x(3)
        xx(4)=x(4)
        pmtrx(3,1)=xx(1)
        pmtrx(3,2)=xx(2)

```

```

pmtrx(3,3)=xx(3)
pmtrx(3,4)=xx(4)
y(3)=funkt(nz,ndat,ndim,xx,tdat,amudat,sigdat,porb,aorb,u1,u2,NN)
xx(1)=x(1)
xx(2)=x(2)
xx(3)=x(3)+dtmin
xx(4)=x(4)
pmtrx(4,1)=xx(1)
pmtrx(4,2)=xx(2)
pmtrx(4,3)=xx(3)
pmtrx(4,4)=xx(4)
y(4)=funkt(nz,ndat,ndim,xx,tdat,amudat,sigdat,porb,aorb,u1,u2,NN)
xx(1)=x(1)
xx(2)=x(2)
xx(3)=x(3)
xx(4)=x(4)+drstar
pmtrx(5,1)=xx(1)
pmtrx(5,2)=xx(2)
pmtrx(5,3)=xx(3)
pmtrx(5,4)=xx(4)
y(5)=funkt(nz,ndat,ndim,xx,tdat,amudat,sigdat,porb,aorb,u1,u2,NN)

call AMOEBA(pmtrx,Y,mdim,ndim,NDIM,1.d-6,ITER
p ,nz,ndat,amudat,tdat,sigdat,porb,aorb,u1,u2)
  CC(tr)=pmtrx(1,1)
  DD(tr)=pmtrx(1,2)*180.d0/pi
  EE(tr)=pmtrx(1,3)/24.d0/3600.d0
  FF(tr)=pmtrx(1,4)
do 65 i=1,4
  xx(i)=pmtrx(1,i)
65 enddo
  chi2(tr)=0.d0
  chi2(tr)=funkt(nz,ndat,ndim,xx,tdat,data,sigdat,porb,aorb,u1,u2
p ,NN)
  rchi2(tr)=chi2(tr)/(dble(nz-ndim))
90 enddo
  return
  end

```

```

function funkt(nz,ndat,ndim,x,tdat,amudat,sigdat,porb,aorb,u1,
p u2,NN)
C function to be minimized
  implicit double precision (a-h,o-z)
  integer ij,NN,is
  dimension amuo1(ndat),amu0(ndat)
p ,amudat(ndat),tdat(ndat),sigdat(ndat)
p ,z(ndat),x(ndim)
  p=x(1)
  dinc=x(2)
  tmin=x(3)
  rstar=x(4)
  pi=3.14159265358 d0
  do ij=1,nz
    hlp=2.d0*pi*(tdat(ij)-tmin)/porb
    z(ij)=1.d0/rstar*dsqrt(dsin(hlp)**2+dcos(dinc)**2*dcos(hlp)
p **2)
  enddo
  call occultquad(z,u1,u2,p,amuo1,amu0,nz,ndat)
  funkt=0.d0
  do is=1,nz

```

APPENDIX B. MONTECHYBY4.F – MONTE CARLO SIMULATION

```
      funk=funk+(amuol(is)-amudat(is))**2/sigdat(is)**2
    enddo
  return
end
```

```
C=====
C      SUBROUTINE occultquad(z0,u1,u2,p,mu0,mu1,nz,ndat)
C      Subroutine occultquad was used in the same reading as in the code lcquad4.f
C      stated in Appendix A
C=====
```

```
C      SUBROUTINE AMOEBA(P,Y,MP,NP,NDIM,FTOL,ITER
C      p,nz,ndat,amudat,tdat,sigdat,porb,aorb,u1,u2)
C      Subroutine amoeba was used in the same reading as in the code lcquad4.f
C      stated in Appendix A
```

APPENDIX C

STATISTICAL TESTS

In this Appendix are described two statistical tests Student's t -test and Kolmogorov–Smirnov test used in this work. Throughout the description we followed the Press et al. (1992)

C.1 Student's t -test

T test is used for determining the significance of a difference of means. The mean \bar{x} was defined in Equation (1.11). The null hypothesis in this case is the statement: Two data sets have the same mean.

The t -value of the T test is computed as:

$$t = \frac{\bar{x}_A - \bar{x}_B}{s_d}, \quad (\text{C.1})$$

where \bar{x}_A and \bar{x}_B are the means of the two samples A and B , and s_d is the standard error of the difference of means defined as:

$$s_d = \sqrt{\frac{\sum_{i \in A} (x_i - \bar{x}_A)^2 + \sum_{i \in B} (x_i - \bar{x}_B)^2}{N_A + N_B - 2} \left(\frac{1}{N_A} + \frac{1}{N_B} \right)}. \quad (\text{C.2})$$

N_A and N_B are the numbers of points in the two samples.

Next we need to evaluate the significance of the t -value for the Student's distribution with $N_A + N_B - 2$ degrees of freedom by the Student's distribution probability density function $A(t | \nu)$ defined as:

$$A(t | \nu) = \frac{1}{\nu^{1/2} B(\frac{1}{2}, \frac{\nu}{2})} \int_{-t}^t \left(1 + \frac{x^2}{\nu} \right)^{-\frac{\nu+1}{2}} dx \quad (\text{C.3})$$

where $B(\frac{1}{2}, \frac{\nu}{2})$ is beta function. $A(t | \nu)$ is the probability, for ν degrees of freedom, that t , which measures the observed difference of means, would be smaller than the observed value if the means were the same.

Limiting values of the $A(t | \nu)$ function are:

$$\begin{aligned} A(0 | \nu) &= 0, \\ A(\infty | \nu) &= 1. \end{aligned}$$

C.2 Kolmogorov–Smirnov test

The K–S test is a statistical test used for determining if two data sets are drawn from the same distribution function. The null hypothesis in this case is the statement: Two data sets are drawn from the same population distribution function. If we disprove the null hypothesis to a certain level of significance we could say that the data come from a different distribution function. In case we are not able to disprove the null hypothesis, we can only say that the two sets could be from one distribution function.

The principle of this statistical test is based on the comparison of two cumulative distribution functions $S_{N_1}(x)$ and $S_{N_2}(x)$ of two data sets. The “measure” of the K–S test D is defined as the maximum value of the absolute difference between two cumulative distribution functions.

$$D = \max_{-\infty < x < \infty} |S_{N_1}(x) - S_{N_2}(x)|. \quad (\text{C.4})$$

The significance level of an observed value D is given by:

$$\text{Probability}(D > \text{observed}) = Q_{\text{KS}} \left(\left[\sqrt{M} + 0.12 + 0.11/\sqrt{M} \right] D \right), \quad (\text{C.5})$$

where M is defined as

$$M = \frac{N_1 N_2}{N_1 + N_2}. \quad (\text{C.6})$$

The function Q_{KS} is

$$Q_{\text{KS}}(\lambda) = 2 \sum_{i=1}^{\infty} (-1)^{i-1} e^{-2i^2 \lambda^2}. \quad (\text{C.7})$$

N_1 and N_2 are the number of data points in the first and second sample. The limiting values of the function are:

$$\begin{aligned} Q_{\text{KS}}(0) &= 1, \\ Q_{\text{KS}}(\infty) &= 0. \end{aligned}$$

APPENDIX D

LIST OF EXOPLANETS USED IN CHAPTER 2

Table D.1: Parameters of exoplanetary systems. Systems below the line at the bottom part of the table describe FEROS data sample. M_p is the planetary mass, i is the orbital inclination, a is the semi-major axis, T_{eff} is the effective temperature of the star, EQW is the equivalent width of the core of the lines Ca II K and H, $\log R'_{\text{HK}}$ is the chromospheric activity indicator, letters T and RV stands for transiting and radial velocity discovery method, respectively. Data taken from <http://www.exoplanet.eu/>.

Object	$M_p \sin i$ [M_J]	P_{orb} [days]	a [AU]	T_{eff} [K]	EQW _K [Å]	EQW _H [Å]	$\log R'_{\text{HK}}$	Detection method
WASP-19 b	1.168	0.78884	0.01655	5500	-	-	-4.66	T
Kepler-10 b	0.0143	0.837495	0.01684	5627	0.1864	0.2681	-	T
WASP-12 b	1.404	1.0914222	0.02293	6300	-	-	-5.5	T
HAT-P-23 b	2.09	1.212884	0.0232	5905	-0.7840	-0.6446	-	T
TrES-3	1.91	1.30618608	0.0226	5720	-0.7795	-0.4953	-4.549	T
CoRoT-1 b	1.03	1.5089557	0.0254	5950	-	-	-5.312	T
CoRoT-2 b	3.31	1.7429964	0.0281	5625	-	-	-4.331	T
WASP-3 b	2.06	1.8468372	0.0313	6400	0.1073	0.2072	-4.872	T
HD 86081 b	1.5	2.1375	0.039	6028	0.0371	0.085	-4.973	RV
HAT-P-32 b	0.941	2.150009	0.0344	6001	0.4073	0.3978	-	T
WASP-2 b	0.847	2.15222144	0.03138	5150	-	-	-5.054	T
HAT-P-7 b	1.8	2.2047298	0.0379	6350	0.1946	0.1672	-5.018	T
HD 189733 b	1.138	2.21857312	0.03142	4980	-2.3605	-1.6252	-4.501	RV
WASP-14 b	7.341	2.2437661	0.036	6475	-	-	-4.923	T
TrES-2	1.253	2.470614	0.03556	5850	0.2015	0.2055	-4.949	T
WASP-1 b	0.86	2.5199464	0.0382	6200	0.1785	0.2508	-5.114	T
HD 73256 b	1.87	2.54858	0.037	5570	-1.6362	-1.1336	-4.407	RV
XO-2 b	0.62	2.615838	0.0369	5340	-0.2480	-0.0929	-4.988	T
HAT-P-16 b	4.193	2.77596	0.0413	6158	0.1982	0.3938	-	T
HAT-P-5 b	1.06	2.788491	0.04075	5960	-	-	-5.061	T
HAT-P-20 b	7.246	2.875317	0.0361	4595	-5.4172	-4.1585	-	T
HD 149026 b	0.356	2.8758916	0.04288	6147	0.0581	0.1473	-5.030	RV
HAT-P-3 b	0.591	2.899703	0.03866	5185	-0.7236	-0.5572	-4.904	T
HD 83443 b	0.4	2.985625	0.0406	5460	-0.3757	-0.109	-4.84	RV
HD 46375 b	0.249	3.024	0.041	5199	-0.2325	-0.0538	-4.96	RV
TrES-1	0.761	3.0300722	0.0393	5300	-0.7222	-1.1840	-4.738	T
HAT-P-27 b	0.66	3.0395721	0.0403	5300	-0.7542	-0.3335	-	T

Table D.1: (continued)

Object	$M_p \sin i$ [M_J]	P_{orb} [days]	a [AU]	T_{eff} [K]	EQW_K [Å]	EQW_H [Å]	$\log R'_{\text{HK}}$	Detection method
HAT-P-4 b	0.68	3.0565114	0.0446	5860	0.0739	0.1231	-5.082	T
HAT-P-8 b	1.34	3.07632402	0.0449	6200	0.1113	0.1799	-4.985	T
HD 187123 b	0.52	3.0965828	0.0426	5714	-	-	-4.999	RV
XO-3 b	11.79	3.1915239	0.0454	6429	-	-	-4.595	T
HAT-P-22 b	2.147	3.21222	0.0414	5302	-0.5378	-0.2469	-	T
HAT-P-12 b	0.211	3.2130598	0.0384	4650	-1.6008	-0.6398	-5.104	T
Kepler-4 b	0.077	3.21346	0.0456	5857	0.3420	0.5354	-	T
Kepler-6 b	0.669	3.234723	0.04567	5647	0.4951	0.4373	-	T
HAT-P-28 b	0.626	3.257215	0.0434	5680	0.2449	0.1190	-	T
HAT-P-24 b	0.685	3.35524	0.0465	6373	0.8322	0.6930	-	T
HD 88133 b	0.22	3.416	0.047	5494	-0.0570	0.0795	-5.178	RV
HAT-P-33 b	0.763	3.474474	0.0503	6401	0.5521	0.5925	-	T
BD-10 3166 b	0.48	3.487	0.046	5400	-0.8254	-0.3488	-4.847	RV
Kepler-18 b	0.0217	3.504725	0.0447	5383	0.1184	0.4276	-	T
Kepler-8 b	0.603	3.52254	0.0483	6213	0.6870	0.8710	-	T
HD 209458 b	0.714	3.52474859	0.04747	6075	0.0744	0.1229	-5.00	RV
Kepler-5 b	2.114	3.54846	0.05064	6297	0.6038	0.5871	-	T
TrES-4	0.917	3.5539268	0.05084	6200	0.1783	0.1630	-5.104	T
HAT-P-25 b	0.567	3.652836	0.0466	5500	0.1131	0.5228	-	T
WASP-11 b	0.46	3.722469	0.0439	4980	-1.7503	-0.9634	-4.823	T
WASP-17 b	0.486	3.735438	0.0515	6550	-	-	-5.331	T
HD 219828 b	0.066	3.8335	0.052	5891	0.0604	0.1164	-4.945	RV
HAT-P-6 b	1.057	3.853003	0.05235	6570	0.1397	0.1836	-4.799	T
HAT-P-9 b	0.67	3.922814	0.053	6350	-	-	-5.092	T
XO-1 b	0.9	3.9415128	0.0488	5750	-0.0056	0.0293	-4.958	T
HAT-P-19 b	0.292	4.008778	0.0466	4990	-3.8168	-1.2652	-	T
HD 102195 b	0.45	4.113775	0.049	5291	-1.5490	-0.8946	-	RV
HAT-P-21 b	4.063	4.124461	0.0494	5588	-1.6625	-0.9689	-	T
XO-4 b	1.72	4.1250823	0.0555	5700	-	-	-5.292	T
HD 125612 c	0.058	4.1547	0.05	5897	-	-	-4.867	RV
XO-5 b	1.077	4.1877537	0.0487	5510	0.0093	0.0559	-	T
61 Vir b	0.016	4.215	0.050201	5531	-	-	-4.962	RV
51 Peg b	0.468	4.23077	0.052	5793	0.0432	0.2338	-5.08	RV
HAT-P-26 b	0.059	4.234516	0.0479	5079	-0.3556	0.0659	-	T
WASP-13 b	0.485	4.353011	0.05379	5826	-	-	-5.263	T
Kepler-12 b	0.431	4.4379637	0.0556	5947	0.4331	0.4949	-	T
HAT-P-1 b	0.524	4.4652934	0.05535	5975	0.1351	0.1391	-4.984	T
ups And b	0.69	4.617136	0.059	6212	-	-	-4.980	RV
HAT-P-14 b	2.2	4.627657	0.0594	6600	0.1183	0.1667	-4.855	T
HD 156668 b	0.0131	4.646	0.05	4850	-0.8485	-0.4613	-	RV
HAT-P-11 b	0.081	4.887804	0.053	4780	-3.4991	-2.0965	-4.567	T
HD 49674 b	0.115	4.9437	0.058	5482	-0.2634	-0.1234	-4.80	RV
HD 109749 b	0.28	5.24	0.0635	5610	0.0512	0.1015	-4.975	RV
HD 7924 b	0.029	5.3978	0.057	5177	-0.3167	-0.1232	-4.83	RV
HAT-P-18 b	0.197	5.508023	0.0559	4803	-2.6726	-1.4038	-	T
HAT-P-2 b	8.74	5.6334729	0.0674	6290	0.0552	0.0996	-4.78	T
HD 1461 b	0.0239	5.7727	0.063438	5765	0.0179	0.0825	-5.03	RV
HD 68988 b	1.9	6.276	0.071	5767	0.0495	0.0845	-5.04	RV
HD 168746 b	0.23	6.403	0.065	5610	0.0273	0.1815	-5.05	RV
HD 102956 b	0.96	6.495	0.081	5054	-0.2472	0.0111	-	RV
HIP 14810 b	3.88	6.673855	0.0692	5485	-	-	-5.062	RV
HD 185269 b	0.94	6.838	0.077	5980	-	-	-5.077	RV
HD 217107 b	1.33	7.12689	0.073	5666	-	-	-5.086	RV
HIP 57274 b	0.036	8.1352	0.07	4640	-1.5066	-0.8212	-	RV
HD 162020 b	14.4	8.428198	0.074	4830	-4.6563	-3.7086	-	RV
HD 69830 b	0.033	8.667	0.0785	5385	-	-	-4.987	RV

Table D.1: (continued)

Object	$M_p \sin i$ [M_J]	P_{orb} [days]	a [AU]	T_{eff} [K]	EQW _K [Å]	EQW _H [Å]	$\log R'_{\text{HK}}$	Detection method
Kepler-19 b	0.064	9.2869944	0.118	5541	0.1498	0.2958	-	T
HD 97658 b	0.02	9.4957	0.0797	5170	-0.2781	-0.0696	-	RV
HAT-P-17 b	0.53	10.338523	0.0882	5246	0.2963	0.2310	-	T
HD 130322 b	1.02	10.72	0.088	5330	-0.7721	-0.4124	-4.552	RV
HAT-P-15 b	1.946	10.863502	0.0964	5568	0.0856	0.2282	-	T
HD 38529 b	0.78	14.3104	0.131	5697	-	-	-5.007	RV
HD 179079 b	0.08	14.476	0.11	5724	0.0267	0.1008	-5.018	RV
HD 99492 b	0.109	17.0431	0.1232	4740	-0.9996	-0.5199	-	RV
HD 190360 c	0.057	17.1	0.128	5588	-	-	-5.107	RV
HD 16417 b	0.069	17.24	0.14	5936	-	-	-5.050	RV
HD 33283 b	0.33	18.179	0.168	5995	0.1073	0.1574	-5.164	RV
HD 195019 b	3.7	18.20163	0.1388	5787	0.1036	0.2811	-5.022	RV
HD 192263 b	0.72	24.348	0.15	4965	-2.3811	-1.5036	-	RV
HD 224693 b	0.71	26.73	0.233	6037	0.0726	0.1279	-5.082	RV
HD 43691 b	2.49	36.96	0.24	6200	0.0103	0.0655	-4.846	RV
HD 11964 c	0.079	37.91	0.229	5248	-	-	-5.168	RV
HD 45652 b	0.47	43.6	0.23	5312	-0.2185	0.0142	-4.930	RV
HD 107148 b	0.21	48.056	0.269	5797	0.0290	0.0748	-5.03	RV
HD 90156 b	0.057	49.77	0.25	5599	-	-	-4.969	RV
HD 74156 b	1.88	51.65	0.294	5960	-	-	-5.050	RV
HD 37605 b	2.84	55.23	0.26	5475	-	-	-5.025	RV
HD 168443 b	7.659	58.11247	0.2931	5591	-	-	-5.085	RV
HD 85512 b	0.011	58.43	0.26	4715	-2.6150	-1.4743	-	RV
HD 3651 b	0.2	62.23	0.284	5173	-0.2119	0.0358	-5.02	RV
HD 178911 B b	6.292	71.487	0.32	5650	-	-	-4.900	RV
Gl 785 b	0.053	74.72	0.32	5144	-0.4055	-0.1949	-5.011	RV
HD 163607 b	0.77	75.229	0.36	5543	0.0947	0.3270	-5.009	RV
HD 16141 b	0.215	75.82	0.35	5533	0.0657	0.1536	-5.09	RV
HD 114762 b	10.98	83.9151	0.353	5934	-	-	-4.902	RV
HD 80606 b	3.94	111.43637	0.449	5645	-0.0441	0.0523	-	RV
70 Vir b	6.6	116.67	0.48	5432	-	-	-5.116	RV
HD 216770 b	0.65	118.45	0.46	5248	-0.3098	-0.0804	-4.92	RV
HD 52265 b	1.05	119.6	0.5	6159	0.1133	0.1293	-5.02	RV
HD 102365 b	0.05	122.1	0.46	5650	0.0863	0.0712	-4.931	RV
HD 231701 b	1.08	141.6	0.53	6208	0.0829	0.0935	-4.897	RV
HD 37124 b	0.675	154.378	0.53364	5610	-	-	-4.897	RV
HD 11506 c	0.82	170.46	0.639	6058	-	-	-4.983	RV
HD 5891 b	7.6	177.11	0.76	4907	-0.0017	0.4399	-	RV
HD 155358 b	0.89	195	0.628	5760	-	-	-4.931	RV
HD 82943 c	2.01	219	0.746	5874	-	-	-4.918	RV
HD 218566 b	0.21	225.7	0.6873	4820	-1.0175	-0.4221	-	RV
HD 8574 b	2.11	227.55	0.77	6080	0.1015	0.1169	-5.07	RV
HD 134987 b	1.59	258.19	0.81	5740	-	-	-5.081	RV
HD 40979 b	3.28	263.1	0.83	6205	-0.2931	-0.0294	-4.63	RV
HD 12661 b	2.3	263.6	0.83	5742	-	-	-5.024	RV
HD 164509 b	0.48	282.4	0.875	5922	0.2167	0.2618	-4.874	RV
HD 175541 b	0.61	297.3	1.03	5060	-0.2814	-0.1121	-5.23	RV
HD 92788 b	3.86	325.81	0.97	5559	0.0118	0.0975	-5.05	RV
HD 33142 b	1.3	326.6	1.06	5052	-0.2125	0.0631	-	RV
HD 192699 b	2.5	351.5	1.16	5220	-	-	-5.169	RV
HD 4313 b	2.3	356	1.19	5035	-0.2078	0.1786	-	RV
HD 96063 b	0.9	361.1	0.99	5148	-0.0725	0.3247	-5.120	RV
HD 212771 b	2.3	373.3	1.22	5121	-0.1416	0.0554	-5.170	RV
alf Ari b	1.8	380.8	1.2	4553	-0.4053	0.1224	-	RV
HD 28185 b	5.7	383	1.03	5482	0.0092	0.0349	-5.023	RV
HD 28678 b	1.7	387.1	1.24	5076	0.1876	0.2216	-	RV

APPENDIX D. LIST OF EXOPLANETS USED IN CHAPTER 2

Table D.1: (continued)

Object	$M_p \sin i$ [M_J]	P_{orb} [days]	a [AU]	T_{eff} [K]	EQW_K [\AA]	EQW_H [\AA]	$\log R'_{\text{HK}}$	Detection method
HD 75898 b	2.51	418.2	1.19	6021	0.0944	0.1454	-5.056	RV
HD 4203 b	2.07	431.88	1.164	5701	0.0444	0.1040	-5.18	RV
HD 1502 b	3.1	431.8	1.31	5049	-0.0948	0.1779	-	RV
HD 98219 b	1.8	436.9	1.23	4992	-0.1541	0.2442	-	RV
HD 99109 b	0.502	439.3	1.105	5272	-0.1254	-0.0333	-5.06	RV
HD 210277 b	1.23	442.1	1.1	5532	-0.0307	0.0459	-5.06	RV
HD 108863 b	2.6	443.4	1.4	4956	-0.0677	0.0967	-	RV
24 Sex b	1.99	452.8	1.333	5098	-0.186	0.0715	-	RV
HD 188015 b	1.26	456.46	1.19	5520	-0.0296	0.0450	-5.05	RV
HD 136418 b	2	464.3	1.32	5071	-0.0939	0.1845	-	RV
HD 31253 b	0.5	466	1.26	5960	0.1123	0.3844	-5.026	RV
HD 180902 b	1.6	479	1.39	5030	0.3773	0.3547	-	RV
HD 96167 b	0.68	498.9	1.3	5770	0.0629	0.1055	-5.153	RV
HD 20367 b	1.07	500	1.25	6128	-	-	-4.445	RV
HD 114783 b	1.0	501	1.2	5105	-0.5261	-0.2177	-	RV
HD 95089 b	1.2	507	1.51	5002	-0.1224	0.2961	-	RV
HD 158038 b	1.8	521	1.52	4897	-0.4858	0.1794	-	RV
HD 192310 c	0.075	525.8	1.18	5166	-	-	-5.011	RV
HD 4113 b	1.56	526.62	1.28	5688	-0.0128	0.0568	-4.979	RV
HD 19994 b	1.68	535.7	1.42	5984	-	-	-4.843	RV
HD 222582 b	7.75	572.38	1.35	5662	0.0567	0.0711	-4.922	RV
HD 206610 b	2.2	610	1.68	4874	-0.2457	0.2020	-	RV
HD 200964 b	1.85	613.8	1.601	5164	-0.1220	0.3634	-5.135	RV
HD 183263 b	3.67	626.5	1.51	5888	-	-	-5.042	RV
HD 141937 b	9.7	653.22	1.52	5925	-0.1438	-0.0451	-4.94	RV
HD 181342 b	3.3	663	1.78	5014	-0.0290	0.3080	-	RV
HD 116029 b	2.1	670.2	1.73	4951	-0.4563	0.0854	-	RV
HD 5319 b	1.94	675	1.75	5052	-0.3424	-0.0533	-	RV
HD 152581 b	1.5	689	1.48	5155	0.0610	-0.0231	-	RV
HD 38801 b	10.7	696.3	1.7	5222	-0.1931	0.1133	-5.026	RV
HD 82886 b	1.3	705	1.65	5112	0.0341	0.2630	-5.178	RV
HD 18742 b	2.7	772	1.92	5048	-0.2086	0.2808	-	RV
HD 102329 b	5.9	778.1	2.01	4830	-0.5418	0.0876	-	RV
16 Cyg B b	1.68	799.5	1.68	5766	-	-	-5.046	RV
HD 4208 b	0.8	829	1.7	5571	0.0141	0.0243	-4.95	RV
HD 70573 b	6.1	851.8	1.76	5737	-1.2001	-0.8787	-4.187	RV
HD 99706 b	1.4	868	2.14	4932	-0.2245	0.1801	-	RV
HD 131496 b	2.2	883	2.09	4927	-0.2836	0.0937	-	RV
HD 45350 b	1.79	890.76	1.92	5754	0.0338	0.0851	-5.10	RV
HD 30856 b	1.8	912	2	4982	-0.2822	0.0986	-	RV
HD 16175 b	4.4	990	2.1	6000	-	-	-5.048	RV
HD 34445 b	0.79	1049	2.07	5836	-	-	-4.945	RV
HD 10697 b	6.38	1076.4	2.16	5641	-0.0343	0.1128	-5.08	RV
47 Uma b	2.53	1078	2.1	5892	-	-	-4.973	RV
HD 114729 b	0.84	1135	2.08	5662	0.0658	0.1191	-5.05	RV
HD 170469 b	0.67	1145	2.24	5810	0.0452	0.1043	-5.09	RV
HD 164922 b	0.36	1155	2.11	5385	-0.1236	-0.0144	-5.05	RV
HD 30562 b	1.29	1157	2.3	5861	0.0667	0.0853	-5.04	RV
HD 126614 b	0.38	1244	2.35	5585	0.0434	0.0821	-	RV
HD 50554 b	5.16	1293	2.41	5902	0.0535	0.0976	-4.95	RV
HD 142245 b	1.9	1299	2.77	4878	-0.2781	0.0747	-	RV
HD 196885 A b	2.98	1326	2.6	6340	0.1021	0.1250	-5.01	RV
HD 171238 b	2.6	1523	2.54	5467	-1.3506	-0.8873	-4.605	RV
HD 23596 b	8.1	1565	2.88	5888	-	-	-5.011	RV
HD 106252 b	7.56	1600	2.7	5754	0.0617	0.0811	-4.97	RV
14 Her b	4.64	1773.4	2.77	5311	-0.1555	-0.0599	-5.06	RV

Table D.1: (continued)

Object	$M_p \sin i$ [M_J]	P_{orb} [days]	a [AU]	T_{eff} [K]	EQW_K [\AA]	EQW_H [\AA]	$\log R'_{\text{HK}}$	Detection method
HD 73534 b	1.15	1800	3.15	4952	-0.4324	-0.1126	-	RV
HD 66428 b	2.82	1973	3.18	5752	0.0465	0.0870	-5.08	RV
HD 89307 b	1.78	2157	3.27	5950	0.0688	0.0717	-4.95	RV
HD 50499 b	1.71	2482.7	3.86	5902	0.1008	0.0988	-5.02	RV
eps Eri b	1.55	2502	3.39	5116	-	-	-4.448	RV
HD 117207 b	2.06	2627.08	3.78	5432	0.0276	0.0666	-5.06	RV
HD 87883 b	12.1	2754	3.6	4980	-0.6913	-0.4141	-	RV
HD 106270 b	11	2890	4.3	5638	-0.2846	-0.0745	-4.901	RV
HD 154345 b	0.947	3340	4.19	5468	-0.1824	-0.0172	-4.91	RV
HD 72659 b	3.15	3658	4.74	5926	0.0844	0.1234	-5.02	RV
HD 13931 b	1.88	4218	5.15	5829	0.1010	0.2005	-5.009	RV
HD 149143 b	1.36	4.088	0.052	5730	0.0716	0.0334	-4.97	RV
HD 179949 b	0.95	3.0925	0.045	6260	0.0678	-0.0711	-4.72	RV
HD 212301 b	0.45	2.245715	0.036	5998	0.0966	0.0478	-4.84	RV
WASP-18 b	10.43	0.9414518	0.02047	6400	0.2145	0.0908	-5.43	T

APPENDIX E

LIST OF ABBREVIATIONS AND CONSTANTS

ADPS	The Asiago Database on Photometric Systems
AU	Astronomical Unit
BJD	Barycentric Julian Date
CONICA	Near-Infrared Imager and Spectrograph
CoRoT	Convection, Rotation and planetary Transits
ESO	European Southern Observatory
EQW	Equivalent width
ETD	Exoplanet Transit Database
FEROS	The Fiber-fed Extended Range Optical Spectrograph
HIRES	High Resolution Echelle Spectrometer
HJD	Heliocentric Julian Date
IAU	International Astronomical Union
IRAC	Infrared array camera
KOI	Kepler Object of Interest
KPNO	Kitt Peak National Observatory
K–S test	Kolmogorov–Smirnov test
LIRIS	Long-slit Intermediate Resolution Infrared Spectrograph
M_p	Planetary mass
M_J	Jupiter mass
MC	Monte Carlo
MPG	Max-Planck Gesellschaft
M_\odot	Mass of the Sun
NaCo	NAOS-CONICA
NAOS	Nasmyth Adaptive Optics System
OPTIC	Orthogonal Parallel Transfer Imaging Camera
QE	Quantum efficiency

APPENDIX E. LIST OF ABBREVIATIONS AND CONSTANTS

R_{\odot}	Radius of the Sun
R_{\oplus}	Radius of the Earth
R_p	Planetary radius
R_J	Jupiter radius
RS CVn	RS Canum Venaticorum
RV	Radial Velocity
T test	Student's t -test
VLT	Very Large Telescope
<hr/>	
M_J	$1.899 \cdot 10^{27}$ kg
R_J	$7.149 \cdot 10^4$ km
M_{\odot}	$1.989 \cdot 10^{30}$ kg
R_{\odot}	$6.9599 \cdot 10^5$ km
<hr/> <hr/>	

BIBLIOGRAPHY

- Allard, F., Guillot, T., Ludwig, H.-G., et al. 2003, in IAU Symposium, Vol. 211, Brown Dwarfs, ed. E. Martín, 325
- Alves, S., Do Nascimento, Jr., J. D., & de Medeiros, J. R. 2010, MNRAS, 408, 1770
- Baglin, A., Auvergne, M., Barge, P., et al. 2002, in ESA Special Publication, Vol. 485, Stellar Structure and Habitable Planet Finding, ed. B. Battrick, F. Favata, I. W. Roxburgh, & D. Galadi, 17–24
- Baliunas, S. L., Donahue, R. A., Soon, W. H., et al. 1995, ApJ, 438, 269
- Baraffe, I., Chabrier, G., & Barman, T. 2008, A & A, 482, 315
- Barnes, J. W., Linscott, E., & Shporer, A. 2011, ApJS, 197, 10
- Barros, S. C. C., Boué, G., Gibson, N. P., et al. 2013, MNRAS
- Bessell, M. S. 1990, PASP, 102, 1181
- Bodenheimer, P., Lin, D. N. C., & Mardling, R. A. 2001, ApJ, 548, 466
- Borucki, W. J. & Kepler Team. 2010, ArXiv e-prints
- Borucki, W. J., Koch, D., Basri, G., et al. 2003, in ESA Special Publication, Vol. 539, Earths: DARWIN/TPF and the Search for Extrasolar Terrestrial Planets, ed. M. Fridlund, T. Henning, & H. Lacoste, 69–81
- Borucki, W. J., Koch, D. G., Basri, G., et al. 2011, ApJ, 736, 19
- Budaj, J. 2011, AJ, 141, 59
- Budaj, J. & Richards, M. T. 2004, Contributions of the Astronomical Observatory Skalnaté Pleso, 34, 167
- Burrows, A., Budaj, J., & Hubeny, I. 2008, ApJ, 678, 1436
- Burrows, A., Hubeny, I., Budaj, J., & Hubbard, W. B. 2007, ApJ, 661, 502

BIBLIOGRAPHY

- Canto Martins, B. L., Das Chagas, M. L., Alves, S., et al. 2011, *A & A*, 530, A73+
- Castelli, F. & Kurucz, R. L. 2004, *ArXiv Astrophysics e-prints*
- Charbonneau, D., Allen, L. E., Megeath, S. T., et al. 2005, *ApJ*, 626, 523
- Charbonneau, D., Brown, T. M., Latham, D. W., & Mayor, M. 2000, *ApJl*, 529, L45
- Chauvin, G., Lagrange, A.-M., Dumas, C., et al. 2004, *A & A*, 425, L29
- Christian, D. J., Gibson, N. P., Simpson, E. K., et al. 2009, *MNRAS*, 392, 1585
- Christiansen, J. L., Ballard, S., Charbonneau, D., et al. 2011, *ApJ*, 726, 94
- Claret, A. 2000, *A & A*, 363, 1081
- Colón, K. D., Ford, E. B., Lee, B., Mahadevan, S., & Blake, C. H. 2010, *MNRAS*, 408, 1494
- Cowan, N. B. & Agol, E. 2011, *ApJ*, 729, 54
- Croll, B., Jayawardhana, R., Fortney, J. J., Lafrenière, D., & Albert, L. 2010, *ApJ*, 718, 920
- Cuntz, M., Saar, S. H., & Musielak, Z. E. 2000, *ApJl*, 533, L151
- De Mooij, E. J. W. & Snellen, I. A. G. 2009, *A & A*, 493, L35
- de Pater, I. & Lissauer, J. J. 2001, *Planetary Sciences* (Cambridge UK: University Press, 2001)
- Deming, D., Seager, S., Richardson, L. J., & Harrington, J. 2005, *Nat*, 434, 740
- Dittmann, J. A., Close, L. M., Scuderi, L. J., & Morris, M. D. 2010, *ApJ*, 717, 235
- Dommanget, J. & Nys, O. 2002, *VizieR Online Data Catalog*, 1274, 0
- Duncan, D. K., Vaughan, A. H., Wilson, O. C., et al. 1991, *ApJS*, 76, 383
- Eberhard, G. & Schwarzschild, K. 1913, *ApJ*, 38, 292
- Fortney, J. J., Lodders, K., Marley, M. S., & Freedman, R. S. 2008, *ApJ*, 678, 1419
- Fressin, F., Knutson, H. A., Charbonneau, D., et al. 2010, *ApJ*, 711, 374
- Gibson, N. P., Pollacco, D., Simpson, E. K., et al. 2009, *ApJ*, 700, 1078
- Gonzalez, G. 2011, *MNRAS*, 416, L80

- Guillot, T. & Showman, A. P. 2002, *A & A*, 385, 156
- Hall, D. S. 1976, in *Astrophysics and Space Science Library*, Vol. 60, IAU Colloq. 29: Multiple Periodic Variable Stars, ed. W. S. Fitch, 287
- Hall, J. C. 2008, *Living Reviews in Solar Physics*, 5, 2
- Hartman, J. D. 2010, *ApJl*, 717, L138
- Henry, G. W., Marcy, G. W., Butler, R. P., & Vogt, S. S. 2000, *ApJl*, 529, L41
- Hubbard, W. B., Hattori, M. F., Burrows, A., Hubeny, I., & Sudarsky, D. 2007, *Icarus*, 187, 358
- Hubeny, I. & Burrows, A. 2007, *ApJ*, 669, 1248
- Hubeny, I., Burrows, A., & Sudarsky, D. 2003, *ApJ*, 594, 1011
- Isaacson, H. & Fischer, D. 2010, *ApJ*, 725, 875
- Johnson, J. A., Winn, J. N., Cabrera, N. E., & Carter, J. A. 2009, *ApJl*, 692, L100
- Jordán, A. & Bakos, G. Á. 2008, *ApJ*, 685, 543
- Kashyap, V. L., Drake, J. J., & Saar, S. H. 2008, *ApJ*, 687, 1339
- Knutson, H. A., Charbonneau, D., Allen, L. E., et al. 2007, *Nat*, 447, 183
- Knutson, H. A., Howard, A. W., & Isaacson, H. 2010, *ApJ*, 720, 1569
- Krejčová, T. & Budaj, J. 2012, *A & A*, 540, A82
- Krejčová, T., Budaj, J., & Krushevska, V. 2010, *Contributions of the Astronomical Observatory Skalnaté Pleso*, 40, 77
- Kundurthy, P., Becker, A. C., Agol, E., Barnes, R., & Williams, B. 2013, *ApJ*, 764, 8
- Li, S.-L., Miller, N., Lin, D. N. C., & Fortney, J. J. 2010, *Nat*, 463, 1054
- Loeb, A. & Gaudi, B. S. 2003, *ApJl*, 588, L117
- Maciejewski, G., Dimitrov, D., Neuhäuser, R., et al. 2011a, *MNRAS*, 411, 1204
- Maciejewski, G., Raetz, S., Nettelmann, N., et al. 2011b, *A & A*, 535, A7
- Mandel, K. & Agol, E. 2002, *ApJl*, 580, L171
- Maxted, P. F. L., Marsh, T. R., & North, R. C. 2000, *MNRAS*, 317, L41

BIBLIOGRAPHY

- Mayor, M. & Queloz, D. 1995, *Nat*, 378, 355
- Mazeh, T. & Faigler, S. 2010, *A & A*, 521, L59
- Mazeh, T., Nachmani, G., Sokol, G., Faigler, S., & Zucker, S. 2012, *A & A*, 541, A56
- Middelkoop, F. 1982, *A & A*, 107, 31
- Mislis, D. & Hodgkin, S. 2012, *MNRAS*, 422, 1512
- Niedzielski, A., Maciejewski, G., & Czart, K. 2003, *Acta Astron.*, 53, 281
- Noyes, R. W., Hartmann, L. W., Baliunas, S. L., Duncan, D. K., & Vaughan, A. H. 1984, *ApJ*, 279, 763
- O'Donovan, F. T., Charbonneau, D., Bakos, G. Á., et al. 2007, *ApJl*, 663, L37
- Poddaný, S., Brát, L., & Pejcha, O. 2010, *New A*, 15, 297
- Poppenhaeger, K., Robrade, J., & Schmitt, J. H. M. M. 2010, *A & A*, 515, A98
- Poppenhaeger, K. & Schmitt, J. H. M. M. 2011, *ApJ*, 735, 59
- Press, W. H., Teukolsky, S. A., Vetterling, W. T., & Flannery, B. P. 1992, *Numerical recipes in FORTRAN. The art of scientific computing* (Cambridge: University Press, —c1992, 2nd ed.)
- Rubenstein, E. P. & Schaefer, B. E. 2000, *ApJ*, 529, 1031
- Sada, P. V., Deming, D., Jennings, D. E., et al. 2012, *PASP*, 124, 212
- Santerne, A., Moutou, C., Barros, S. C. C., et al. 2012, *A & A*, 544, L12
- Scharf, C. A. 2010, *ApJ*, 722, 1547
- Schneider, J., Dedieu, C., Le Sidaner, P., Savalle, R., & Zolotukhin, I. 2011, *A & A*, 532, A79
- Schrijver, C. J. & Zwaan, C. 2000, *Solar and Stellar Magnetic Activity* (Cambridge: University Press, 2000)
- Seager, S. & Deming, D. 2010, *ARA&A*, 48, 631
- Seager, S., Richardson, L. J., Hansen, B. M. S., et al. 2005, *ApJ*, 632, 1122
- Shkolnik, E. 2004, PhD thesis, University of British Columbia

- Shkolnik, E., Bohlender, D. A., Walker, G. A. H., & Collier Cameron, A. 2008, *ApJ*, 676, 628
- Shkolnik, E., Walker, G. A. H., & Bohlender, D. A. 2003, *ApJ*, 597, 1092
- Shkolnik, E., Walker, G. A. H., Bohlender, D. A., Gu, P., & Kürster, M. 2005, *ApJ*, 622, 1075
- Shkolnik, E. L. 2013, *ApJ*, 766, 9
- Showman, A. P. & Guillot, T. 2002, *A & A*, 385, 166
- Shporer, A., Jenkins, J. M., Rowe, J. F., et al. 2011, *AJ*, 142, 195
- Sing, D. K. 2010, *A & A*, 510, A21
- Smith, A. M. S., Hebb, L., Collier Cameron, A., et al. 2009, *MNRAS*, 398, 1827
- Sozzetti, A., Torres, G., Charbonneau, D., et al. 2009, *ApJ*, 691, 1145
- Szabó, G. M., Szabó, R., Benkő, J. M., et al. 2011, *ApJl*, 736, L4
- Turner, J. D., Smart, B. M., Hardegree-Ullman, K. K., et al. 2013, *MNRAS*, 428, 678
- Vaughan, A. H., Preston, G. W., Baliunas, S. L., et al. 1981, *ApJ*, 250, 276
- Vaughan, A. H., Preston, G. W., & Wilson, O. C. 1978, *PASP*, 90, 267
- Vaňko, M., Maciejewski, G., Jakubík, M., et al. 2013, *MNRAS*
- Vernazza, J. E., Avrett, E. H., & Loeser, R. 1981, *ApJS*, 45, 635
- Vidal-Madjar, A., Lecavelier des Etangs, A., Désert, J.-M., et al. 2003, *Nat*, 422, 143
- Vogt, S. S., Allen, S. L., Bigelow, B. C., et al. 1994, in *Society of Photo-Optical Instrumentation Engineers (SPIE) Conference Series*, Vol. 2198, *Society of Photo-Optical Instrumentation Engineers (SPIE) Conference Series*, ed. D. L. Crawford & E. R. Craine, 362
- von Zeipel, H. 1924, *MNRAS*, 84, 665
- Welsh, W. F., Orosz, J. A., Seager, S., et al. 2010, *ApJl*, 713, L145
- Wilson, O. C. 1968, *ApJ*, 153, 221
- Wilson, O. C. 1978, *ApJ*, 226, 379

BIBLIOGRAPHY

Wilson, R. E. 1990, *ApJ*, 356, 613

Winn, J. N. 2011, *Exoplanet Transits and Occultations* (University of Arizona Press, 2011), 55–77

Winn, J. N., Holman, M. J., Shporer, A., et al. 2008, *AJ*, 136, 267

Wolszczan, A. & Frail, D. A. 1992, *Nat*, 355, 145

Wright, J. T., Marcy, G. W., Butler, R. P., & Vogt, S. S. 2004, *ApJS*, 152, 261

This thesis has been typeset with \LaTeX .

LIST OF PUBLICATIONS

PAPERS

1. **Krejčová, T.**, Budaj, J. 2012, *Evidence for enhanced chromospheric Ca II H and K emission in stars with close-in extrasolar planets*, A&A, 540, A82
2. **Krejčová, T.**, Budaj, J., Krushevska, V. 2010, *Photometric observations of transiting extrasolar planet Wasp-10 b*, CoSka, 44, 77
3. Maciejewski, G., Dimitrov, D., Neuhauser, R., Tetzlaff, N., Niedzielski, A., Raetz, St., Chen, W. P., Walter, F., Marka, C., Baar, S., **Krejčová, T.**, Budaj, J., Krushevska, V., Tachihara, K., Takahashi, H., Mugrauer, M. 2011, *Transit timing variation and activity in the Wasp-10 planetary system*, MNRAS, 411, 1204
4. Vaňko, M., Maciejewski, G., Jakubík, M., **Krejčová, T.**, Budaj, J., Pribulla, T., Ohlert, J., Raetz, St., Parimucha, Š., Bukowiecki, L. 2013, *New photometric observations of the transiting planetary system TrES-3: Long-term stability of the system*, MNRAS, ArXiv eprints:1303.4535
5. In preparation: Kohout, T., Havrila, K., Tóth, J., Husárik, M., Gritsevich, M., Britt, D., Borovička, J., Spurný, P., Igaz, A., Svoreň, J., Kornoš, L., Vereš, P., Koza, J., Kučera, A., Zigo, P., Gajdoš, Š., Világi, J., Čapek, D., Křišandová, Z., Tomko, D., Šilha, J., Schunová, E., Bodnárová, M., Búzová, D., **Krejčová, T.**; *Density, porosity and magnetic susceptibility of the Košice meteorites and homogeneity of H chondrite showers*, Meteoritics & Planetary Science, 2013

CONFERENCE PROCEEDINGS

1. **Krejčová, T.**, Budaj, J., Koza, J. 2012, *Search for the Star–Planet Interaction*, IAUS, 282, 125
2. Vaňko, M., Jakubík, M., **Krejčová, T.**, Maciejewski, G., Budaj, J., Pribulla, T., Ohlert, J., Raetz, S., Krushevska, V., Dubovský, P. 2012, *New Photometric Observations of the Transiting Extrasolar Planet TrES-3b*, IAUS, 282, 135
3. **Krejčová, T.**, Budaj, J. 2010, *Photometric Observation of Transiting Extrasolar Planet Wasp-10b*, ASPC, 435, 447
4. Toth, J., Porubčan, V., Borovička, J., Igaz, A., Spurný, P., Svoreň, J., Husárik, M., Kornoš, L., Vereš, P., Zigo, P., Koza, J., Kučera, A., Gajdoš, S., Világi, J., Čapek, D., Šilha, J., Schunová, E., Křišandová, Z., Tomko, D., Bodnarová, M., Búzová, D., **Krejčová, T.** 2012, *Košice meteorite – recovery and the strew field*, European Planetary Science Congress 2012, EPSC2012-708
5. **Krejčová, T.**, Budaj, J., Krushevska, V. 2011, *Extrasolar planetary system WASP-10*, 42nd Conference on Variable Stars Research, OEJV, 139, 10-12
6. **Krejčová, T.** 2009, *Photometry of extrasolar planets*, 40th Conference on Variable Stars Research, OEJV, 109, 28